ENERGY TRANSPORT IN INERTIAL CONFINEMENT FUSION PLASMAS

By

KARABI GHOSH

PHYS 01200704016

Bhabha Atomic Research Centre, Mumbai

A thesis submitted to the

Board of Studies in Physical Sciences

In partial fulfillment of requirements

for the Degree of

DOCTOR OF PHILOSOPHY

of

HOMI BHABHA NATIONAL INSTITUTE

April, 2013

Homi Bhabha National Institute

Recommendations of the Viva Voce Committee

As members of the Viva Voce Committee, we certify that we have read the dissertation prepared by Karabi Ghosh entitled "Energy Transport in Inertial Confinement Fusion Plasmas" and recommend that it may be accepted as fulfilling the thesis requirement for the degree of Doctor of Philosophy.

Chairman	**Date:**
Guide/Convener-(Prof. N. K. Gupta)	**Date:**
Member1	**Date:**
Member2	**Date:**
Member3	**Date:**

Final approval and acceptance of this dissertation is contingent upon the candidate's submission of the final copies of the thesis to HBNI.

I hereby certify that I have read this thesis prepared under my direction and recommend that it may be accepted as fulfilling the thesis requirement.

Date:

Place:

Guide

STATEMENT BY AUTHOR

This dissertation has been submitted in partial fulfillment of requirements for an advanced degree at Homi Bhabha National Institute (HBNI) and is deposited in the Library to be made available to borrowers under rules of the HBNI.

Brief quotations from this dissertation are allowable without special permission, provided that accurate acknowledgement of source is made. Requests for permission for extended quotation from or reproduction of this manuscript in whole or in part may be granted by the Competent Authority of HBNI when in his or her judgment the proposed use of the material is in the interests of scholarship. In all other instances, however, permission must be obtained from the author.

(Karabi Ghosh)

DECLARATION

I, hereby declare that the investigation presented in the thesis has been carried out by me. The work is original and has not been submitted earlier as a whole or in part for a degree / diploma at this or any other Institution / University.

(Karabi Ghosh)

List of Publications arising from the thesis

Journal

1. "Energy Deposition of Charged Particles and Neutrons in an Inertial Confinement Fusion Plasma", Karabi Ghosh and S.V.G. Menon, 2007, *Nuclear Fusion*, 47, 1176-1183.

2. "Fully implicit 1D radiation hydrodynamics: Validation and verification", Karabi Ghosh and S.V.G. Menon, 2010, *Journal of Computational Physics*, 229, 7488-7502.

3. "Analytical benchmark for non-equilibrium radiation diffusion in finite size systems", Karabi Ghosh, 2014, *Annals of Nuclear Energy*, 63, 59-68.

Conferences

1. "Study of the ignition requirements and burn characteristics of DT_x pellets for ICF", Karabi Ghosh and S.V.G. Menon,2010, *Journal of Physics: Conf. Series*, 208, 012003.

2. "Convergence studies of fully implicit 1D radiation hydrodynamics", Karabi Ghosh and S. V. G. Menon, *DAE-BRNS National Laser Symposium (NLS-19)*, Raja Ramanna Centre for Advanced Technology, Indore, India, 1-4 December 2010. Paper No. 3281, P-6.09, Page 101.

3. "Melting curve of metals using classical molecular dynamics simulations", Karabi Ghosh, 2012, *Journal of Physics: Conf Series*, 377, 012085.

4. "Effect of site selective Ti substitution on the melting point of CuTi alloys", Karabi Ghosh and M. Ghosh, 2013, *AIP Conf. Proc.*, 1512, 58-59.

5. "Thermonuclear burn and fusion yields of DT pellets", Karabi Ghosh *DAE-BRNS National Laser Symposium (NLS-21)*, Bhabha Atomic Research Centre, Mumbai, India, 6-9 February 2013. Paper no. 4007, CP-08-01, Page 87.

Others

1. “High Energy Density Systems-Physics and Modelling”, S.V.G.Menon, Karabi Ghosh et. al. *IANCAS Bulletin* January 2010.

(Karabi Ghosh)

DEDICATIONS

To Manoranjan

ACKNOWLEDGEMENTS

I am grateful from the core of my heart to my supervisor Prof. N. K. Gupta for his constant support and encouragement. He has helped me improve the quality of my work with his useful suggestions and critical comments. Timely completion of this thesis is possible because of his sincere efforts. I am thankful to Prof. S. V. G. Menon, former Head, ThPD, for introducing me to this subject and teaching me the basics of programming. He has always taken keen interest in analyzing the results and clearing my doubts. I would like to acknowledge my PhD doctoral committee members Prof. Y. S. Mayya (Chairman), Prof. S. Chaturvedi and Prof. A. Shyam for devoting their valuable time to assess the progress of my work every year. Thanks are due to Dr. V. Kumar, Head, ThPD for helping me improve my knowledge by suggesting good books, reports and recent papers relevant to my work from time to time. I am grateful to Dr. T. K. Basu for his encouragement and suggestions.

All my colleagues, both seniors and juniors have been instrumental in making my interactions in office an enjoyable experience. Special thanks to Dr. M. K. Srivastava who has always been ready to share his knowledge on high energy density physics and differential equations. Thanks are due to Dr. A. Ray and Dr. G. Kondayya for innumerable valuable and useful discussions. I want to thank Dr. D. Biswas and Dr. R. Kumar for their help in solving problems regarding software installation and usage. I have shared the positive developments, failures and disappointments with Chandrani-di, Madhu-di, Gaurav, Bishnupriya and Sai. Thanks to all of them for putting up with me.

I gratefully acknowledge the role of my parents for their unconditional love, blessings and sacrifices to make this thesis possible. Last, but not the least, I would like to express gratitude to my husband Manoranjan for bringing out the best in me. His criticisms and comments have helped me realise the deficiencies in the work and rectify them to the extent possible. He and our son Antarip kept me relaxed with their constant fun and frolic.

Contents

Synopsis

Inertial Confinement Fusion (ICF) is a process where thermonuclear fusion reactions are initiated in a fusion fuel (e.g., DT, DD, DHe^3, etc) by compressing it to tremendous densities and temperatures by focusing high power laser or charged particle beams on the surface of the pellet or via X-rays in a hohlraum [1]. The inertia of the fuel pellet helps in confining it long enough to produce more fusion energy than is expended in heating and containing it. The twin requirements of heating and confinement is represented by the Lawson criterion which is obtained by balancing the fusion energy release against the energy investment in ablating, compressing, heating the fuel to thermonuclear temperatures and the energy lost through radiation. In the laboratory, ICF plasmas provide us with very high densities and temperatures, i.e., extreme conditions normally obtained in the interior of stars. If good theoretical understanding of the physical processes taking place in ICF plasmas is developed, experiments related to ICF can be designed with confidence. Numerical simulation is a very convenient tool in this regard. Starting with the appropriate initial conditions, we can predict the outcome of an experiment by properly accounting the material properties and conservation laws. Energy deposition by charged particles and neutrons, energy exchange between ions and electrons, and interaction between radiation and material are the primary energy transport mechanisms within a thermonuclear plasma. In the present thesis, an improved model of charged particle energy deposition has been developed by considering large angle Coulomb scattering, nuclear scattering and collective plasma effects. The same model is then used to re-evaluate the concept of internal tritium breeding in high density ICF pellets. The zero-dimensional model consisting of rate equation for total number of nuclides, detailed energy deposition and all possible energy loss mechanisms is used to study the thermonuclear burn characteristics of compressed DT microspheres. For validating radiation diffusion codes, new analytical benchmark results for the non-equilibrium Marshak diffusion problem in a planar slab, sphere and spherical shell of finite thickness are derived using two independent methods, namely the Laplace transform method

and the eigenfunction expansion method. In order to linearize the radiation transport and material energy equation, the heat capacity is assumed to be proportional to the cube of the material temperature. This assumption is made to relax the physical content of the problem such that a detailed analytical solution can be obtained and provide useful test problems for radiative transfer codes, since those codes handle an arbitrary temperature dependence of the heat capacity. As the zero dimensional model lacks spatial variation, which is a pre-requisite for studying shock propagation, pellet implosion and explosion, etc, fully implicit one-dimensional 3T Lagrangian hydrodynamic code is developed. Radiation transport equation is solved using the discrete ordinates method and coupled with hydrodynamic code. These codes have been used to study a range of significant problems in ICF. The work described in this thesis is divided into seven chapters.

Chapter 1

In this chapter we introduce the various physical processes like hydrodynamic ablation, shock compression, radiation transport, thermonuclear ignition and burn propagation, etc. occurring in ICF pellets. The analytical and numerical techniques/methodologies commonly used for studying these mechanisms are described along with their range of applicability. We also bring out the motivation behind the work presented in this thesis and its impact on current understanding of the subject.

Chapter 2

The details of the charged particle and neutron energy deposition are described in this chapter. The calculation of energy leakage probability is generalized to include nuclear scattering, large angle Coulomb scattering and collective plasma effects. In general, these processes reduce the thermalization distance in the plasma and increase the fraction of energy deposited to ions. The fraction of the charged particle energy that is absorbed by the ICF pellet is an important parameter determining the ignition condition. For pellet sizes comparable to the thermalization range of fusion products, a part of the energy will escape the pellet. This fraction was calculated

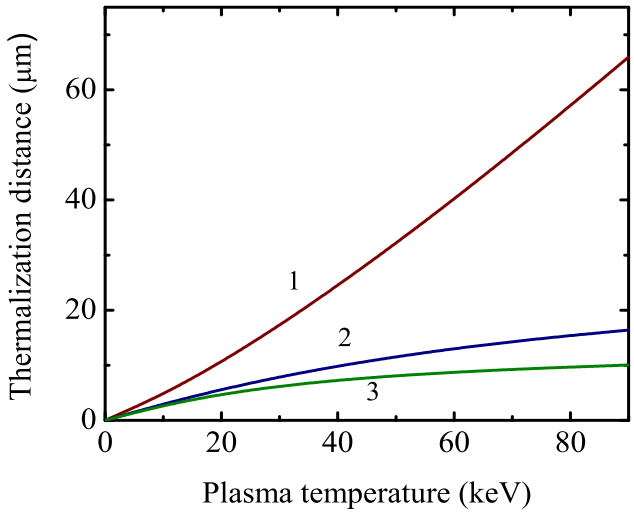

Figure 1: Thermalization distance of deuterons Vs. plasma temperature in a deuterium plasma of ion number density $10^{26}/cm^3$ for the three cases of energy loss: 1. only to electrons, 2. electrons and ions and 3. including nuclear scattering.

by Krokhin and Rozanov [3] by considering energy transfer only to electrons. Later, Cooper and Evans improved this calculation by including energy transfer to ions within the small angle binary collision approximation [4]. The effects of nuclear interactions have not been taken into account previously as it is negligible for small scattering angles. However, when the incident charged particle energy is large (as in the case of the proton produced in D^2-He^3 reaction) and for higher plasma temperatures, the effect of nuclear scattering is important [5]. In this chapter, we evaluate the effects of elastic nuclear scattering, large angle Coulomb scattering and collective plasma effects on the fraction of energy leaking from the pellet, thereby improving the earlier results by Cooper et al [4]. As a representative of these results, we show the effect of including all the above mentioned energy deposition mechanisms on thermalization distance and energy leakage probability in figures 1 and 2 respectively. A simple approach for energy deposition by neutrons due to nuclear interaction with the ions is also developed using a multi group model.

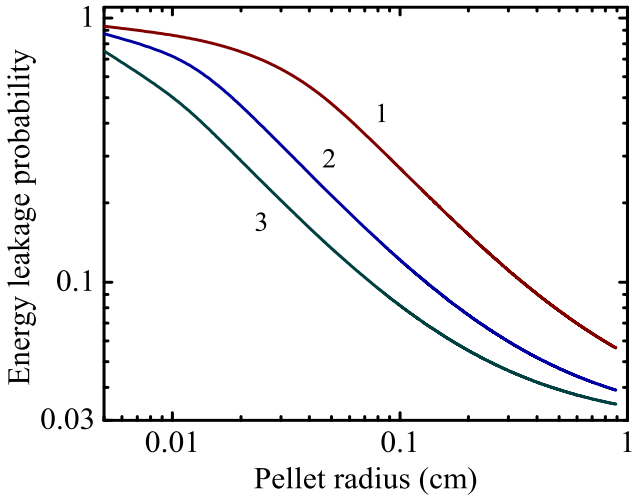

Figure 2: Energy leakage probability of deuterons Vs. pellet radius in a deuterium plasma at temperature 0.1 MeV and ion number density $10^{26}/cm^3$ for the three cases of energy loss: 1. only to electrons, 2. electrons and ions and 3. including nuclear scattering.

Chapter 3

This chapter deals with the application of the improved energy deposition model to analyze Internal Tritium breeding and thermonuclear burn characteristics of compressed D-T microspheres. The D-T fusion reaction has a much higher cross section compared to D-D reaction at lower temperatures. As a result, the ignition temperature in deuterium (D) fusion targets can be significantly reduced with the addition of small quantities of tritium (T). Due to beta-decay, with half life of 12.5 years, tritium does not occur in nature, and hence has to be produced artificially. For instance, neutrons from the D-T reactions produce tritium in a Li-blanket surrounding the fusion reactor via the (n,γ) reaction with lithium. Production of large quantities of tritium by such means is technologically challenging, and so the internal breeding of tritium in D-T pellets is a useful concept [6]. As one of the channels of D-D reaction produces tritium, a proper pellet design, with a small concentration of tritium, can be made such that its concentration at the end of the burn is same or more than the initial concentration. The small amount of

initial tritium, thus, acts as a catalyst during the course of fusion burn. The simulation model considers the rate of decay or buildup of the six nuclides (D, T, He^3, He^4, p, n) participating in the 4 reactions: D-D (proton channel), (D-D) (neutron channel), (D-T) and (D-He^3). Energy balance equations for ions, electrons and radiation, within the three-temperature model, including all the energy exchange processes, determine the time dependent temperatures. Finally, the hydrodynamic disassembly of the pellet determines the extent of burn. An accurate formula for the Maxwellian averaged fusion cross-sections for all the four reactions, valid up to 500 keV temperatures has been used [7]. We consider an optimal pellet configuration of density ρ=5000 gm/cm^3, ρR =12.5 gm/cm^2 where R is the pellet radius, tritium fraction x= 0.0112, and ion, electron, and radiation temperatures given by T_i= T_e= 10 keV and T_r= 1 keV, respectively, analyzed by Eliezer et al [6]. While this pellet showed tritium breeding within the assumptions made by Eliezer et al, it failed to show breeding when inverse Compton scattering and photon losses were taken into account. However with the improved energy deposition model by charged particles and neutrons and using the improved formulas for fusion reaction rates it is found that the pellet breeds tritium even under extreme conditions of radiation loss. As a representative of these results we show the variation in T ratio as a function of time on including all the energy loss mechanisms in figure 3.

Using the above described zero dimensional three temperature model which considers all the energy deposition mechanisms like small and large angle Coulomb scattering, nuclear scattering and collective plasma effects, the effect of varying various pellet parameters like its density, fraction of tritium added and initial temperature on the burn fraction and tritium breeding ratio is studied. We conclude that for sufficient burning of the pellet and for tritium to behave as a catalyst, the following optimum pellet configuration is necessary:

- the initial pellet density $\geq$ 3500gm/cc
- initial plasma temperature $\geq$ 4 keV

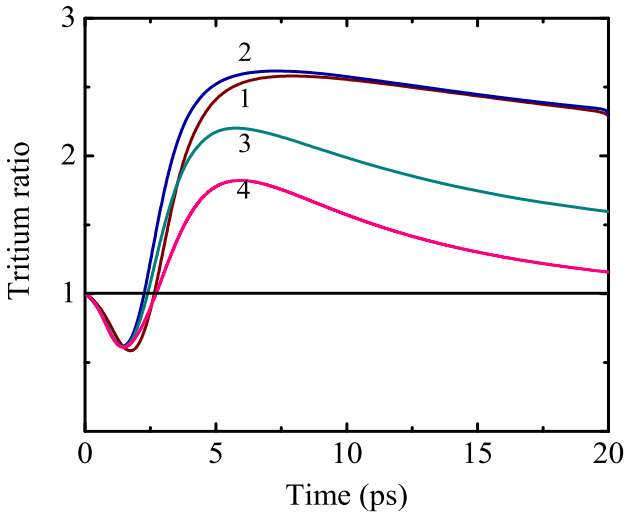

Figure 3: Tritium breeding Vs. time for the DT pellet. Curve-1 refers to bremsstrahlung loss only, Curve-2 includes inverse bremsstrahlung as well, Curve-3 includes, in addition, inverse Compton scattering and Curve-4 is similar to curve-3, but without photon losses.

- fraction of tritium added lies between 0.005 and 0.02 i.e., $0.005 \leq x \leq 0.02$

The zero-dimensional model is also applied for studying the thermonuclear burn characteristics of compressed D-T microspheres. Fusion yields in case of volume and central ignition have been considered. Yields have been obtained for DT pellets of different masses and densities having a range of initial temperatures. As a representative of the obtained results, the yield vs. density of a 10 μg pellet having various initial temperatures is shown in figure 4. The fusion yields are found to increase as $\rho^{2/3}$ for lower densities and then rise steeply and finally saturates. Higher is the initial pellet temperature, more is the fusion yield because of the increase in DT and DD fusion reactions as a function of temperature. Also, as the initial pellet temperatures increase, the fusion yield attains saturation values for lower pellet densities. For an initial pellet temperature of 1.8 keV, there is no steep rise in the fusion yield even for densities as high as 10,000 gm/cc showing the importance of ignition temperature in thermonuclear fusion. For central ignition, the code has been modified to include the burn propagation into the outer cold

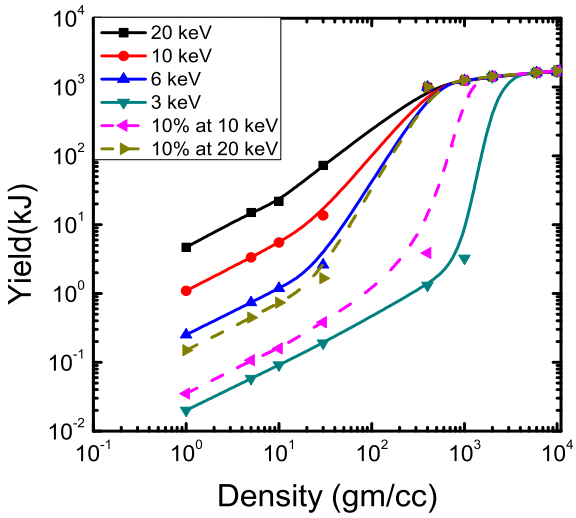

Figure 4: Yield vs. density for 10 μg DT pellets having various initial temperatures.

fuel, bootstrap heating and subsequent increase in fusion reactions leading to higher gain in fusion energy. Comparison with the results of a one-dimensional 3T Lagrangian hydrodynamics code [8] shows good agreement which supports the fact that though the zero dimensional model lacks spatial resolution, tracking the number densities and energetics of the nuclides is sufficient for obtaining the energy released in fusion [9]. The dotted curves show the same for central ignition with only inner 10% of the pellet at 10 and 20 keV respectively.

Chapter 4

Radiant energy transport plays an important role in determining the state and motion of the medium. In the earlier chapters, radiation interaction has been considered in terms of Bremstrahlung and inverse Compton scattering only. It is possible to analyze radiation interaction in a more rigorous manner by solving the time dependent radiation transport equation. The time dependent non-equilibrium radiation transport equation is non linearly coupled to the material energy equation [10], [11]. Also the material properties have complex dependence on the independent variables. As a result, the time dependent thermal radiation transport problems are commonly solved numerically. Several numerical methods are in use for this purpose,

namely the discrete ordinates, finite volume, Monte Carlo, hybrid stochastic-deterministic, or the approximate methods like the Eddington approximation, heat conduction or the diffusion approximations. Benchmark results for test problems are necessary to validate and verify the numerical codes [2]. Analytical solutions producing explicit expressions for the radiation and material energy density, integrated densities, leakage currents, etc. are the most desirable. In the literature, considerable amount of efforts have been applied for solving the Radiation Transport problem analytically. Marshak obtained a semi-analytical solution by considering radiation diffusion in a semi infinite planar slab with radiation incident upon the surface [12]. Assuming that the radiation and material fields are in equilibrium, the problem admits a similarity solution to a second order ordinary differential equation which was solved numerically. The results were extended for non-equilibrium radiation diffusion by assuming that the specific heat is proportional to the cube of the temperature. This assumption linearized the problem providing a detailed analytical solution. Using the same linearization, 3T radiation diffusion equations were solved for spherical and spherical shell sources in an infinite medium. All available results on the non-equilibrium radiative transfer problems in planar and spherical geometry consider systems having infinite or semi-infinite extension. Benchmarks involving finite size systems have been limited either to the heat conduction or equilibrium diffusion approximation [13]. In this chapter, new benchmark results have been generated for validating and verifying radiation diffusion codes in both planar and spherical geometries. Analytical solution to the non-equilibrium Marshak diffusion problem in a planar slab, sphere and spherical shell of finite thickness is presented. Using two independent methods namely the Laplace transform method and the eigen function expansion method, the radiation and material energy densities are obtained as a function of space and time. The variation in integrated energy densities and leakage currents are also studied. In order to linearize the radiation transport and material energy equation, the heat capacity is assumed to be proportional to the cube of the material temperature. The steady state energy densities show linear variation along the depth of the planar slab, whereas non-linear

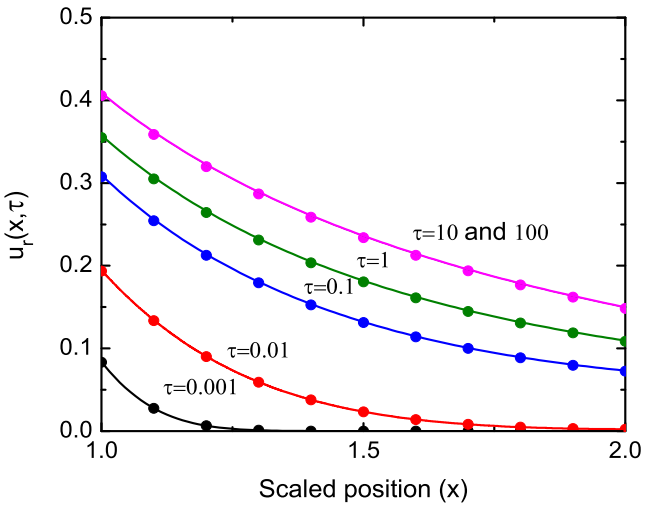

Figure 5: Transient analytical (symbols) and numerical (line) radiation energy densities in a spherical shell with radiation incident on the inner surface.

dependence is observed for the spherical shell. The analytical energy densities show good agreement with those obtained from finite difference method using small mesh width and time step. As a representative of the obtained results, we show scaled radiation energy densities for a spherical shell in figure 5. Initially, the material energy density is found to lag behind the radiation energy densities and finally equilibrate as time proceeds.

Chapter 5

The zero dimensional model is successful in obtaining the appropriate yields and reaction dynamics going on in time. However, to study more complex processes like shock propagation in ICF plasmas, pellet implosion and explosion either in a direct drive fusion or via x-rays in a hohlraum for the indirect drive, the actual spatial variation is to be considered. Thus, to have a better understanding of the processes taking place in a thermonuclear plasma, at least one dimensional hydrodynamic simulation study need to be performed. In this chapter, a fully implicit one dimensional Lagrangian hydrodynamic code has been developed in planar, cylindrical and spherical geometries. The medium is divided into a number of meshes and Lagrangian differ-

ential equations for conservation of mass, momentum and energy are solved in each mesh. All the meshes are connected and the velocities at the end of the time step are obtained by solving a tri-diagonal system of equations. The hydrodynamic system of equations are closed by using the equation of state (EOS) corresponding to the material. As the melting curve of the elements play an important role in the early stages, we have studied the melting curve of Cu and Al and the effect of dopants on the melting point using classical molecular dynamic simulations (included in appendices C and D respectively). The code is used to obtain the results for Sod's shock tube problem in planar geometry [14], Sedov's self similar point explosion problem in spherical geometry [15] and Noh's problem in both spherical and cylindrical geometries [16]. For the high energy density systems, the flow of energy from radiation to matter cannot be neglected and the total energy of the material changes because of radiation interaction in addition to that due to hydrodynamic compression. In order to describe properly the dynamics of the radiating flow, it is necessary to solve the full time-dependent radiation transport equation as very short time scales corresponding to a photon flight time over the mean free path are to be considered [10]. Two methods commonly used are non-equilibrium diffusion theory and radiation heat conduction approximation [17]. The former is valid for optically thick bodies, where the density gradients are small and the angular distribution of photons is nearly isotropic. The conduction approximation is only applicable when matter and radiation are in local thermodynamic equilibrium, so that the radiant energy flux is proportional to temperature gradient, and for slower hydrodynamics time scales. Use of Eddington's factor for closing the first two moment equations is yet another approach followed in radiation hydrodynamics. The full radiation transport equation has been solved using the discrete ordinates method [18]. The time dependent radiation transport equation for one group model is solved by discretizing it in angle and space. The angular difference coefficients and the weight attached to the angles (obtained according to Gauss quadrature) define the angular discretization whereas the finite difference version in space is obtained by integrating over a cell. Together with the exponential difference

scheme, the fluxes for all the meshes are obtained using the vacuum boundary condition and the symmetry of the flux at the centre of the sphere. The rate of radiation energy absorbed by unit mass of the material in each of the fixed mesh is finally obtained. The code is then used to study the Marshak wave problem in planar and spherical geometry. Su and Olson [19] derived an analytical solution of the non-equilibrium Marshak wave problem in a one-dimensional planar geometry in the diffusion approximation. The non-equilibrium Marshak wave problem consists of a semi-infinite, purely absorbing, and homogeneous medium occupying $0 \leq z \leq \infty$. The medium is at a zero temperature with no radiation field present at time t<0. At time t = 0, a time independent radiative flux F_{inc}= c/4 impinges upon the surface at z = 0. Opacity is assumed to be a constant independent of temperature and the specific heat is proportional to the cube of the temperature, i.e., C_V=α T^3. As a representative of these results, we show the scaled radiation and material energy densities as functions of position in the slab at different times for $\varepsilon = 0.1$ in figure 6. For numerical simulation we have chosen opacity σ_a =100 cm^{-1} and mesh width $\Delta z = 10^{-3}$cm in order to maintain $\sigma_a \Delta z = 0.1$. Comparison with the analytical results shows good agreement after a large time, whereas there is slight disagreement at earlier times. As the analytical results are obtained for the Marshak diffusion problem whereas our results employ the full radiation transport, slight difference at earlier times is expected because of larger penetration for diffusion approximation. An analytical solution is derived for the steady state Marshak diffusion in spherical geometry with the plasma having a constant opacity (σ_a =5.58 cm^{-1}) and neglecting the heating and cooling rates. Steady state scaled radiation temperatures within the sphere obtained from the radiation transport code are compared to the analytical solution.

Chapter 6

In this chapter, the radiation transport and hydrodynamics codes described in chapter 5 are coupled together to obtain a fully implicit radiation hydrodynamics code. The coupled radiation hydrodynamics code is applicable when the radiative transfer and the interaction between the

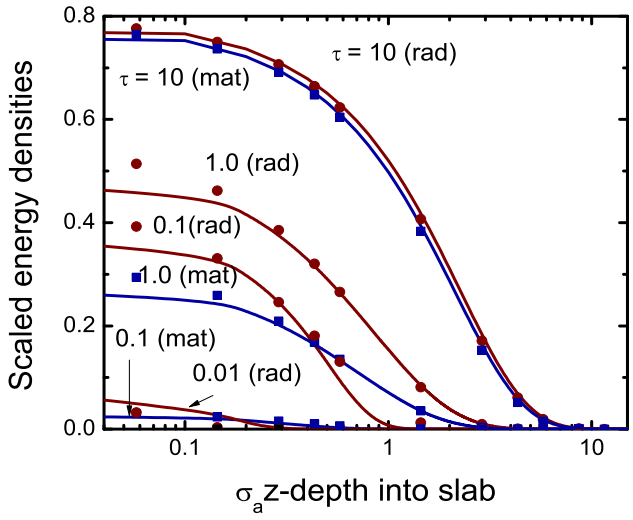

Figure 6: Linear plot of the radiation energy density and material energy density as functions of position in the slab at different times. The symbols represent the analytical solutions.

radiation and the material have a substantial effect on both the state and motion of the medium [17]. The radiation energy density and pressure are negligible in comparison to those corresponding to the materials for non-relativistic radiation hydrodynamics. However, the radiant heat transfer in the medium is significant because the radiant energy flux is comparable to the material energy flux. Thus the continuity equation and the equation of motion remains unchanged as the radiant energy density and the work done by the radiation pressure forces are neglected. A term describing the radiation absorption and emission is introduced into the energy equation. The solution method is described in the thesis in detail and is clearly depicted in the flowchart given in figure 7. The time step index is denoted by ‘nh’ and ‘dt’ is the time step taken. The iteration indices for electron temperature and total pressure are expressed as ‘npt’ and ‘npp’ respectively. ‘Error1’ and ‘Error2’ are the fractional errors in pressure and temperature respectively whereas ‘eta1’ and ‘eta2’ are those acceptable by the error criterion.

Using this radiation hydrodynamic code, the problem of shock propagation in Al foil is studied in planar geometry. In the indirect drive inertial confinement fusion, high power laser

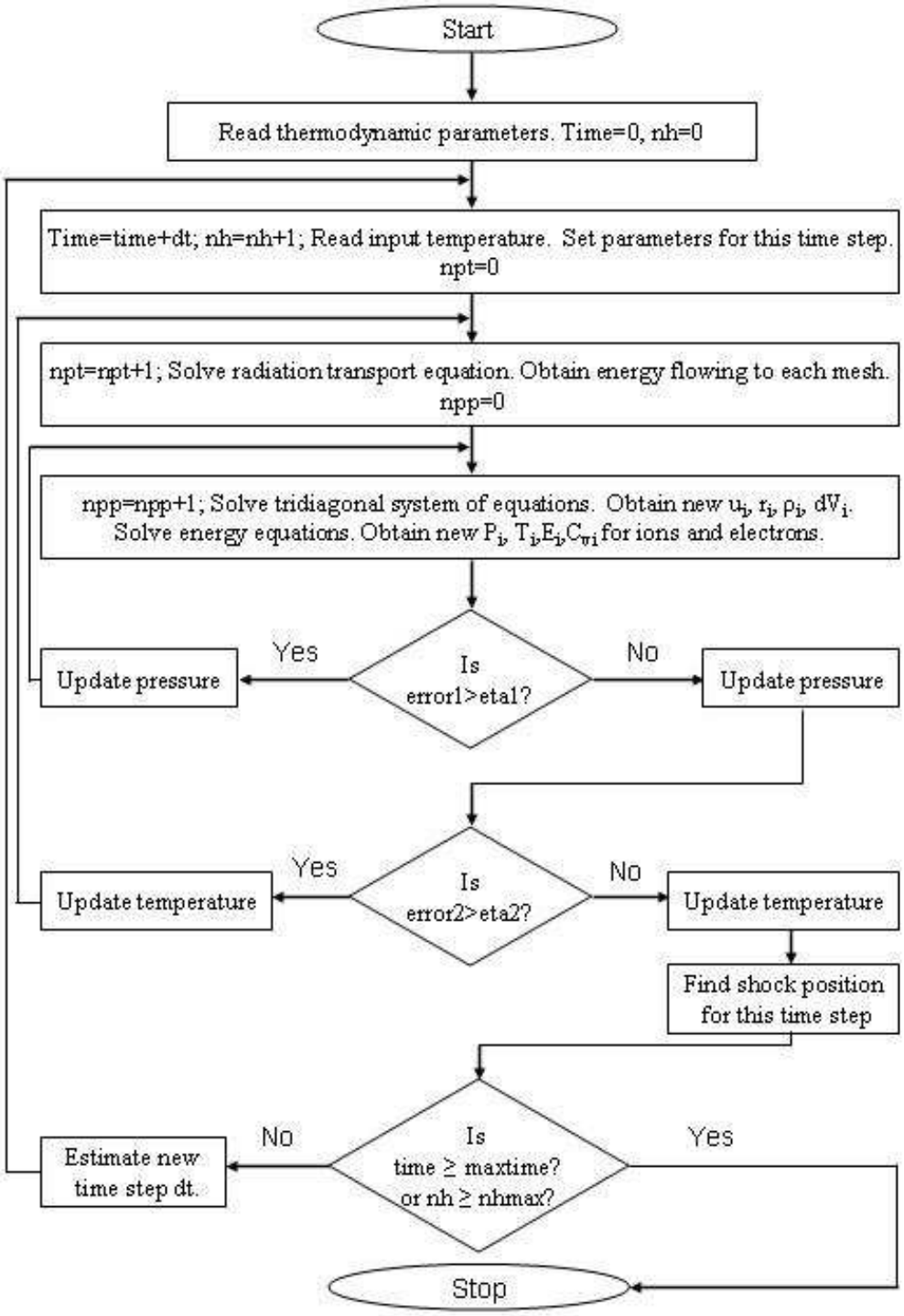

Figure 7: Flowchart of the radiation hydrodynamics code.

beams are focused on the inner walls of high Z cavities or hohlraums, converting the driver energy to x-rays which implode the capsule. If the x-ray from the hohlraum is allowed to fall on an aluminium foil over a hole in the cavity, the low Z material absorbs the radiation and ablates generating a shock wave. Using strong shock wave theory, the radiation temperature in the cavity T_r can be correlated to the shock velocity u_s. The scaling law derived for aluminium is $T_r = 0.0126 u_s^{0.63}$, where T_r is in units of eV and u_s is in units of cm/s for a temperature range of 100-250 eV [20]. Comparison between the numerically obtained shock velocities for different radiation temperatures and the scaling law for aluminium show good agreement in the temperature range where the scaling law is valid. The point explosion problem with heat conduction is also studied in spherical geometry. P. Reinicke and J. Meyer-ter-Vehn (RMV) analyzed the problem of point explosion with nonlinear heat conduction for an ideal gas equation of state and a heat conductivity depending on temperature and density in a power law form [21]. The problem combines the hydrodynamic (Sedov) point explosion with the spherically expanding nonlinear thermal wave. The RMV problem is a good test to determine the accuracy of coupling two distinct physics processes: hydrodynamics and radiation diffusion. We generate the results for the point explosion including radiation interaction using our fully implicit radiation hydrodynamics code. As a representative of these results, we show the normalized density, pressure, velocity and temperature obtained from our radiation hydrodynamic code in figure 8. The kink in ρ/ρ_1 and a sharp drop in T/T_1 at a distance of 0.57 cm are observed which shows that the heat front lags behind the shock front in this case. The smooth variation of temperature near the origin shows the effectiveness of radiative energy transfer from regions of high temperature. But for the unperturbed power law density profile ahead of the shock front, profiles of other variables are somewhat similar to point explosion problem without heat conduction.

Asymptotic convergence analysis is performed for conducting verification analysis of the code. The asymptotic convergence rate quantifies the convergence properties of the software implementation (code) of a numerical algorithm for solving the discretized forms of continuum

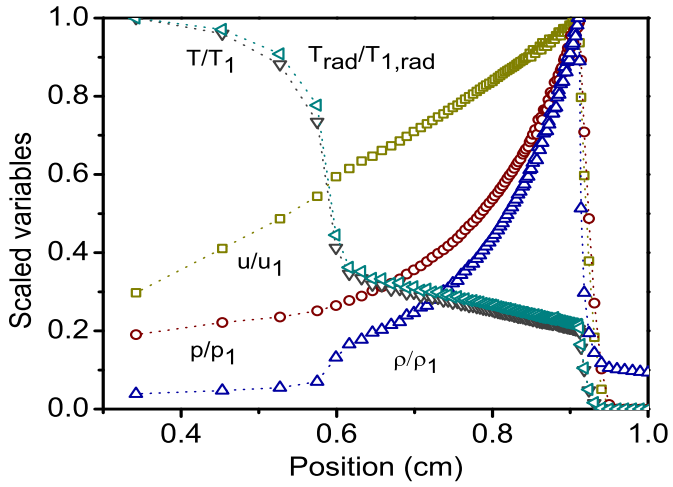

Figure 8: Profiles of the scaled thermodynamic variables at t = 4.879 ns for the point explosion problem including radiation interaction for $\gamma = 5/4$. Total energy 16.9×10^{16} ergs is deposited at $t = 0$ in the innermost mesh.

equations [22]. Our code verification for both planar and spherical cases consider the global mass-wise and temporal convergence separately. Spatial as well as temporal convergence rates are $\sim$1 as expected from the difference forms of mass, momentum and energy conservation equations.

Chapter 7

Finally, we conclude the thesis in this chapter. The studies carried out and the important results obtained are summarized. The limitations and the future scope of the work is also discussed.

Four appendices have been included at the end of the thesis:

1. Adaptive Cash-Carp Runge Kutta (RK) method for solving the ODEs.

2. Error arising from the discretization of mass, momentum and energy conservation equations.

3. Melting curve of metals using classical molecular dynamics (MD) simulations.

4. Effect of Site Selective Ti substitution on the Melting Point (MP) of CuTi Alloys.

In summary, the important highlights of the work are as follows: An improved model of charged particle and neutron energy deposition is developed to analyze internal T breeding and thermonuclear burn characteristics of compressed D-T pellets. Also, new analytical benchmark results have been derived for radiation diffusion in planar and spherical geometries. A fully implicit 1D Lagrangian hydrodynamics code is developed and applied to significant problems in ICF. We have performed Classical MD simulations to obtain MP of metals and alloys as they are important for EOS determination and use in hydrodynamic simulations.

References:

1. J. J. Duderstadt and G. A. Moses, Inertial Confinement Fusion, John Wiley and Sons 1982.
2. L. Ensman, The Astrophysical Journal 424 (1994) 275.
3. O. N. Krokhin and V. B. Rozanov, Soviet J. of Quantum Electronics 2 (1973) 93.
4. R. S. Cooper and F. Evans Phys. Fluids 18 (1975) 332.
5. F. Evans Phys. Fluids 16 (1973) 1011.
6. S. Eliezer, Z. Henis, J. M. Martinez-val and I. Vorbeichik, Nucl. Fusion 40 (2000) 95.
7. H. S. Bosch and G. M. Hale, Nucl. Fusion 32 (1992) 611-31.
8. J. S. Clarke, H. N. Fisher, and R. J. Mason, Phys. Rev. Lett. 30 (1973) 89.
9. G. S. Fraley, E. J. Linnebur, R. J. Mason, and R. L. Morse, Phys. Fluids 17 (1974) 474.
10. D. Mihalas and B. W. Mihalas, Foundations of Radiation Hydrodynamics, Oxford University Press, New York, 1984.

11. G. C. Pomraning, The Equations of Radiation Hydrodynamics, 1st Ed. Oxford, Pergamon Press, 1973.

12. R. E. Marshak, Phys. Fluids. 1 (1958) 74.

13. A. Liemert and A. Kienle, J. Quant. Spectros. Radiat. Transf. 113 (2012) 559.

14. G. A. Sod, J Comput. Phys. 27 (1978) 1.

15. L.I.Sedov, Similarity and Dimensional Methods in Mechanics (Moscow, 4 th edition 1957. English transl. (M.Holt, ed.), Academic Press, New York, 1959)

16. W. F. Noh, J. Comput. Phys. 72 (1978) 78.

17. Y. B. Zeldovich and Y. P. Raizer, Physics of Shock Waves and High Temperature Hydrodynamic Phenomena, Academic Press, New York, 1966.

18. E. E. Lewis and W. F. Miller, Jr., Computational Methods of Neutron Transport, John Wiley and Sons, New York, 1984.

19. B. Su and G. L. Olson, J. Quant. Spectros. Radiat. Transfer 56 (1996) 337.

20. R. L. Kauffman, et.al, Phys. Rev. Lett. 73 (1994) 2320.

21. P. Reinicke and J. Meyer-ter-Vehn, Phys. Fluids A 3 (1991) 1807.

22. J. R. Kamm, W. J. Rider, J. S. Brock, Consistent Metrics for Code Verification, Los Alamos National Laboratory, LA-UR-02-3794 (2004).

List of Figures

List of Tables

1 Introduction

1.1 Motivation

Hot dense plasmas are encountered in high-energy density physics scenarios such as Inertial Confinement Fusion (ICF), strong explosions, astrophysical systems, shock waves, etc. Such systems are obtained at pressures exceeding 1Mbar and energy densities greater than $10^{12}\mathrm{erg/cm}^3$ [1]. They consist of three kinds of particles, namely the ions, electrons and photons [2]. The self equilibration times of ions and electrons are much smaller ($\sim 10^{-13}$ s) compared to the time taken by ions and electrons to attain the same temperature ($\sim 10^{-9}$ s) [3, 4]. So, distinct energy and temperature is assigned to the constituent species and the evolution of energy density for such a plasma is described using the three-temperature (3T) equations. However, if the time scale of interest is larger than the electron-ion temperature equilibration time, a single material temperature can be defined for the two components of the plasma fluid. When energy is deposited locally, it gives rise to local perturbations in density, pressure and temperature. These disturbances then propagate away from the source by transporting energy to the other regions [3]. The two principal energy transport modes are hydrodynamic motion (sound waves or shock waves) and radiation transport (RT). The fusion products in ICF (charged particles and neutrons) mainly deposit their energy to the ions through collisions whereas radiation energy preferably heats the electrons.

The equations for conservation of mass, momentum and energy along with the Equation of State (EOS) define the hydrodynamic motion of the plasma [4]. The radiation transport equation defines the radiation intensity as a function of space and time in the interacting medium. Solving the problem of radiation transport is difficult because the equation is integro-differential in character and can take various forms (elliptic, parabolic or hyperbolic) in different mediums [5]. Simplifying assumptions are made to obtain analytical solutions in some cases. As the photon density is a function of seven independent variables; three for position, two for direction of flight, one for energy and one for time, simulating real radiation transport problems is challenging. Significant storage and computational complexity is involved in resolving all of these dimensions on a spatial, temporal, angular and energy grid. Radiative phenomena occur on time scales that differ by many orders of magnitude from those characterizing hydrodynamic flow. This leads to significant computational challenges in the efficient modeling of radiation hydrodynamics [6, 7].

The motivation behind the work in this thesis is to study the aforementioned energy transport mechanisms in detail. New analytical solutions have been derived and numerical codes developed for the purpose.

1.2 Theoretical background

Dynamical phenomena such as shock waves, radiation waves, material ablation, etc. are essential for the production of high-energy density conditions, to the achievement of inertial fusion and to the simulation of astrophysical phenomena [2]. The models and codes developed in this thesis are applied to hot dense plasmas generated in the laboratory using inertial confinement fusion approach. In this section, we discuss the physical processes taking place in an ICF plasma. The techniques and methodologies for studying energy flow through hydrodynamic motion and radiation transport is also introduced. Analytical solutions available only for a few

simple problems are discussed and various numerical methods in use for the complicated ones are compared. We also discuss about atomistic simulation for obtaining the melting points of metals and alloys which plays a major role in choosing the proper material properties (EOS) at lower temperatures, for example, the initial stages of ICF.

1.2.1 Concept of inertial confinement fusion

Hans Bethe discovered in 1931 that nuclear fusion is the primary energy source of stars. As the conventional fuels have limited resources, nuclear fusion has the potential of turning into the energy source of the future because of its ecological and safety advantages [8]. In order to fuse two light nuclei which are positively charged and strongly repel each other, high temperatures are required to overcome the Coulomb repulsion [3]. In 1961, a Livermore scientist, John Nuckolls, realised that the powerful light beam of a pulsed laser could be used to achieve the energy densities necessary to produce very high compressions. Inertial Confinement Fusion (ICF) is a process where thermonuclear fusion reactions are initiated in a fusion fuel (e.g., DT, DD, DHe^3, etc) by compressing it to tremendous densities and temperatures by focusing high power laser or charged particle beams on the surface of the pellet or via X-rays in a hohlraum [1]. The inertia of the fuel pellet helps in confining it long enough to produce more fusion energy than is expended in heating and containing it. The twin requirements of heating and confinement is represented by the Lawson criterion which is obtained by balancing the fusion energy release against the energy investment in ablating, compressing, heating the fuel to thermonuclear temperatures and the energy lost through radiation. If n is the ion density and τ is the confinement time, the Lawson criterion states that $n\tau > 10^{14}$ s/cc for D-T reactions and $n\tau > 10^{16}$ s/cc for D-D reactions when the reaction rate is evaluated at suitable temperatures (10 keV for D-T and 100 keV for D-D). An alternative way of defining the Lawson criterion is the product of the fuel density ρ and pellet radius R. Efficient thermonuclear burn occurs if $\rho R > 3\mathrm{g/cm}^2$ so that 1/3 rd of the fuel pellet burns before its disassembly. The most important

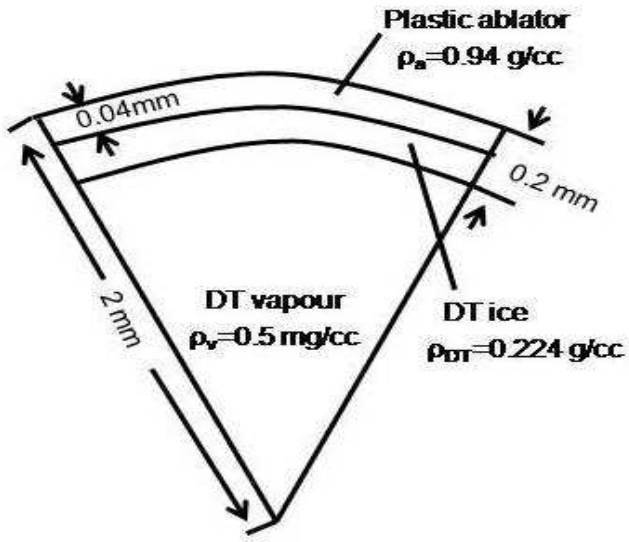

Figure 1.1: Target sector of a typical ICF pellet.

quantity determining whether a reaction would take place or not is the reaction cross-section (σ) which measures the probability per pair of particles for the reaction to occur. Cross section is defined as the number of reactions per target nucleus per unit time when the target is hit by a unit flux of projectile particles. If n_A is the ion density of species A while n_B is the density of species B, then the rate at which fusion reactions occur is given by $R_{AB} = n_A n_B < \sigma v >$ where $< \sigma v >= \int\int f(\vec{v}_A) f(\vec{v}_B) \sigma(v_{rel}) v_{rel} d\vec{v}_A d\vec{v}_B$ indicates an average over the velocity distributions of both species with the relative velocity $v_{rel} =\mid \vec{v}_A - \vec{v}_B \mid$. The velocity distributions characterizing a plasma fuel in thermal equilibrium at a temperature T is given by the Maxwell-Boltzmann distribution $f(\vec{v}) = (\frac{m}{2\pi k_B T})^{3/2} \exp(-\frac{mv^2}{2k_B T})$ where k_B is the Boltzmann's constant.

A typical ICF pellet consists of a hollow shell capsule with an outer ablator layer of 1.67 mg plastic and a fuel layer of 1.68 mg (cryogenic) solid DT. The outer radius of the shell is slightly less than 2 mm and its aspect ratio is about 10 as shown in figure 1.1. The central cavity is filled with DT vapour, which forms the ignition hot spot after the implosion [9].

The various stages followed in inertial confinement fusion process are:

1. **Laser/Particle beam or x-ray driven ablation**

   When laser light is incident on the outer surface of a fusion pellet, the material is transformed into the plasma state and expands outward from this surface. The density of the plasma is highest close to the capsule surface and lower further away. If the density of the plasma is greater than the critical density, laser beam can no more penetrate into the capsule. The driver energy is transported from the outer regions of the plasma corona into the ablation surface via classical electron conduction, hot (superthermal) electron transport and radiation transport. Particle beams on the other hand penetrate in the medium upto their range and deposit their energy into the ions and electrons. An alternative is the indirect drive approach in which laser energy is first absorbed in the inner walls of the hohlraum coated with high Z material which emits x-rays. The x-rays fall on the capsule at the centre of the hohlraum and leads to the ablation of the outer surface. 70-80 $\%$ of the laser light is converted to x-rays.

2. **Ablative shock compression**

   As the outer surface of the pellet ablates, due to rocket motion an ablative pressure is generated inwards. A spherical shock wave moves inwards and compresses the fuel. In order to obtain higher shock compressions, a series of weak shocks rather than one strong shock is used.

3. **Thermonuclear ignition and burn propagation**

   Thermonuclear ignition and burn of a plasma occurs when internal heating by fusion products exceeds all energy losses such that no further external heating is necessary to keep the plasma in the burning state [9]. For a DT pellet containing equal amounts of D_1^2 and T_1^3, the ignition temperature is ~ 5 keV or higher. Ignition can be achieved through various schemes, viz. volume ignition, hot spot/ central ignition and fast ignition. In volume ignition, the whole of the fuel is compressed and heated to fusion conditions at

the end of the compression phase so that ignition starts in the whole pellet. The driver energy requirement is very high $\sim$ 60MJ for volume ignition. In hot-spot or central ignition concept, the fuel moves inwards with increasing velocities as the driver deposits its energy. The result of this acceleration is that the inner part of the fuel is compressed into a higher temperature adiabat ($\sim$ 5-10 keV) than the outer part of the fuel ($\sim$ 1 keV). Both parts will be compressed to high densities, but the inner hot spot will be slightly less dense than the outer part. In the hot spot concept the burn of the fusion material begins in the central hot spot. The alpha particles are mainly responsible for depositing the fusion energy into the outer layers. If the hot spot size is greater than the critical radius, a thermonuclear burn front propagates into outer cold fuel producing high gain. At these very high densities, the energetic alpha particles produced in the DT fusion reactions are absorbed in this central region heating it to still higher temperatures and causing the fuel to burn even more rapidly. As the central spark burns, alpha particles are deposited in the adjacent fuel, bringing it to ignition temperatures. This process continues, leading to a thermonuclear burn wave that propagates outward into the cold compressed fuel surrounding the ignited pellet core, consuming the fuel in a very rapid thermonuclear microexplosion. After only a few picoseconds a significant fraction of the imploded pellet fuel has burned before the pellet disassembles. As the compression of hot material is more energy consuming than the cold material, and because less material needs to be heated in the hot spot scheme, it provides better gains with the additional advantage that the external dense and cold fuel layer provides better confinement. In the fast ignition scheme, the capsule is precompressed by a conventional long pulse (ns) laser to produce a high density core ($\rho \sim$ 300-400 g/cc) [10]. The core is then ignited using a short pulse (fs) ultra intense ($\sim 10^{20}\ \mathrm{W/cm^2}$) particle beam. The advantage of the fast ignitor concept is that compression and ignition are separated, thereby enabling higher gain from a lower driver energy input, possibly allowing higher tolerances in target fabrication. The

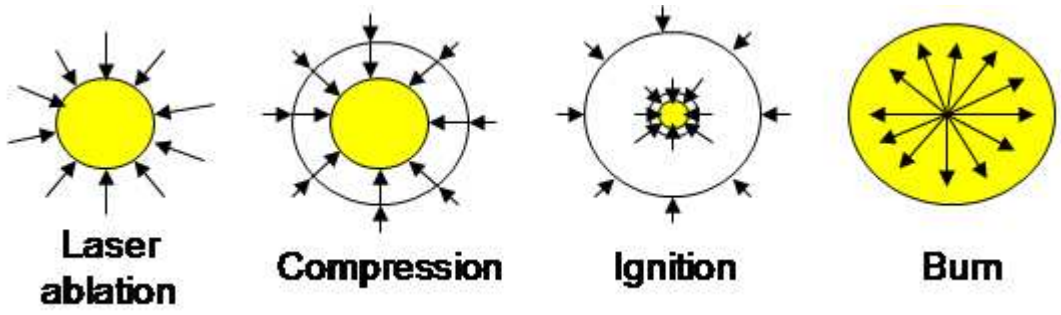

Figure 1.2: Various stages followed in Inertial Confinement Fusion.

various stages of an ICF pellet implosion and burn is shown in figure 1.2.

The most important fusion reactions occuring in a thermonuclear plasma containing D_1^2 and T_1^3 are:

$$D_1{}^2 + D_1{}^2 \longrightarrow He_2{}^3 + n_0{}^1 + 3.269 \quad MeV, \tag{1.1}$$

$$D_1{}^2 + D_1{}^2 \longrightarrow T_1{}^3 + p_1{}^1 + 4.033 \quad MeV, \tag{1.2}$$

$$D_1{}^2 + T_1{}^3 \longrightarrow He_2{}^4 + n_0{}^1 + 17.589 \quad MeV, \tag{1.3}$$

$$He_2{}^3 + D_1{}^2 \longrightarrow He_2{}^4 + p_1{}^1 + 18.353 \quad MeV. \tag{1.4}$$

DT reaction has the highest reactivity in the whole temperature interval below 400 keV. The second most probable reaction is DD at temperatures below 25keV while it is DHe^3 for 25 $\leq$ T $\leq$ 250 keV as shown in figure 1.3. Advanced fusion fuels involving hydrogen isotopes and light nuclei (such as helium, lithium and boron) are particularly interesting as they do not involve any radioactive fuels or neutrons and only releases charged particles. One such reaction is the proton-boron reaction

$$p_1{}^1 + B_5{}^{11} \longrightarrow 3He_2{}^4 + 8.6 \quad MeV, \tag{1.5}$$

which has reactivity equal to that of DHe^3 at about 250 keV and that of DT at about 400keV.

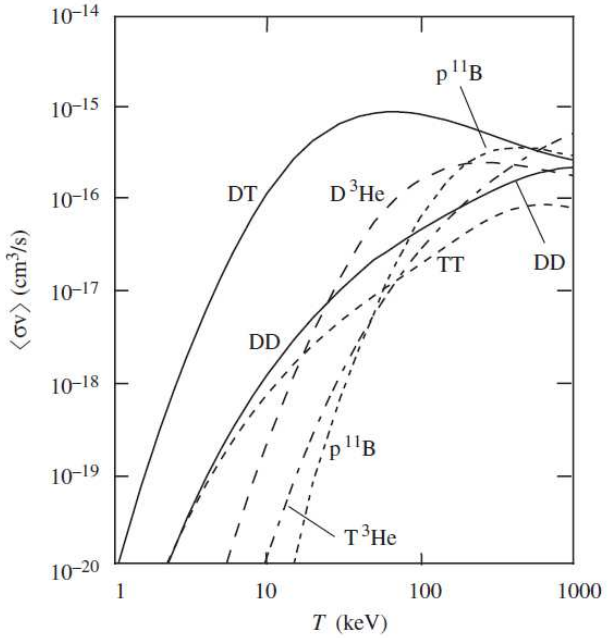

Figure 1.3: Maxwell-averaged reactivity Vs. temperature for reactions of interest to inertial confinement fusion. Reproduced with permission from reference [9].

A key point in achieving fusion is a homogeneous compression, which means aiming for a perfectly symmetric implosion. But it is difficult to achieve a spherically symmetric compression because of the instabilities. Among hydrodynamic instabilities, the Rayleigh-Taylor (RT) and Richtmyer-Meshkov (RM) instabilities play a role in ICF. Out of these two, the RT instability is the most dangerous one. The RT instability occurs when a lighter fluid tries to accelerate a denser fluid. During the spherical implosion of an ICF pellet, RT instability arises when the ablated low density plasma pushes a cold high density fuel inwards. Also, at the end of the implosion, the pressure in the hot fuel increases thereby decelerating the pusher shell imploding the fuel mass. If the fuel density is lower than the pusher density, the pusher material mixes into the fuel due to RT instability thus affecting the thermonuclear burn of the fuel [11],[12],[13].

1.2.2 Hydrodynamics

The state of a moving fluid whose thermodynamic properties are known can be defined in terms of velocity, density, and pressure as functions of position and time [4]. The continuity equation or the equation of mass conservation signifies that the change in density within a volume element is because of fluid flow into or out of this element. If ρ is the density and $\vec{u}$ is the velocity, then the above equation is

$$\frac{D\rho}{Dt} + \rho\vec{\nabla}.\vec{u} = 0, \tag{1.6}$$

where $\frac{D}{Dt} = \frac{\partial}{\partial t} + \vec{u}.\vec{\nabla}$. The equation of conservation of momentum is equivalent to Newton's second law and attributes the acceleration to the applied forces. If P is the pressure, then

$$\rho\frac{D\vec{u}}{Dt} = -\vec{\nabla}P. \tag{1.7}$$

The equation of conservation of energy is equivalent to the first law of thermodynamics and states that the change in specific internal energy E of a given fluid element is a result of the work of compression done on the element by the surrounding medium, and the energy generated by external sources.

$$\frac{DE}{Dt} + P\frac{dV}{dt} = Q, \tag{1.8}$$

where $V = 1/\rho$ is the specific volume, Q is the energy generated by external sources per unit mass of the material per unit time. In order to close the above system of five equations with six unknowns, the thermodynamic properties of the fluid are assumed to be known through the Equation of State (EOS) given by $P = P(\rho, T)$ and $E = E(\rho, T)$.

The hydrodynamic equations become acoustic equations describing the propagation of sound waves in the limiting case, where changes in density $\Delta\rho$ and pressure ΔP accompanying the

fluid motion are very small in comparison with the average values of density ρ_0 and pressure P_0, and where the flow velocities are small in comparison with the speed of sound c_s. The energy of a sound wave is a quantity of second order, proportional to the square of the amplitude ρc_s^2 [1]. If the medium is disturbed very strongly in an extremely short time, as in the case of energy deposition by driver, the disturbance propagates into the neighbouring regions approximately with the speed of sound which is proportional to the square root of the density, $c_s \sim \rho^{1/2}$. Hence the disturbance propagates faster in the high density regions than in low density regions. The perturbation profile of a fast propagating disturbance travelling into a lower density region steepens resulting in a shock wave which is supersonic w.r.t. the medium ahead of it [8]. Figure 1.4 a) shows a shock wave moving with speed u_s in a fixed frame of reference with a static medium ahead of the shock. It is convenient to work in the frame fixed to the shock wave so that the medium ahead of the shock moves towards it with the shock speed as shown in figure 1.4 b). The conservation laws are then given in one dimensional form by

$$\frac{\partial \rho}{\partial t} + \frac{\partial}{\partial x}(\rho u) = 0, \tag{1.9}$$

$$\frac{\partial}{\partial t}(\rho u) + \frac{\partial}{\partial x}(P + \rho u^2) = 0, \tag{1.10}$$

$$\frac{\partial}{\partial t}(\rho E + \rho \frac{u^2}{2}) + \frac{\partial}{\partial x}[\rho u(E + \frac{u^2}{2} + \frac{P}{\rho})] = 0. \tag{1.11}$$

In the limit of an infinitesimally thin discontinuity, we obtain the Rankine-Hugoniot relations

$$\rho_0 u_0 = \rho_1 u_1, \tag{1.12}$$

$$P_0 + \rho_0 u_0^2 = P_1 + \rho_1 u_1^2, \tag{1.13}$$

$$E_0 + \frac{P_0}{\rho_0} + \frac{u_0^2}{2} = E_1 + \frac{P_1}{\rho_1} + \frac{u_1^2}{2}. \tag{1.14}$$

The Hugoniot curve is locus of all thermodynamic states obtained by single shock compressions. As illustrated in the P-V diagram of figure 1.5, the Hugoniot curve lies above that of

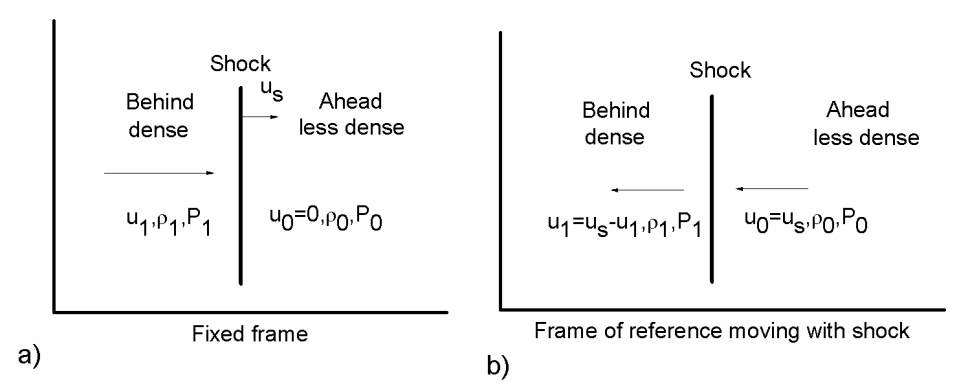

Figure 1.4: Hydrodynamic variables behind and ahead of a shock wave in a) fixed frame of reference and b) frame of reference moving with the shock.

adiabatic compression. The area under the curve is equivalent to the work done to compress the material. While the temperature and pressure across the shock will rise indefinitely with the strength of the shock, the compression or density change approaches an asymptotic limiting value of $\frac{\rho_1}{\rho_0} = \frac{\gamma+1}{\gamma-1}$. For a monoatomic gas (specific heat ratio $\gamma = C_P/C_V = 5/3$), this ratio is 4, for a diatomic gas ($\gamma = 7/5$), it is 6, and so on. In reality, at high temperatures and pressures, the specific heats and specific heat ratios are no longer constant because of molecular dissociation and ionization. Even in this case, the density ratio remains finite and it does not exceed 11-13. As a series of weak shocks approach an adiabat, the work done to compress the fuel is lower. An isentropic compression also prevents in heating the fuel so that it is easier to contain the fuel for a longer time.

Numerical problems involving simple gas flows can be solved analytically and used as tests for validating hydrodynamic simulation codes written for studying more complicated processes [14]. A steady plane-parallel adiabatic shock, with its step function changes in density and temperature [7] is a classic test problem for hydrodynamic codes with the analytical solution known (Rankine Hugoniot). Such a shock can be produced numerically by a piston, i.e., by giving the inner zone boundary a constant outward velocity. Another standard hydrodynamics test is the shock tube [15]. The point explosion problem admits self-similar analytical solution

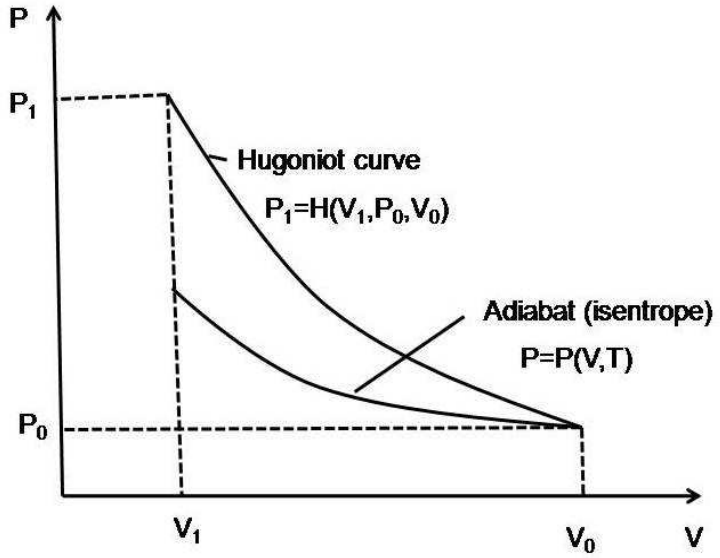

Figure 1.5: P-V diagram for shock and adiabatic compression.

in spherical geometry [16]. The Noh problem has also been solved analytically for spherical and cylindrical cases [17].

Hydrodynamic simulation is performed by dividing the system to be studied into meshes, discretizing the hydrodynamic equations in these regions and solving them numerically [18]. As the meshes are attached to the moving material in the Lagrangian formulation, the mass within a mesh remains constant. However, in the Eulerian scheme, the meshes are fixed in space with material moving from one mesh to the other. The Lagrangian scheme is conceptually simple and the entire time history of all the field variables at a material point can be easily tracked and obtained. Though it is difficult to track the time history data of any material point or boundary, large deformations can be easily handled in the Eulerian scheme. The equations can be discretized either using finite difference (FD), finite volume (FV) or the finite element (FE) methods [19]. In the finite difference method (FDM), derivatives are approximated as finite difference using Taylor's expansion and neglecting higher order terms. Local truncation errors are introduced in the solution depending on the order of term neglected in the series. In finite volume method (FVM) on the other hand, instead of pointwise approximations on a grid,

average integral value on a reference volume is considered using Gauss theorem. The FVM is applicable to integral form of conservation law and is a natural choice for heterogeneous material as each grid cell can be assigned different material parameters. In finite element method (FEM), the variables are expanded in terms of basis function with a partition of the domain in a finite dimensional subspace. It is flexible and applicable for complicated geometries. For the Lagrangian finite difference method, one may use the explicit scheme in which the thermodynamic variable at the present time step is obtained from a knowledge of the previous time step values. Implicit schemes on the other hand rely on solving a system of equations at each time step as the variable values are dependent not only on previous time step values but also on the present values of the adjacent meshes [20]. Approximating the time step as a backward difference leads to explicit scheme whereas forward or central difference results in an implicit scheme. Although the explicit scheme is computationally simple, it has a serious drawback that the time step should be very small (less than the time taken by a sound signal to traverse the grid spacing) for the solutions to be stable [21]. As a simultaneous system of equations is solved in the implicit scheme, it takes more computational time per time step than the explicit scheme.

The molecular structure of a fluid results in dissipative processes like viscosity and heat conduction which creates an additional, non-hydrodynamic transfer of momentum and energy. They appear only where there are large gradients in the flow variables as in a shock front and are responsible for the increase in entropy. All numerical procedures describing shock structures must have some degree of dissipation like viscosity or heat conduction to control the numerical instability by smearing the shock within a few mesh widths. The Von-Neumann procedure [22] artificially adds a new viscous term whereas the high resolution methods use an upwind scheme based on the exact Godunov [23] or an approximate [24] Riemann solver. The high resolution methods inherently possess the needed dissipation through the type of differencing operator used to approximate the governing equation [25].

1.2.3 Radiation transport

In the radiation field, energy is carried by point massless particles called photons. Each photon travels with the speed of light c and carries an energy hν where h is the Planck's constant and ν is the frequency of the electromagnetic field associated with the photon. A radiation field in space is described by the distribution of the intensity of radiation w.r.t., frequency, to space and to the direction of radiant energy transfer and is expressed by the photon distribution function $f(\nu, \vec{r}, \vec{\Omega}, t)$ [4]. Then the number of photons in the frequency interval ν to $\nu + d\nu$, contained at time t in the volume element $d\vec{r}$ at the point $\vec{r}$, and having a direction of motion within an element of solid angle d$\vec{\Omega}$ about a unit vector $\vec{\Omega}$ is given by $f(\nu, \vec{r}, \vec{\Omega}, t)d\nu d\vec{r}d\vec{\Omega}$. The spectral radiation intensity $I_\nu(\vec{r}, \vec{\Omega}, t) = h\nu c f(\nu, \vec{r}, \vec{\Omega}, t)d\nu d\vec{r}d\vec{\Omega}$ represents the radiant energy in a unit spectral interval, passing per unit time through unit area, with direction of energy propagation contained within unit solid angle about the vector $\vec{\Omega}$. The photons interact with the background material by emission and absorption during electronic transitions from one energy state to another in atomic systems, like electron-ion plasmas. All electronic transitions can be divided into three groups using the continuity criterion or the discreteness of the energy spectrum of the initial and final states of the atomic system. These groups are bound-bound, bound-free and free-free transitions. A free electron traveling through the electric field of an ion in an ionized plasma can either emit a photon without losing all its kinetic energy and remain free or it can absorb a photon and acquire additional kinetic energy. These free-free transitions are called Bremsstrahlung and has a continuous emission and absorption spectra. For a fully ionized plasma, Bremsstrahlung transitions are the most dominant mechanism of radiation absorption and emission. The radiative transfer equation is a partial differential equation for the radiation intensity and describes a non-equilibrium radiation field. Thermodynamic equilibrium in matter is usually established very rapidly, and it is therefore possible to consider the material to be in a state of local thermodynamic equilibrium (LTE) at each point of space and at each instant of time. The state of the material is then described by two parameters, such as temperature and

density. The time dependent, multi-frequency, non-equilibrium radiation transport equation is given by

$$\frac{1}{c}\frac{\partial I(\nu,\vec{r},\vec{\Omega},t)}{\partial t}+\vec{\Omega}\cdot\vec{\nabla}I(\nu,\vec{r},\vec{\Omega},t)+(\sigma_a(\vec{r},\nu,T)+\sigma_s)I(\nu,\vec{r},\vec{\Omega},t)= \sigma_a(\nu,\vec{r},t)B(\nu,T)+\sigma_s\int\int I(\nu',\vec{r},\vec{\Omega}',t)d\vec{\Omega}'d\nu', \tag{1.15}$$

along with the material energy equation

$$C_V(\vec{r},T)\frac{\partial T(\vec{r},t)}{\partial t}=\int\int\sigma_a(\vec{r},\nu,T)[I(\vec{r},\vec{\Omega}',\nu\prime,t)-B(\nu',T)]d\vec{\Omega}'d\nu', \tag{1.16}$$

where the Planck's function is $B(\nu,T)=\frac{8\pi h\nu^3}{c^2}\frac{1}{exp(h\nu/k_BT)-1}$. σ_a is the opacity (inverse of absorption mean free path) and σ_s is the scattering cross-section. Here, speed of light $(c) = 2.9979 \times 10^8$ m/s, Planck's constant $(h) = 6.62 \times 10^{-34}$ J.s and Boltzmann's constant $(k_B) = 1.38 \times 10^{-23}$ J/K. Though the temperature is most familiarly expressed in Kelvin (K), it is convenient to express it in keV where 1eV=11,600K.

The external source of radiation enters through the boundary conditions. The first term in eqn. [1.15] is a time rate of change term. This time derivative is related to several loss terms in phase space on the LHS and gain terms on the RHS. The second term on the LHS is a loss term due to photons streaming out of an element of phase space. The third term is a loss term due to photons absorbed into the background material and scattered out of the phase space. The absorption term appears as a source term in the material energy equation. The first term on the RHS is a radiative source due to the background temperature of the material (hence a corresponding loss term appears on the RHS of the other equation). The last term represents increase in photon intensity in the direction $\vec{\Omega}$ due to scattering from other angles [5].

Analytical solutions of the above equations are difficult except for the simplest of cases. The equation for the specific intensity is integro-differential in nature and non-linearly coupled to the material equation so that devising an appropriate numerical scheme is also difficult. To generate

solutions to physically interesting problems, it is necessary to make some approximations.

The most common approximation is the multi frequency approximation in which the frequency variable is divided into G groups and group specific intensity, group Planck function, etc. are defined. The group averaged absorption opacities are formed by multiplying with physically meaningful weighting functions. The Planck mean opacity is obtained by weighting against the Planck's function and is accurate in the optically thin, emission dominated limit.

$$\sigma_P(\vec{r},T) = \frac{\int \sigma_a(\vec{r},\nu)B(\nu,T)d\nu}{\int B(\nu,T)d\nu}. \tag{1.17}$$

The Rosseland mean opacity is valid for an optically thick system in which the specific heat is small and the speed of light is large.

$$\sigma_R(\vec{r},T) = \frac{\int \frac{\partial B(\nu,T)}{\partial T}d\nu}{\int \frac{1}{\sigma_a(\vec{r},\nu)}\frac{\partial B(\nu,T)}{\partial T}d\nu}. \tag{1.18}$$

The Rosseland mean is accurate if the problem is highly diffusive and slowly varying in time. The Rosseland and Planck means may vary by an order of magnitude in different temperature density regimes. In this thesis, the group averaged Rosseland opacities have been used as they have been shown to be more accurate in the presence of strong temperature gradients.

The next level of simplification is the Grey approximation wherein the opacities are frequency independent so that the above RT equation may be integrated over all frequencies to obtain the Grey radiation transport equation.

In the diffusion approximation, the angular variable is eliminated by finding equations for the first two terms in a spherical harmonics expansion. It is also assumed that the angular dependence of the specific intensity is adequately represented by the first two terms of a Legendre polynomial expansion. Assuming a constant radiative flux, the diffusion equation is obtained. This approximation is valid for problems where the flux is nearly isotropic.

In the heat conduction approximation, the radiation intensity at a space point in the medium

is assumed to be at the local material temperature at that point. In this case the equilibrium heat conduction equation is used for obtaining energy transfer.

The other approximations normally used are the quasidiffusion approximation, Eddington approximation, etc.

Radiation transport and diffusion equations are either solved deterministically using P_N, S_N, etc. methods or stochastically by Monte Carlo methods. In the deterministic methods, the radiation transport equations are discretized in space, time and angle and then solved iteratively. Several numerical methods are in use for solving the radiation transport equation, namely the discrete ordinates [26], finite volume [27], Monte Carlo [28], hybrid stochastic-deterministic [29],[30], or the approximate methods like the Eddington approximation [31], heat conduction [32] or the diffusion approximations [33], [34], [35]. Nevertheless, analytical approaches have decisive advantages regarding accuracy, speediness and numerical implementation compared to numerical methods and are important for their validation [36]. Also, better insight can be gained through the mathematical form of an analytical solution compared to a discrete numerical solution. The orthogonal expansion technique [37], Green's function approach [38], Laplace transform and separation of variables [39], finite integral transform method, etc. are some of the commonly used methods for obtaining analytical solutions to the radiation conduction and diffusion problems in several systems.

1.2.4 Atomistic simulation

An essential input to the hydrodynamic simulations is a knowledge of the material EOS which usually takes the form of pressure P and energy E as functions of density ρ and temperature T. The pressure and internal energy of a material can be considered as the sum of cold and thermal terms. The cold or elastic terms (P_c and E_c) are related to the interaction forces between the atoms of the material and is important below 1 eV. The thermal term is related to the temperature T of the body and consists of contribution from the lattice ions (P_{TL} and E_{TL}) and electrons

(P_{TE} and E_{TE}) [40]. Therefore, the EOS can be written as

$$P = P_c + P_{TL} + P_{TE}, \tag{1.19}$$

$$E = E_c + E_{TL} + E_{TE}. \tag{1.20}$$

Depending on the composition, density and temperature, contribution from each of the terms vary [41]. For low Z materials, ions make a significant contribution at any densities and temperatures. For high Z materials, at temperatures above $\sim$ 10 eV, most of the pressure comes from the free electrons and the key variable is the ionization state. The thermodynamic properties of a system can be obtained from molecular dynamics by considering the interaction between the atoms of the system. At the initial states of ICF implosion when phase transition from the solid to liquid phase occurs, accurate knowledge of the melting point for various pressures is essential for choosing the proper EOS to be used for the hydrodynamic simulation. It has been observed both experimentally and through numerical simulation that the outer ($\sim 20\mu m$) of the ablator material (e.g., Be) will be melted by radiation preheat, with subsequent material melted by the initial shock [42]. The solid liquid phase boundary commonly known as the melting curve is an important part of the phase diagram and is widely used in high pressure physics, inertial confinement fusion, material science, astrophysics and geophysical sciences. Melting curves of metals can be obtained experimentally by the Diamond Anvil Cell (DAC) which is a static method or by the dynamic methods consisting of laser or ion beam driven ablation, etc. However it is difficult to design experiments because of the high pressures and temperatures involved. Various simulation methods like the Lindemann's law, dislocation mediated melting, classical and ab initio Molecular Dynamics (MD) etc. are in use to complement the experiments. The classical MD method [43] is very convenient as a large number of atoms compared to ab initio MD can be simulated using an empirical potential which properly describe the interatomic interactions.

In molecular dynamics simulations, the time evolution of a system of interacting particles

is determined by the integration of the equations of motion. Such measurements allow the computation of relevant macroscopic variables such as kinetic or potential energy, pressure, diffusion constants, transport coefficients, structure factors, spectral density functions, distribution functions, etc. [44]. In classical molecular dynamics (MD) simulation, the trajectories of atoms and molecules are determined by numerically solving the Newton's equations of motion for a system of interacting particles where the forces between the particles is determined by the interatomic potentials. The most widely used model to calculate the interactions is the Lenard-Jones (LJ) potential which is a pair potential. However, pair potentials are insufficient for describing the properties of metals as the cohesive energy of a crystal is mainly described by the many-body interactions or by a volume dependent part [45]. Pure pair interactions also imply that the surface relaxes outwards instead of inwards as is observed in experiments. The embedded atom method (EAM) potential circumvents these problems by viewing each atom in a solid as embedded in a host comprising all the other atoms. The total energy is the sum of the embedding and pair potential energy [46]. EAM potentials are generated by fitting to experimental data or results of ab initio calculations. According to the EAM theory, the total energy of a system of N atoms is described as the energy required to embed these N atoms into the homogeneous electron gas caused by surrounding atoms plus a correction of energy from two-body interactions [47]. Thus this total internal energy can be expressed as

$$E_{tot} = \sum_i F_i(\rho_i) + \frac{1}{2}\sum_i \sum_{j \neq i} \phi_{ij}(r_{ij}), \tag{1.21}$$

where $F_i(\rho_i)$ is the embedding energy required to place atom i in an electron density ρ_i, $\phi_{ij}(r_{ij})$ is the two-body potential between atoms i and j, r_{ij} is the separation distance related to the specified pair of atoms i and j, and ρ_i denotes the host electron density at atom i due to all other

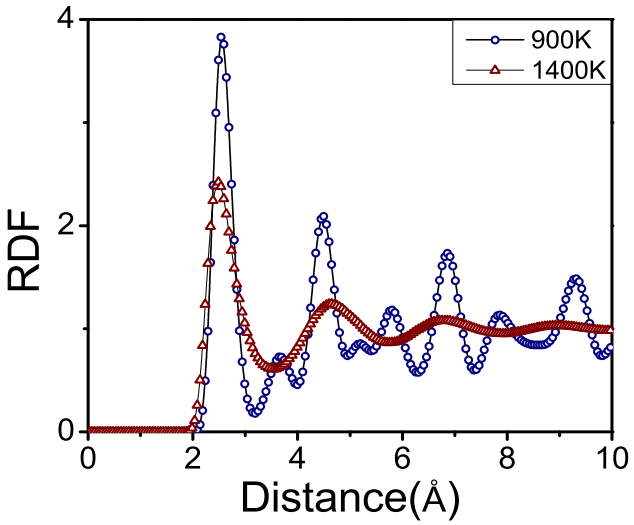

Figure 1.6: Radial distribution function (RDF) of Cu before and after melting.

atoms and is given by

$$\rho_i = \sum_{j \neq i} f(r_{ij}), \tag{1.22}$$

where $f(r_{ij})$ is the electron density of the individual atom j.

The melting point is determined using the one-phase method [48] wherein the melting point is identified from sharp increase in atomic volume, diffusion coefficient and energy as temperature is varied. Also, as the long range order is lost once melting occurs, the height of the first peak of RDF decreases drastically and RDF ≈ 1 after 2-3 small humps. The RDF describes how the atomic density varies as a function of distance from the atom and is given by $g(r) = n(r)/(4\pi r^2 \Delta r \rho)$ where $n(r)$ is the number of atoms at a distance r within a shell of thickness Δr and ρ is the average number density. The heights of the peaks signify the number of first, second, etc., nearest neighbours. Similarly the position of RDF peaks reflects the neighbour distances. Earlier, a similar study of alloying bcc Fe with Si has been performed and the increase in melting point is explained in terms of the RDF peak height [49]. For Cu, at a tem-

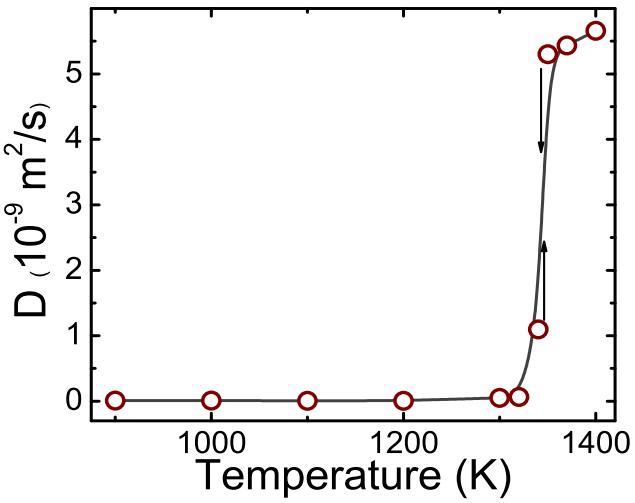

Figure 1.7: Jump in the diffusion coefficient (D) of Cu at melting point.

perature of 1440K, the intermediate and long distance peaks of Cu-Cu RDF are seen to slowly merge out indicating that melting has occured (figure 1.6). The jump in diffusion coefficient for Cu is shown in figure 1.7 wherein the melting point 1340K is indicated using arrows.

1.3 Survey of the work done prior to this thesis

Plasma heating by charged particles and neutrons, energy exchange between ions and electrons and radiative losses are the primary mechanisms determining the ignition conditions in a thermonuclear plasma [3]. These processes have been modelled under varying degrees of rigor in detailed computer simulations of both inertial and magnetic confinement fusion schemes [9, 50]. Experimental proof of these theoretical predictions measuring the energy loss of heavy ions in fully ionised hydrogen plasma were given by Hoffmann *et al* [51]. It is well known that most of the energy of the fusion products should be deposited to the ions in order to obtain higher fusion gains [52]. However, increase of electron temperature, either due to direct energy deposition or via energy transfer from ions, leads to radiation losses from the plasma. The fraction of the

charged particle energy that is absorbed by the ICF pellet is an important parameter determining the ignition condition. For pellet sizes comparable to the thermalization range of fusion products, a fraction of the energy will escape the pellet. Krokhin and Rozanov [53] calculated the thermalization distance and energy leakage probability of a charged particle in a fully ionized plasma at a uniform temperature and density by considering energy transfer to electrons only. Later, Cooper and Evans improved this calculation by including energy transfer to ions within the small angle binary collision approximation [54].

Advanced fusion fuels like $\mathrm{DD}, \mathrm{DHe}^3, \mathrm{DLi}^7$, etc. are very appealing from the point of view of radiological cleanliness, but they are very difficult to exploit because of their ultrahigh ignition temperatures [52]. Recently Eliezer *et al* [55] have shown that the ignition temperature in deuterium fusion targets can be significantly reduced with the addition of very small amounts of tritium [56]. This is because DT fusion has a larger cross section in comparison to DD fusion at lower temperatures. There is also a possibility of a catalytic regime for tritium burning where external addition of tritium is not needed because the amount needed is bred internally. However, Gsponer and Hurni [57] showed that by taking radiation effects such as inverse Compton scattering fully into account, the maximum burn temperature of a highly compressed DD pellet is reduced from about 300 keV to only 100 keV. This decrease in ion temperature leads to a substantial reduction in the burn fraction. They concluded that if the radiation effects are properly taken into account, internal T breeding does not occur in the pellet. Fraley *et al* studied thermonuclear burn in DT microspheres at high densities and obtained numerical results characterizing the burn for a broad range of initial conditions using a 1D 3T Lagrangian simulation code and cross-checked the results with a separate non-equilibrium code which solves radiation transport using Monte Carlo method [60].

Analytical solutions to radiation transport involve solving the radiation diffusion or transport equation through a steady interacting medium. In the literature, considerable amount of efforts have been applied for solving the Radiation Transport problem analytically. Two com-

mon diffusion problems having analytical solutions are evolution to radiative equilibrium and radiative cooling of a sphere [14]. Marshak obtained a semi-analytical solution by considering radiation diffusion in a semi infinite planar slab with radiation incident upon the surface [61]. Assuming that the radiation and material fields are in equilibrium, the problem admits a similarity solution to a second order ordinary differential equation which was solved numerically [62]. The results were extended for non-equilibrium radiation diffusion by assuming that the opacity is temperature independent and the specific heat is proportional to the cube of the temperature [63], [64]. This assumption linearized the problem providing a detailed analytical solution. As the radiative transfer codes are meant to handle an arbitrary temperature dependence of the material properties, the obtained solutions serve as useful test problems [65], [66], [67]. Using the same linearization, 3T radiation diffusion equations were solved for spherical and spherical shell sources in an infinite medium [2]. All available results on the non-equilibrium radiative transfer problems in planar and spherical geometry consider systems having infinite or semi-infinite extension. Benchmarks involving finite size systems have been limited either to the heat conduction or equilibrium diffusion approximation [68], [69], [36].

Radiation transport and its interaction with matter via emission, absorption and scattering of radiation have a substantial effect on both the state and the motion of materials in high temperature hydrodynamic flows occurring in inertial confinement fusion (ICF), strong explosions and astrophysical systems [4]. Researchers are continuously working on devising new numerical schemes for simulating radiation hydrodynamics. In order to describe properly the dynamics of the radiating flow, it is necessary to solve the full time-dependent radiation transport equation as very short time scales ($t_R \sim l/c$ or $t_\lambda \sim \lambda_p/c$ corresponding to a photon flight time over a characteristic structural length l, or over a photon mean free path λ_p) are to be considered [70]. Two methods commonly used are non-equilibrium diffusion theory [71], [72] and radiation heat conduction approximation [4]. The former is valid for optically thick bodies, where the density gradients are small and the angular distribution of photons is nearly isotropic. The conduction

approximation is only applicable when matter and radiation are in local thermodynamic equilibrium, so that the radiant energy flux is proportional to temperature gradient, and for slower hydrodynamics time scales [4]. Use of Eddington's factor for closing the first two moment equations is yet another approach followed in radiation hydrodynamics [73]. Earlier studies on the non-equilibrium radiation diffusion calculations show that the accuracy of the solution increases on converging the non-linearities within a time step and increasing benefit is obtained as the problem becomes more and more nonlinear and faster [34], [35]. Niem developed an implicit Lagrangian formulation to handle multi-material hydrodynamic problems involving shocks and rarefaction waves [74]. Although high resolution methods for simulating pure hydrodynamic flows are well established [75], their extension to coupled radiative regimes have only recently begun [71],[73]. P. Reinicke and J. Meyer-ter-Vehn (RMV) analyzed the problem of point explosion with nonlinear heat conduction for an ideal gas equation of state and a heat conductivity depending on temperature and density in a power law form [76]. The problem combines the hydrodynamic (Sedov) point explosion with the spherically expanding nonlinear thermal wave. The RMV problem is a good test to determine the accuracy of coupling two distinct physics processes: hydrodynamics and radiation diffusion. Later on, Shestakov presented the results of point explosion with heat conduction using a coupled hydrodynamic diffusion code [77]. Bates *et al* compared the time accuracy and convergence properties of three, mixed explicit-implicit schemes for simulating nonrelativistic, radiative hydrodynamic phenomena in the equilibrium diffusion limit [72]. Verification of codes are also performed using the asymptotic convergence analysis [78] or modified equation analysis [79].

1.4 Scope of the thesis

The work in this thesis focuses on understanding the mechanisms of energy transport by charged particles, neutrons, photons, etc. in an interacting medium. The temperatures we consider are

high enough so that material stresses and strains do not play any role in the dynamics of the system. We have improved the present energy deposition model of charged particles by including large angle Coulomb scattering, nuclear scattering and collective plasma effects. Thermalization distance is reduced resulting in lesser energy escaping from the pellet. We also resolve the controversy regarding the possibility of internal tritium breeding. It is observed that on using the improved energy deposition model, internal tritium breeding occurs even on accounting for inverse Compton losses. Based on T breeding ratio and deuterium burn fraction, the optimum pellet parameters have been obtained for which T is bred internally. The zero dimensional model is next used to obtain the fusion yields in DT pellets having a range of densities and temperatures and are found to agree with the results of 3T Lagrangian hydrodynamics code. The zero dimensional model is also modified in order to apply it to central ignition where only a central region of the pellet is heated to ignition temperatures, burn wave propagates outwards into the cold fuel, thus producing fusion energies. As the interaction of radiation with the medium is one of the most important energy transport mechanism, radiation transport has been analyzed in detail in this thesis. Radiation has been considered as a stream of photons interacting with the medium by getting absorbed, scattered and emitted. The radiation transport equation defines the time and space dependent radiation intensity. Because of its coupling to the material, it is integro-differential and highly non-linear. In this thesis, we have made some simplifying assumptions to obtain detailed analytical solutions. This highly enriches our understanding of this important energy transport mechanism. The Eigenfunction expansion method has been successfully applied to the non-equilibrium radiation diffusion problem in finite systems. The Laplace transform method also independently provides the same analytical results. As the diffusion approximation is valid for small density gradients and for a medium whose properties are isotropic, this is a reasonable approximation for optically thick plasmas. Near the edges, suitable boundary conditions take care of the anisotropy. Based on the implicit Lagrangian formulation of Kiem, a fully implicit 1D Lagrangian hydrodynamics code is developed. The code

is used for studying the shock tube problem in planar, point explosion problem in spherical and Noh problem in both spherical and cylindrical geometries. A numerical radiation diffusion code is developed based on the finite difference method and results are generated for a finite and infinite planar slab, and a spherical shell. The radiation transport equation is solved using the discrete ordinates method and the code is used for studying the Marshak wave problem in both planar and spherical geometries. A fully implicit radiation hydrodynamics code is developed by coupling hydrodynamics and radiation transport together. This code is applied to the problem of shock propagation in Al foil and shock velocities are compared with empirical values. Similarly, the point explosion problem with heat conduction is studied and compared with Meyer ter Vehn's problem. Asymptotic convergence analysis of the code is next performed to verify it. Finally, in the appendix, melting curve of metals Cu and Al have been determined using classical molecular dynamics simulation. As Equation of State (EOS) is an integral part of the radiation hydrodynamics code, selection of the proper EOS is important for obtaining correct results. The EOS applicable in the solid phase cannot be used for the liquid phase and vice versa. As a result, a knowledge of the melting points for various pressures, i.e., melting curve of materials is essential. Effect of alloying Cu with Ti is also studied: melting point is found to decrease linearly for random and microstructure doping, however the arrangement of the initial structure determines the same for selective doping.

2 Energy deposition of charged particles and neutrons in an inertial confinement fusion plasma

2.1 Introduction

Charged particles mainly deposit energy in a plasma via elastic Coulomb interactions with ions and electrons, though nuclear scattering also contributes to ion heating. For low density and high temperature plasmas, Coulomb interactions can be approximated as small angle binary collisions [80], however, large angle scattering needs to be included for high densities and low temperatures [82]. The effect of nuclear interactions have not been taken into account previously as it is negligible for small scattering angles. However, when the incident charged particle energy is large, as in the case of the proton produced in $D^2 - He^3$ reaction, and for higher pellet densities, the effect of nuclear scattering is important [83]. Collective plasma effects arise when the plasma is considered as a dielectric medium without bringing into picture its internal particle behaviour and the energy loss in a plasma from distant collisions is obtained with the continuum approximation [84]. In this chapter, we generalize the calculation of energy leakage probability to include nuclear scattering, large angle Coulomb scattering and collective plasma effects. In general, these effects reduce the thermalization distance in the plasma and increase the fraction of energy deposited to ions. We also develop a simple approach for energy deposition by neutrons due to nuclear interaction with the ions.

2.2 Theoretical model

In this section, we develop the theoretical methodology for obtaining the total stopping power and energy leakage probability of fusion products in a fully ionized plasma. A multigroup model for energy deposition by neutrons is also developed.

2.2.1 Charged particle energy deposition

The charged fusion products interact with the ions and electrons in the medium via small and large angle Coulomb scattering in addition to nuclear interactions.

2.2.1.1 Coulomb scattering

The Fokker-Planck equation which was originally derived to treat the Brownian motion of molecules, has been widely used to evaluate the collision term of the Boltzmann equation for describing small-angle binary collisions of the inverse-square type of force [81]. Considering the effects of both large and small angle scattering, the energy loss per unit length of path of a fast charged particle of mass m, laboratory frame energy $E = \frac{1}{2}mv^2$ and charge Ze, which moves through a hot plasma with ions of mass m_1, charge $Z_1 e$ and number density n_1 at a temperature T_1 is given by [82]

$$\frac{dE}{dx} = -2\pi n_1 Z^{\,2} {Z_1}^2 e^4 \frac{m}{m_1 E}(F_1(y_1)\ln\Lambda_b + \Theta({y_1}^2)\ln[1.123(y_1)]), \tag{2.1}$$

where

$$F_1(y_1) = \phi(y_1) - (1 + \frac{m_1}{m})y_1\phi'(y_1) + \frac{m_1}{m\ln\Lambda_b}\phi(y_1), \tag{2.2}$$

with

$$y_1{}^2 = \frac{m_1}{m}\frac{E}{k_B T_1}. \tag{2.3}$$

Collective plasma effects are represented by the second term of eqn. [2.1], namely

$\Theta(y_1{}^2)\ln[1.123\,(y_1)]$ where $\Theta(y_1{}^2)$ is a step function whose value is identically 0 for $y_1{}^2 \leq 1$ and 1 for $y_1{}^2 > 1$.

Further, k_B is the Boltzmann constant, $\phi(y_1) = 2\int_0^{y_1} \frac{e^{-\xi}\sqrt{\xi}d\xi}{\sqrt{\pi}}$ and $\phi'(y_1)$ are the error function and its derivative, respectively. The Coulomb logarithm term is defined as [82]

$$\ln \Lambda_b = \ln\left(\frac{\lambda_D}{d_{min}}\right). \tag{2.4}$$

The Coulomb logarithm is a measure of the importance of small-angle binary collisions relative to large-angle scattering. The large-angle scattering can be neglected only when the Coulomb logarithm is of order 10 or greater. However, it cannot be neglected for moderately coupled ICF plasmas in the intermediate regime ($2 \leq ln\Lambda_b \leq 10$). For the non-degenerate regime, the Debye length λ_D and minimum distance d_{min} are defined as

$$\lambda_D = \sqrt{\frac{k_B T_{elec}}{4\pi n_{elec} e^2}}, \tag{2.5}$$

where T_{elec} and n_{elec} are the electron temperature and number density respectively, and

$$d_{min} = \sqrt{p_\perp{}^2 + (\frac{\hbar}{2m_r v_{rel}})^2}. \tag{2.6}$$

Here, $\hbar = h/2\pi$ is the reduced Planck's constant and $p_\perp = \frac{ZZ_1e^2}{m_r v_{rel}^2}$ where m_r is the reduced mass

and v_{rel} the relative velocity. So d_{min} can be finally expressed as

$$d_{min} = \sqrt{\left[(\frac{ZZ_1e^2(m+m_1)}{2m_1E})^2 + (\frac{\hbar(m+m_1)}{2m_1\sqrt{2mE}})^2\right]}. \tag{2.7}$$

However, when considering the energy loss to electrons, d_{min} can be accurately approximated as

$$d_{min} = \sqrt{\left(\frac{ZZ_1e^2}{3k_BT_{elec}}\right)^2 + \left(\frac{\hbar}{2\sqrt{3k_BT_{elec}m_{elec}}}\right)^2}. \tag{2.8}$$

Similarly, since ${y_1}^2 \ll 1$ for electrons, $F_1(y_1)$ can be approximated as

$$F_1(y_1) \approx \frac{4}{3\sqrt{\pi}}{y_1}^3. \tag{2.9}$$

2.2.1.2 Nuclear scattering

In computing the energy deposition or loss by heavy charged particles in a plasma, in addition to the Coulomb interactions with the electrons and ions, nuclear forces elastic scattering plus nuclear Coulomb interference are also to be considered. The nuclear forces-nuclear Coulomb interference term is assumed to be independent of the temperature and density of the medium, the approximations are equivalent to the case when the target nuclei are at a temperature T=0. This approximation is good enough for the incident energies large compared to the target temperature.

The contribution to energy loss due to elastic nuclear scattering has been modeled in terms of stopping power [85], which can be written as

$$\frac{dE}{dx} = \frac{<\Delta E>}{\Lambda_T}, \tag{2.10}$$

where $<\Delta E>$ is the average energy loss per collision and the transport mean free path $\Lambda_T =$

$(n_1\sigma_T)^{-1}$. The transport cross sections σ_T is expressed as

$$\sigma_T = \frac{4\pi m m_1}{(m+m_1)^2}\int_{-1}^{1}\sigma_s(\nu)(1-\nu)d\nu, \tag{2.11}$$

where $2\pi\sigma_s(\nu)$ denotes the differential cross-section for scattering angle $cos^{-1}(\nu)$. Eqn. [2.10] implicitly assumes that energy loss via nuclear scattering also takes place predominantly due to small angle collisions. For the calculations reported in this paper, σ_T for different charged particles slowing down in a deuterium plasma is taken from Devaney *et al* [85].

2.2.1.3 Total stopping power

The total stopping power can be expressed as

$$\begin{aligned}\frac{dE}{dx} &= \left(\frac{dE}{dx}\right)_i^{(R)} + \left(\frac{dE}{dx}\right)_e^{(R)} + \left(\frac{dE}{dx}\right)_i^{(N)} \\ &= A_d(E)E^{-1} + A_e(E)E^{-1} + A_N(E)E,\end{aligned} \tag{2.12}$$

where the subscripts d, e and N denote Coulomb scattering from ions, electrons and nuclear scattering, respectively. The ionic term is explicitly given by

$$A_d(E) = \sum_j -2\pi n_j Z^2 {Z_j}^2 e^4 \frac{m}{m_j}(F_j(y_j)\ln\Lambda_{bj} + \Theta({y_j}^2)\ln[1.123(y_j)]). \tag{2.13}$$

The summation over j goes over all the types of ions in the pellet plasma. Similarly, the electronic and nuclear terms are

$$A_e(E) = -2\pi n_{elec} Z^2 {Z_e}^2 e^4 \frac{m}{m_{elec}}\frac{4}{3\sqrt{\pi}} \times \left(\frac{m_{elec}E}{mk_B T_{elec}}\right)^{3/2}\ln\Lambda_{be}, \tag{2.14}$$

$$A_N(E) = -\sum_j n_j\sigma_{Tj}. \tag{2.15}$$

The energy loss rate given by eqn. [2.12] can be used to determine all the parameters such as thermalization distance, energy leakage probability and fraction of energy deposited to ions as will be discussed in the following sections.

2.2.2 Neutron energy deposition

The rate of neutron interactions in a plasma is given by $n_1\sigma_t\phi$ where n_1 is the number density of ions, σ_t is the total cross-section for interaction of neutrons with nuclei and ϕ is the neutron flux [86]. In order to calculate the fraction of neutron energy deposited to the ions, we divide the energy range of neutrons from 17 to 0 MeV into $g_{max} = 30$ energy groups. Then for the g^{th} group,

$$n_1\sigma_{tg}\phi_g = P_c(g) \times S_g, \tag{2.16}$$

where $P_c(g)$ is the probability that a source neutron in g^{th} group will collide with the ions. The source of neutrons, S_g, in the g^{th} energy group, consisting of the external neutron source and the neutrons slowed down from higher energy groups, is:

$$S_g = \sum_{g\prime=1}^{g} n_1\sigma_{s\ g\prime\rightarrow\ g}\phi_{g\prime} + S_{ext\ g}, \tag{2.17}$$

where $\sigma_{s\ g\prime\rightarrow\ g}$ is the scattering cross-section for a neutron to change energy from group $g\prime$ to g. If a single neutron of energy E_0 is produced by fusion per unit volume per second in the ICF pellet, the fraction of energy deposited in the pellet is

$$f_k{}^j = \frac{1}{E_0}\sum_{g=1}^{g_{max}} n_1\sigma_{heating-g} \times \phi_g, \tag{2.18}$$

where $\sigma_{heating-g}$ is the heating cross-section of a neutron in the g^{th} group. The neutron flux ϕ_g of the g^{th} group is obtained from a knowledge of neutron fluxes of all the previous groups.

Using eqns. [2.16] and [2.17] we get

$$(n_1\sigma_{tg} - P_c(g)N_1\sigma_{s\ g\rightarrow\ g})\phi_g = P_c(g)(\sum_{g\prime=1}^{g-1} n_1\ \sigma_{s\ g\prime\rightarrow\ g}\phi_{g\prime} + S_{ext\ g}), \tag{2.19}$$

with the collision probability given by [87]

$$P_c(g) = 1 - \frac{3}{8(Rn_1\sigma_{tg})^3}[2(Rn_1\sigma_{tg})^2 - 1 + (1 + 2N_1\sigma_{tg}R)e^{-2n_1\sigma_{tg}R}], \tag{2.20}$$

where R is the pellet radius. The neutron flux in the first group is obtained by assuming that slowing down source to that group is zero as there are no neutrons of higher energy. Cross-sections for neutron interaction are taken from Barrett *et al* [88]. This multigroup neutron energy deposition model is used in the next chapter to estimate the fraction of neutron energy deposited in a fusion plasma.

2.2.3 Energy leakage probability

First of all, the distance traversed by the charged particle, $s(E_0, E)$, to slow down from energy E_0 to E is obtained from eqn. [2.12] as:

$$s(E_0, E) = \int_{E_0}^{E} dW/[A_d(W)W^{-1} + A_e(W)W^{-1} + A_N(W)W]. \tag{2.21}$$

We can now calculate the fraction of the charged particle energy escaping from the pellet of radius R. If the charged particle is produced with uniform probability in the sphere R, the escape probability can be calculated using the integral [53] (as obtained by Krokhin and Rozanov)

$$\eta = \frac{3}{2R^3}\int_0^R \rho^2 d\rho \int_{-1}^{1} d\mu \frac{E(r)}{E_0}, \tag{2.22}$$

where E_0 is the initial charged particle energy and E(r) the energy after traversing a distance

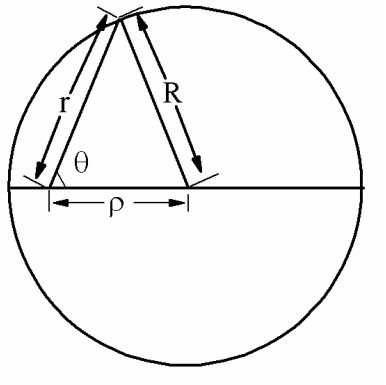

Figure 2.1: Charged particle leakage probability

r from the point of birth to the spherical surface. The parameter r can be expressed in terms of the radial distance ρ from the centre, the radius R and the cosine μ of the angle between the path and the line passing through the centre as shown in figure 2.1.

$$r = \rho\mu + \sqrt{R^2 - \rho^2(1-\mu^2)}. \tag{2.23}$$

To obtain $\frac{E}{E_0}$ as a function of r we solve the differential equation

$$\frac{dE}{dr} = A_d(E)E^{-1} + A_e(E)E^{-1} + A_N(E)E \tag{2.24}$$

numerically using the initial condition that $E(r) = E_0$ at r=0. We use quadratic interpolation for intermediate values of r for evaluating η.

2.3 Results and discussions

In figure 2.2, we show the energy of 3.5 MeV deuteron as a function of distance traversed in a deuterium plasma at temperature 0.1 MeV and number density $10^{\,26}/\mathrm{cm}^3$ for energy deposition via 1) Coulomb scattering only to electrons, 2) Coulomb scattering to both ions and electrons,

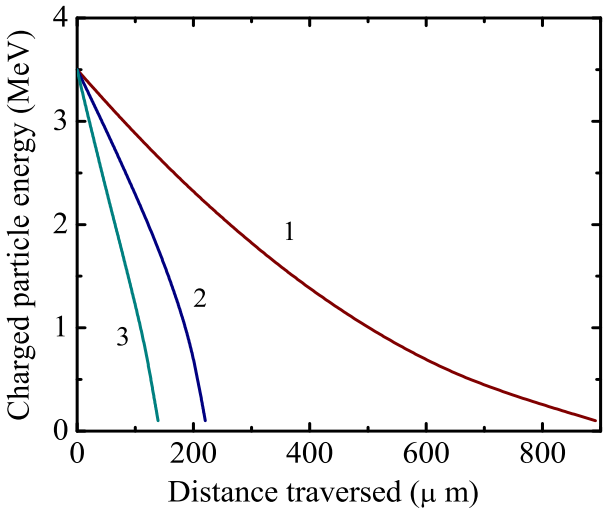

Figure 2.2: Energy of deuteron Vs. distance traversed in a deuterium plasma at temperature 0.1 MeV and ion number density $10^{26}/\mathrm{cm}^3$ for the three cases of energy loss: 1. only to electrons, 2. electrons and ions and 3. including nuclear scattering.

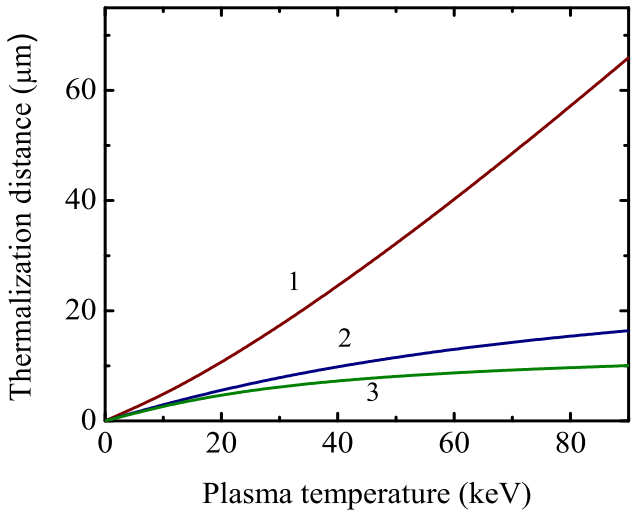

Figure 2.3: Thermalization distance of deuterons Vs. plasma temperature in a deuterium plasma of ion number density $10^{26}/\mathrm{cm}^3$ for the three cases of energy loss: 1. only to electrons, 2. electrons and ions and 3. including nuclear scattering.

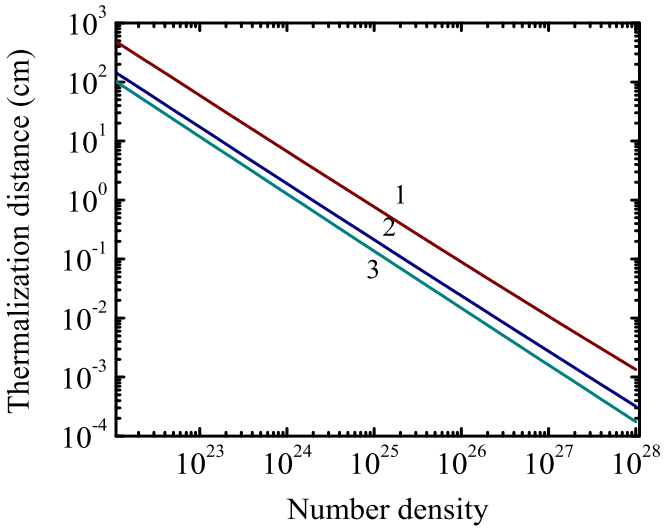

Figure 2.4: Thermalization distance of deuterons Vs. plasma ion density in a deuterium plasma at a temperature of 0.1 MeV for the three cases of energy loss: 1. only to electrons, 2. electrons and ions and 3. including nuclear scattering.

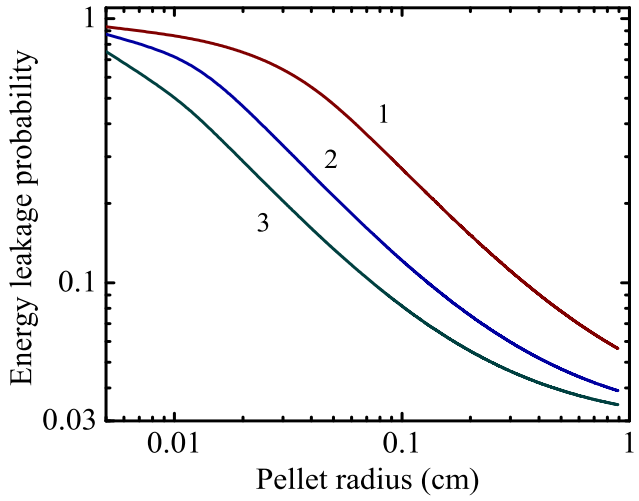

Figure 2.5: Energy leakage probability of deuterons Vs. pellet radius in a deuterium plasma at temperature 0.1 MeV and ion number density $10^{26}/\mathrm{cm}^3$ for the three cases of energy loss: 1. only to electrons, 2. electrons and ions and 3. including nuclear scattering.

and 3) nuclear as well as Coulomb scattering. Figure 2.3 and figure 2.4 show the thermalization distance, i.e., the distance traversed by the charged particle before attaining the background plasma temperature, as a function of the plasma temperature and number density respectively for the above three cases. Finally, figure 2.5 depicts the energy leakage probability for the different pellet radii. These results indicate that Coulomb scattering, including large angle contribution and collective effects [82], and nuclear scattering have significant contributions to energy deposition in the plasma.

The increase in the fraction of charged particle energy deposited to the ions leads to higher fusion gains [11] as energy deposited to the electrons lead to radiation losses from the plasma. Increase in plasma temperature results in an increase in nuclear scattering leading to higher energy deposition to the ions. Also, the effect of large angle Coulomb scattering (which leads to energy deposition mainly to the ions) increases with increasing density. In figure 2.6 (a), the fraction of charged particle (deuteron) energy deposited to the ions in deuterium plasma as a function of plasma temperature and number density is shown. In figure 2.6 (b), the thermalization distance of a 3.5 MeV deuteron in deuterium plasma as a function of plasma density and temperature is plotted. Deuteron deposits more energy in a denser and colder plasma showing a reduction in the thermalization distance.

Next, we consider a DT plasma with equal amounts of D and T. The alpha particles produced in the reaction redeposit their energy into the burning regions of the pellet and leads to bootstrap heating. The range of a 3.5MeV alpha particle as a function of the plasma temperature for various plasma densities are shown in figure 2.7. Though the thermalization distance decreases with increasing density for a particular temperature, the range which is the product of density and thermalization distance, is found to increase with density. In figure 2.8, we plot the plasma temperature as a function of fraction of alpha particle energy deposited to the ions for various plasma densities. As the electron temperature increases, an increasingly large fraction of alpha energy is deposited into the ions. This fraction also increases for higher plasma densities.

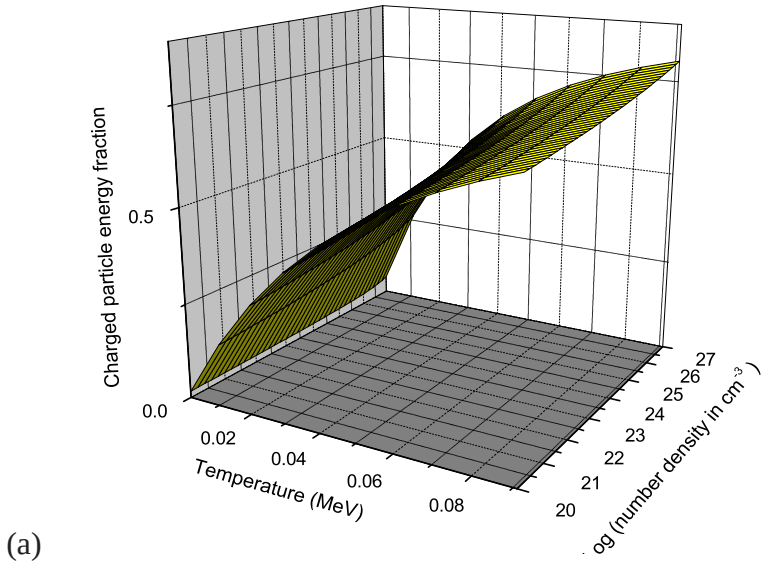

(a)

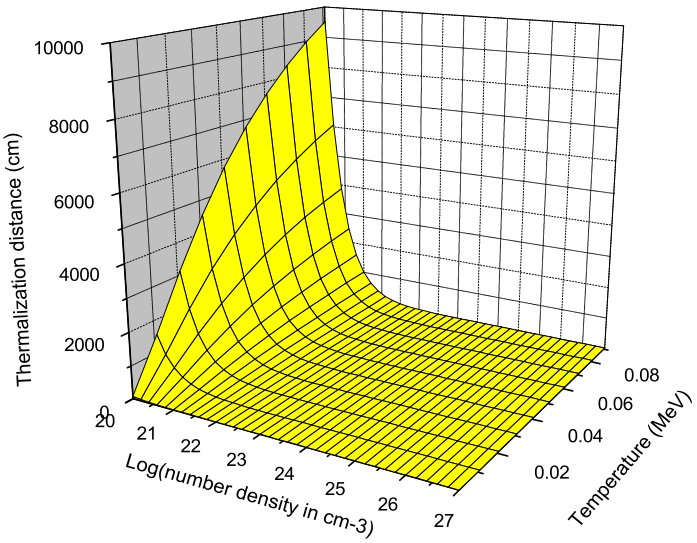

(b)

Figure 2.6: (a) Fraction of charged particle (deuteron) energy deposited to the ions in deuterium plasma as a function of plasma temperature and logarithm of the number density. (b) Thermalization distance of a 3.5 MeV deuteron in deuterium plasma as a function of plasma temperature and logarithm of the number density.

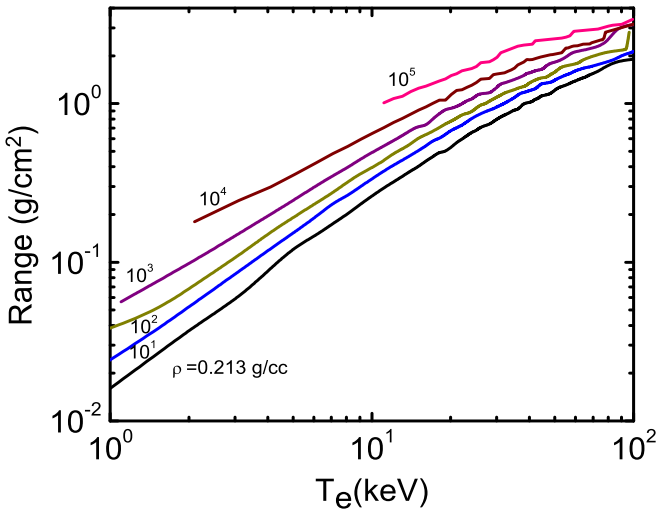

Figure 2.7: Range of alpha particles Vs. electron temperature for various densities.

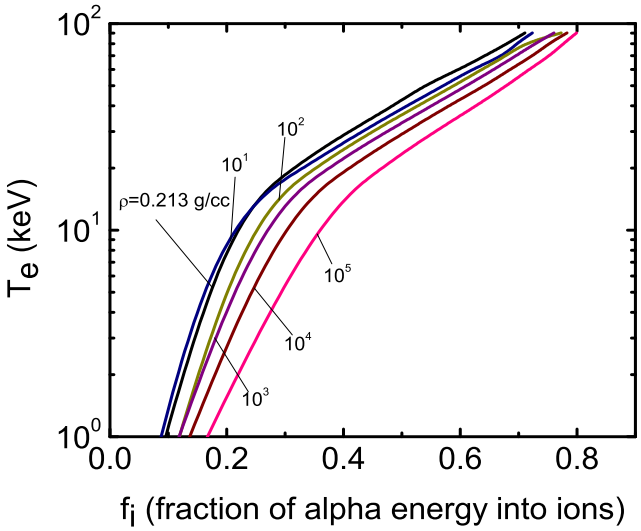

Figure 2.8: Plasma temperature Vs. fraction of alpha energy deposited to ions for various plasma densities.

2.4 Summary

We have incorporated the effects of large angle Coulomb scattering, plasma collective interaction and nuclear scattering to obtain the energy leakage probability from a pellet of size comparable to the thermalization distance. It is found that the energy leakage probability decreases significantly compared to the case when energy deposition to ions due to small angle Coulomb scattering alone is taken into account. A simple multigroup model is developed for correctly accounting the energy deposition by neutrons into the plasma. We also generate extensive results for thermalization distance of deuteron in a deuterium plasma at a range of densities and temperatures and compare with those obtained by considering loss to ions and electrons only. Variation in the range and fraction of alpha particle energy deposited to ions in a DT plasma is also studied for various plasma densities and temperatures.

3 Internal tritium breeding and thermonuclear burn characteristics of compressed D-T microspheres using zero-dimensional model

3.1 Introduction

The ignition temperature of a thermonuclear fusion reaction is found to decrease on adding a small amount of tritium (x$\sim$ 0.0112) to deuterium fusion pellet (DT_x). For lower fuel temperatures ($\sim$10 keV), the D-T reaction proceeds at a rate almost two orders of magnitude larger than that characterizing the D-D reaction [3, 9]. Hence, in order to minimize the ignition temperature, tritium is added to deuterium fusion pellets in stoichiometric ratio (50:50). However tritium inventories in futuristic fusion reactors based on current stoichiometric DT proposals are very high, which poses a significant radiological problem [2]. Also, the breeding of tritium in external tritium blanket and its separation is quite complicated. The concept of internal tritium breeding in which a small amount of tritium in deuterium fusion pellet reduces the ignition temperature and also acts as a catalyst is very lucrative [3]. The conditions necessary for realizing tritium breeding crucially depend on the energy deposition and loss rates from the

plasma. Radiation losses due to inverse Compton scattering and photon losses have been shown to affect the tritium breeding in a major way [57]. Therefore we re-evaluate this problem using a zero-dimensional model with the improvement in charged particle and neutron energy deposition mechanisms discussed in the earlier chapter. In this chapter, we also analyze the catalytic regime for tritium by changing the fraction of tritium (x). The initial density and temperature of the pellet are also found to influence the ignition conditions in a major way. A density-temperature regime is found where internal tritium breeding occurs even on including all the radiative loss mechanisms like bremsstrahlung and inverse Compton scattering. We obtain the optimum pellet parameters for which the deuterium burn fraction is high in addition to tritium in the pellet behaving as a catalyst. The fusion yields of ICF pellets having equal amounts of D and T (50:50) are obtained using the zero-dimensional model. Fusion yields in case of volume, and central ignition have been considered. For volume ignition, yields have been obtained for DT pellets of different masses and densities having a range of initial temperatures and are found to vary as $\rho^{2/3}$ for spheres of fixed mass m. For central ignition, the code has been modified to include the burn propagation into the outer cold fuel, bootstrap heating and subsequent increase in fusion reactions. Comparison with the results of a one-dimensional 3T Lagrangian hydrodynamics code shows good agreement which supports the fact that though the zero dimensional model lacks spatial resolution, tracking the number densities and energetics of the nuclides is sufficient for obtaining the energy released in fusion.

3.2 Simulation model

A time dependent calculation of the fusion process of a $\mathrm{DT_x}$ pellet can be performed using a simple zero-dimensional model in which the spatial variation is ignored. The energy produced in a fusion reaction is carried by the products in a ratio inversely proportional to their masses. The energetic fusion products then deposit this energy to the ions and electrons of the back-

ground plasma via Coulomb scattering. The neutrons deposit less energy in the medium as they have a larger mean free path. The rate equations of the nuclides present in the highly compressed and heated thermonuclear plasma are solved along with the energy balance equations for ions, electrons and radiation [58]. At this high densities and temperatures, photons interact with the medium via Bremsstrahlung and inverse Compton scattering. As we are considering a fully ionised plasma in this model, the effect of bound-bound and bound-free transition is neglected. Most of the phenomena important in normal gases disappear; electron attachment, dissociative recombination, excitation and deexcitation of atoms and molecules, electrical breakdown, etc. do not occur in a fully ionized plasma. Also, the encounters between the charged particles become simpler, as inverse square forces are more precisely calculable than the complicated interactions of systems containing bound electrons [59]. The radius of the pellet is assumed to expand with sound speed times the burn fraction so that the initial stagnation phase is accounted for and fusion occurs until the pellet disassembles. In this model, the delay time in the energy deposition by fusion-born particles is not accounted. Also, the mechanism of suprathermal fusions induced by high energy ions is neglected. By neglecting the finite time needed to slow-down the fusion products, the energy evolution speed is overestimated, whereas, by neglecting the suprathermal fusions, the actual fusion power is underestimated. However, the energy equations governing the plasma evolution are still first order accurate. Two-dimensional space-time dependent codes embodying simulation of all the mechanisms will be needed for an accurate design of the targets, but target physics and its features are well described by the present model. The neutron and proton channels of the DD reaction occur with 50% probability. The total number of particles, N_k, of species k, is governed by the equation

$$\frac{dN_k}{dt} = \sum_j {a_k}^j N_{j(1)} N_{j(2)} < \sigma v >_j \frac{1}{V}, \tag{3.1}$$

where V is the volume of the heated plasma, $< \sigma v >_j$ is the Maxwell averaged reaction rate of reaction j and ${a_k}^j$ is the number of particles of species k created or destroyed in the reaction j. Eliezer. *et al* used $< \sigma v >_j$ values at different temperatures from [89]. The four major reactions, given by eqns. [1.1]-[1.4] and six species viz. $\mathrm{D}_1^2, \mathrm{He}_2^3, \mathrm{T}_1^3, \mathrm{H}_1^1, \mathrm{He}_2^4 \text{ and } \mathrm{n}_0^1$ are considered in the calculation. The equation of energy balance for ions is given by

$$\frac{3}{2}\frac{d}{dt}(N_{ion}T_{ion}) = \sum_j \sum_k {f_k}^j {\omega_k}^j E_j N_{j(1)} N_{j(2)} \times < \sigma v >_j \frac{1}{V} - \frac{P_{ie}}{V} - N_{ion}T_{ion}4\pi R^2(t)c_s\frac{1}{V} \quad (3.2)$$

where T_{ion} is the ion temperature, E_j is the energy yield of reaction j, ${\omega_k}^j$ is the fraction of E_j carried by the product k, ${f_k}^j$ is the fraction of the energy of the product k created in the reaction j that is deposited into the plasma ions, P_{ie} is the ion electron energy exchange term, $R(t)$ is the pellet radius, c_s is the sound speed and N_{ion} is the total number of ions,

$$N_{ion} = \sum_k N_k, \quad (3.3)$$

where k varies from 1 to 5 as $k = 6$ stands for neutrons.

The equation for energy balance for electrons is given by

$$\frac{3}{2}\frac{d}{dt}(N_{elec}T_{elec}) = \sum_j \sum_k (1 - {f_k}^j){\omega_k}^j E_j N_{j(1)} N_{j(2)} \times < \sigma v >_j \frac{1}{V} + \frac{P_{ie}}{V} - \frac{P_B}{V} - P_C - N_{elec}T_{elec}4\pi R^2(t)c_s\frac{1}{V}, \quad (3.4)$$

where N_{elec} is the number of electrons, T_{elec} is the electron temperature, P_B is the Bremsstrahlung term and P_C is the inverse Compton scattering term. The ion-electron energy exchange term is given by

$$P_{ie}(\mathrm{keVcm^3/s}) = 1.69 \times 10^{-13} N_{elec} \sum_k \ln \Lambda_{ek} {Z_k}^2 \frac{N_k}{m_k} \times \frac{T_{ion}(keV) - T_{elec}(keV)}{T_{elec}(keV)^{1.5}}, \quad (3.5)$$

where m_k and Z_k are the mass number and the charge of nuclei k, respectively. The Coulomb logarithm for ion-electron collision is [90]

$$\ln \Lambda_{ek} = 23 - \ln[(\frac{N_{elec}}{V})^{0.5} Z_k T_{elec}(eV)^{-1.5}]. \tag{3.6}$$

The Bremsstrahlung loss term including the inverse bremsstrahlung term incorporated in [57] is given by

$$P_B(\mathrm{keVcm^3/s}) = 2.94 \times 10^{-15} N_{elec} \times \sum_k N_k {Z_k}^2 \times T_{elec}(keV)^{0.5} \times G(\gamma) \frac{T_{elec} - T_r}{T_{elec}}, \tag{3.7}$$

with

$$G(\gamma) = \frac{\pi^2}{4} \frac{(T_r + 1.03 \times T_{elec})}{(T_r + 2.54 \times T_{elec})}. \tag{3.8}$$

However, the Bremsstrahlung loss term decreases in the case of degenerate plasmas [91] [92]. Also the inverse Compton scattering term is

$$P_C(\mathrm{keV/s}) = 1.67 \times 10^{20} \times \frac{32}{3} \pi {r_e}^2 c {T_r}^4 N_{elec}(T_{elec} - T_r), \tag{3.9}$$

where $r_e = 2.81794 \times 10^{-13}$ cm is the classical electron radius. In the mechanical expansion term, the speed of sound is computed using $c_s = \sqrt{\frac{\gamma P}{\rho}}$ where ρ is the density, $\gamma = 5/3$ and P is the total pressure, $P = \frac{1}{V}(N_{ion} T_{ion} + N_{elec} T_{elec})$ The radius of the pellet is governed by

$$R(t) = R(t - \Delta t) + \eta c_s \Delta t, \tag{3.10}$$

where $\eta = 2 \times \phi(t)$ for $\phi(t) < 0.5$ and $\eta = 1$ for $\phi(t) \geq 0.5$

with the burn fraction $\phi(t) = 1 - N_D(t)/N_D(0)$.

It is assumed that the ratio of Coulomb logarithms for ions to electrons is approximately

equal to 1.2 for each ion at all temperatures and densities. Further elastic nuclear scattering is neglected and the term involving error function in $(\frac{dE}{dx})_i$ is approximated as unity. Thus Eliezer *et al* [58] use the formula

$$f_k{}^j = \frac{1}{\omega_k{}^j E_j} \int_{T_{ion}}^{\omega_k{}^j E_j} dW \left[1 + \frac{1.6}{\sqrt{\pi}} (\frac{W}{T_{elec}})^{3/2} \times (\frac{m_{elec}}{m_k})^{1/2} \frac{N_{elec}}{m_k \sum_i N_i \frac{{Z_i}^2}{m_i}} \right]^{-1} \tag{3.11}$$

for the fraction of energy deposited to ions. We note that the correct numerical factor in the above equation is 1.11 instead of 1.6 used by them. For a fully ionized single component plasma, like deuterium, this fraction is independent of plasma density. The fraction of neutron energy deposited in the plasma, as used by Eliezer *et al* [58], is $\rho R/(\rho R + 13.72)$ and $\rho R/(\rho R + 3.92)$ for 14 MeV and 2.45 MeV neutrons, respectively [93]. With the detailed model described in 2.2.1, the fraction $f_k{}^j$ is obtained as

$$f_k{}^j = \frac{1}{\omega_k{}^j E_j - T_{ion}} \times \int_{T_{ion}}^{\omega_k{}^j E_j} dW \frac{A_d(W) + A_N(W) W^2}{A_d(W) + A_e(W) + A_N(W) W^2}. \tag{3.12}$$

Further, we use the neutron energy deposition model of 2.18 given in 2.2.2, and the more accurate fits for the Maxwell averaged reaction rates [94].

We have used Hurwitz's three temperature model [57] for the rate equation for the radiation temperature:

$$4\sigma_B T_r^3 \frac{dT_r}{dt} = \frac{P_B}{V} + P_C - R_{loss}, \tag{3.13}$$

where the photon energy loss rate in keV/s is

$$R_{loss} = 1.8069 \times 10^{28} \times \frac{3\,\sigma_B}{R} {T_r}^4 V, \tag{3.14}$$

where $\sigma_B = 5.67 \times 10^{-8}\,\mathrm{Wm^{-2}K^{-4}}$ is Stefan-Boltzmann's constant. The rate equations for

number of ions and electrons and the energy balance equations for ions, electrons and radiation have been solved using the adaptive Cash Carp Runge Kutta method as described in appendix A.

3.3 Internal tritium breeding

For analyzing the problem of internal T breeding in DT_x pellets, we consider an optimal pellet configuration of density $\rho = 5000\ \mathrm{gm/cm^3},\ \rho\mathrm{R} = 12.5\ \mathrm{gm/cm^2}$ where R is the pellet radius, tritium fraction x= 0.0112, and ion, electron, and radiation temperatures given by $\mathrm{T_{ion}} = \mathrm{T_{elec}} = 10$ keV and $\mathrm{T_r} = 1\ \mathrm{keV}$, respectively, analyzed by Eliezer *et al*. While this pellet showed tritium breeding within the assumptions made by Eliezer *et al*, using the Maxwell averaged reaction rates versus temperature as obtained by Feldbacher [89], it failed to show breeding when inverse Compton scattering and photon losses were taken into account. However with the improved energy deposition model by charged particles and neutrons and using the improved formulas for fusion reaction rates [94] it is found that the pellet breeds tritium even under extreme conditions of radiation loss.

Figure 3.1 shows the variation in the fraction of a) charged particle energy deposited to the ions as a function of time for the model used by Eliezer *et al* and the detailed model discussed in this chapter as given by equations 3.11 and 3.12, respectively, and b) neutron energy deposited to the ions. In figure 3.2, we compare the ion temperatures as the pellet burns. The ions reach much higher temperatures which results in larger fraction of energy being deposited to the ions when the above discussed energy deposition model is used. In figure 3.3, we show the time dependent tritium build up in the target. Figure 3.4 compares the time dependent fusion power for the approximate and detailed models, respectively, and the total energy produced are $2.905 \times 10^{23}\ \mathrm{keV/cm^3}$ and $3.212 \times 10^{23}\ \mathrm{keV/cm^3}$ for the two cases. Similarly, tables 3.1 and 3.2 summarize the various results obtained with different radiation loss mechanisms for the two

	no radiation interaction	direct and inverse bremsstrahlung	direct and inverse Compton	reduced photon losses
Maximum temperatures in keV				
T_{ion}	310.90	318.20	146.90	115.20
T_{elec}	197.70	201.70	73.90	64.22
T_r	-	16.90	26.16	64.22
Burn fraction	0.45	0.45	0.40	0.38
Ratio of tritium content				
Initial	1.00	1.00	1.00	1.00
Minimum	0.56	0.60	0.59	0.59
Maximum	2.91	3.02	1.42	1.05
Final	2.33	2.38	0.79	0.64

Table 3.1: Maximum ion, electron and radiation temperatures (in keV) along with the burn fraction and tritium breeding ratio in the DT pellet for the model used by Eliezer *et al*. Column 1 refers to only bremsstrahlung loss in the two temperature model, Column 2 includes inverse bremsstrahlung as well in the three temperature model, Column 3 includes, in addition, inverse Compton scattering and Column 4 is similar to Column 3, but without photon losses.

different energy deposition models.

Using the above described zero dimensional three temperature model which considers all the energy deposition mechanisms like small and large angle Coulomb scattering, nuclear scattering and collective plasma effects, the effect of varying various pellet parameters like its density, fraction of tritium added and initial temperature on the burn fraction and tritium breeding ratio is studied.

3.3.1 Effect of pellet density on tritium breeding ratio and deuterium burn fraction

The initial density of the DT pellet determines the burn fraction of deuterium and also the breeding ratio of tritium. For the purpose of simulation we consider a pellet of radius 25 μm, initial ion and electron temperature 10 keV, initial radiation temperature 1 keV and tritium fraction x = 0.0112. If the initial pellet density is less than 4000 gm/cc, tritium breeding is not

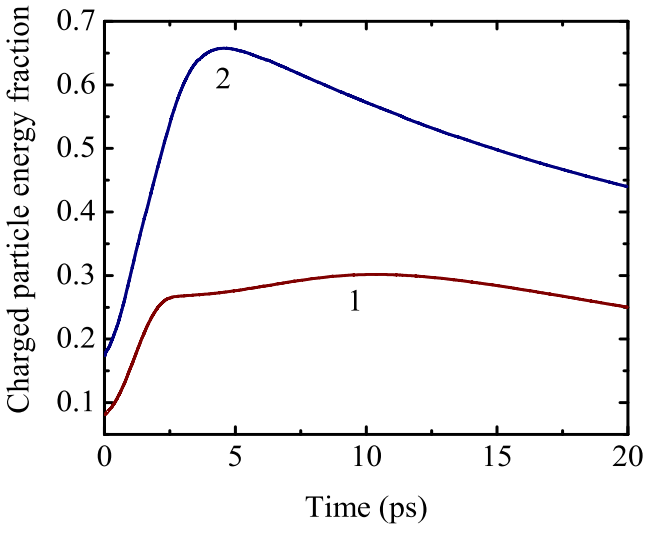

a)

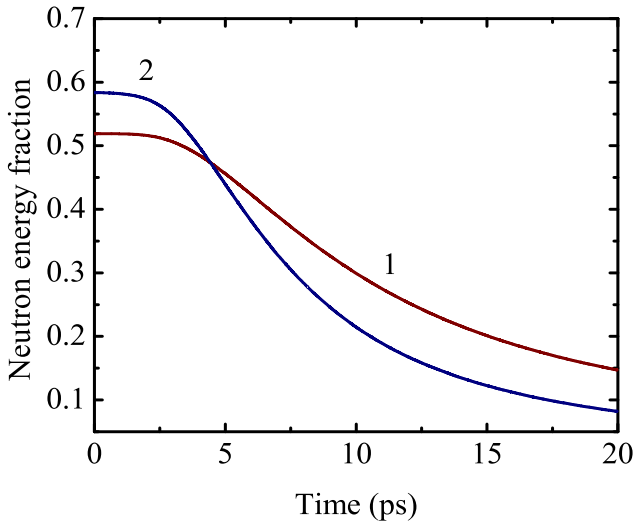

b)

Figure 3.1: Fraction of a) charged particle energy deposited to the ions as the pellet burns. Curve-1 shows the case when energy deposition to ions and electrons due to small angle Coulomb scattering alone is considered. Curve-2 considers energy deposition via large angle Coulomb scattering, collective effects and nuclear interactions using the improved Maxwell averaged reaction rates . b) neutron energy deposited to the ions as the pellet burns. Curve-1 is obtained using the fitted formula and Curve-2 is that for the model discussed in this chapter using the improved Maxwell averaged reaction rates.

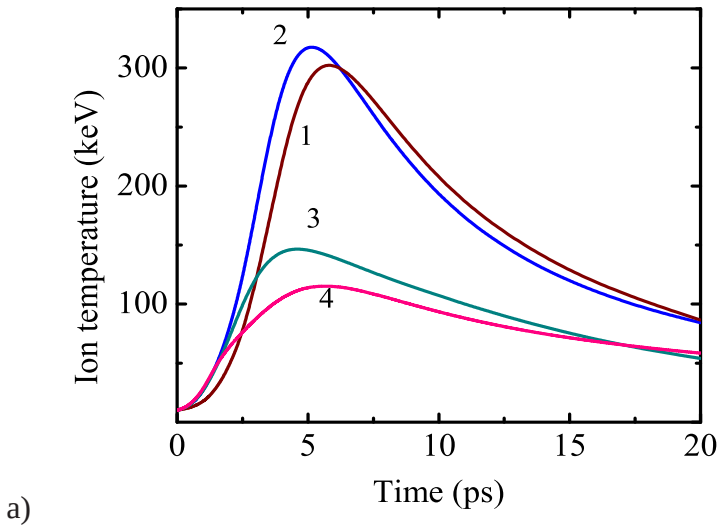

a)

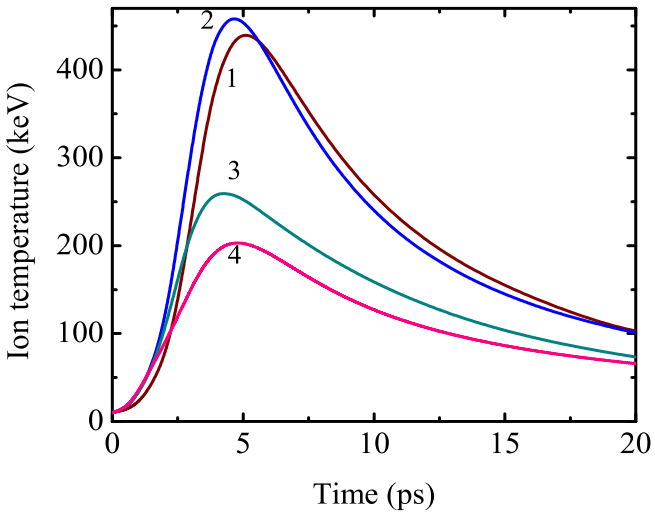

b)

Figure 3.2: Ion temperatures Vs. time in the DT pellet for a) the model used by Eliezer *et al* and b) the model described in this chapter. Curve-1 refers to bremsstrahlung loss only, Curve-2 includes inverse bremsstrahlung as well, Curve-3 includes, in addition, inverse Compton scattering and Curve-4 is similar to Curve-3, but without photon losses.

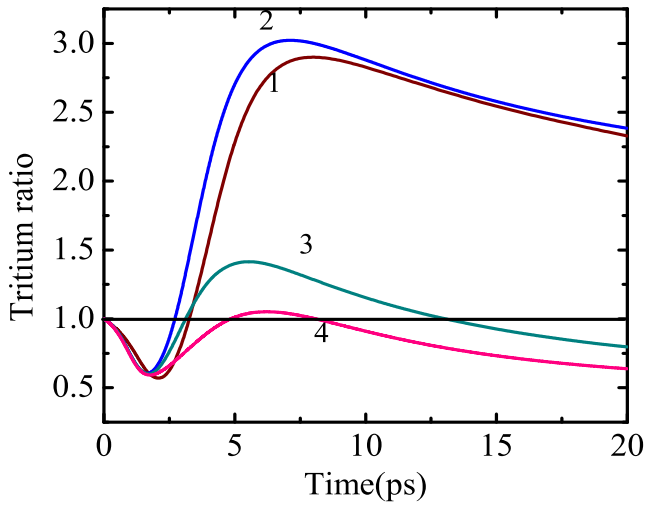

a)

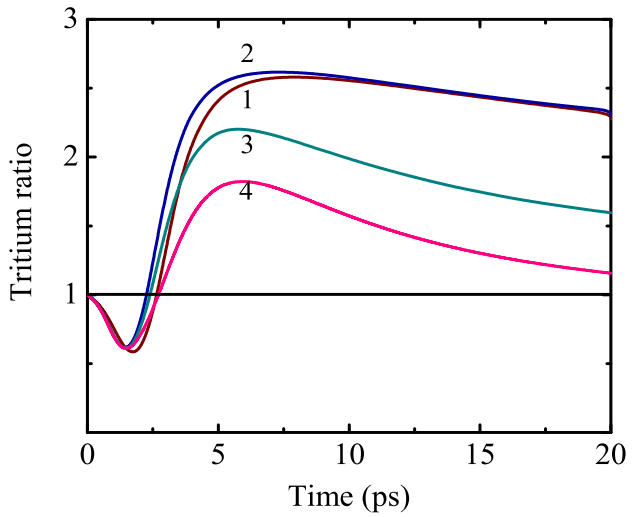

b)

Figure 3.3: Tritium breeding Vs. time for the DT pellet for a) the model used by Eliezer *et al* and b) the model described in this chapter. Curve-1 refers to bremsstrahlung loss only, Curve-2 includes inverse bremsstrahlung as well, Curve-3 includes, in addition, inverse Compton scattering and Curve-4 is similar to curve-3, but without photon losses.

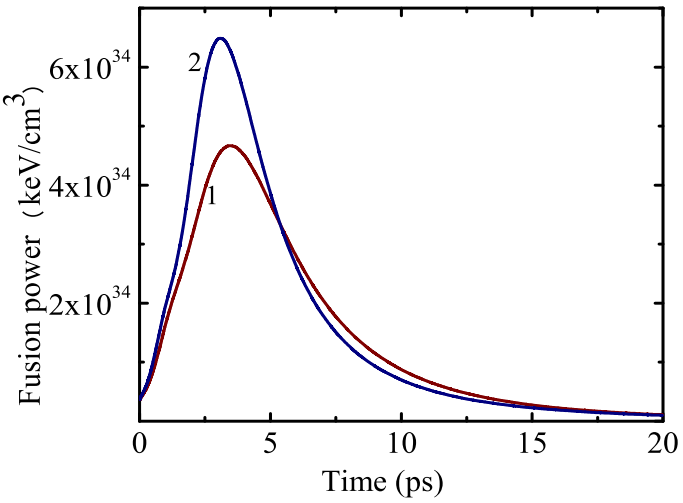

Figure 3.4: Fusion power generated Vs. time for the case of energy exchanged via bremsstrahlung, inverse bremsstrahlung and Compton scattering. Curve-1 is for the model used by Eliezer *et al* and Curve-2 for the model described in this chapter.

	no radiation interaction	direct and inverse bremsstrahlung	direct and inverse Compton	reduced photon losses
Maximum temperatures in keV				
T_{ion}	448.40	459.20	259.90	203.00
T_{elec}	176.50	179.50	84.31	65.67
T_r	-	16.76	27.41	65.69
Burn fraction	0.48	0.48	0.47	0.45
Ratio of tritium content				
Initial	1.00	1.00	1.00	1.00
Minimum	0.57	0.61	0.61	0.61
Maximum	2.59	2.62	2.20	1.82
Final	2.33	2.34	1.59	1.16

Table 3.2: The various fuel burnup parameters for the improved energy deposition model discussed in this chapter.

possible i.e., the amount of tritium left in the pellet after the burn is less than the amount we started with [figure 3.5(a)]. However, above a density of 4000 gm/cc, tritium acts as a catalyst and results in more efficient deuterium burning [figure 3.5(b)]. The deuterium burn fraction is defined as $f_b = (N_{D,initial} - N_{D,final})/N_{D,initial}$, where $N_{D,initial}$ is the total number of deuterons in the pellet initially and $N_{D,final}$ is the number left in the pellet after the burn. The burn fraction steeply decreases with decreasing density as depicted in figure 3.5(b).

3.3.2 Effect of initial temperature of ions and electrons

Below a certain initial temperature of the pellet (both ions and electrons are assumed to be at the same temperature initially), the losses exceed the energy production and the pellet does not burn. The rate of fusion reactions decrease on decreasing the initial plasma temperature within the pellet and this leads to slow burnup and reduced production of tritium [figure 3.6(a)]. A pellet of radius 25 μm, density 5000 gm/cc, initial radiation temperature 1 keV and tritium fraction x = 0.0112 is considered. Below 4 keV, the reactions become so slow that within the pellet disassembly time the rate of fusion reactions remains negligibly small. As a result the deuterium burn fraction is also found to decrease steeply on reducing the initial temperature below 6 keV [figure 3.6(b)].

3.3.3 Effect of tritium fraction (x) in the pellet

For a pellet of radius 25 μm, density 5000 gm/cc, initial ion and electron temperature 10 keV and initial radiation temperature 1 keV, as the fraction of tritium (x) in the pellet is decreased below 0.005, it is no more able to ignite the deuterium so that the burn becomes slower. Also the deuterium burn fraction keeps on decreasing as the tritium content is decreased. However, it is also observed that increasing the tritium fraction beyond 0.03 does not increase the burn fraction any further and the initial amount of tritium in the pellet is also not replenished [figure 3.7(a) and (b)]. Finally, from the above studies on the various pellet parameters like its density,

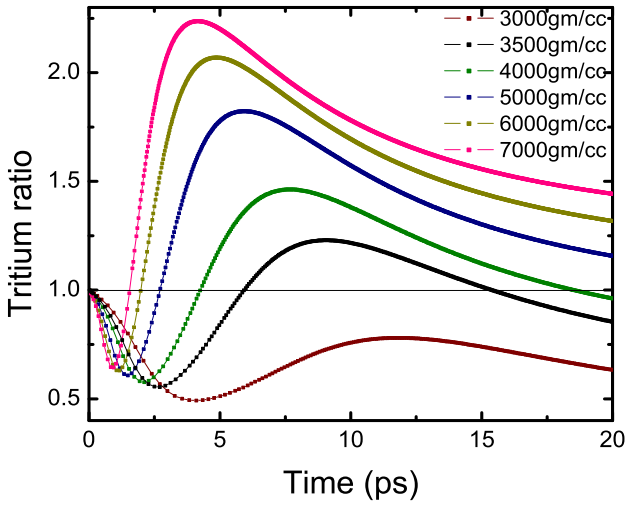

(a)

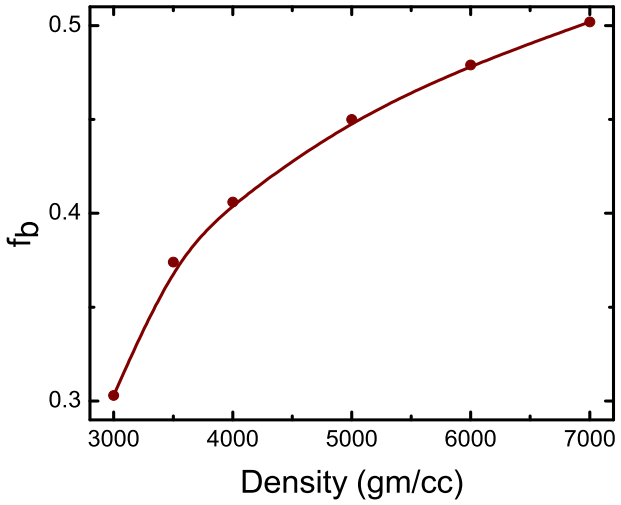

(b)

Figure 3.5: (a) Tritium breeding ratio versus time for DT_x pellets having different initial pellet densities. (b) Deuterium burn fraction as a function of the pellet density.

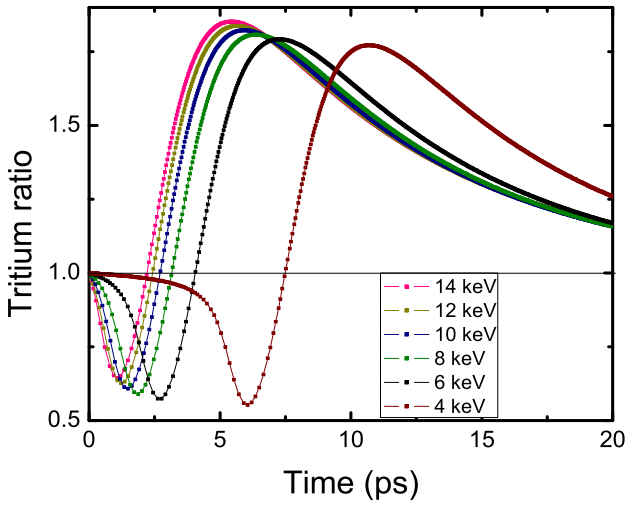

(a)

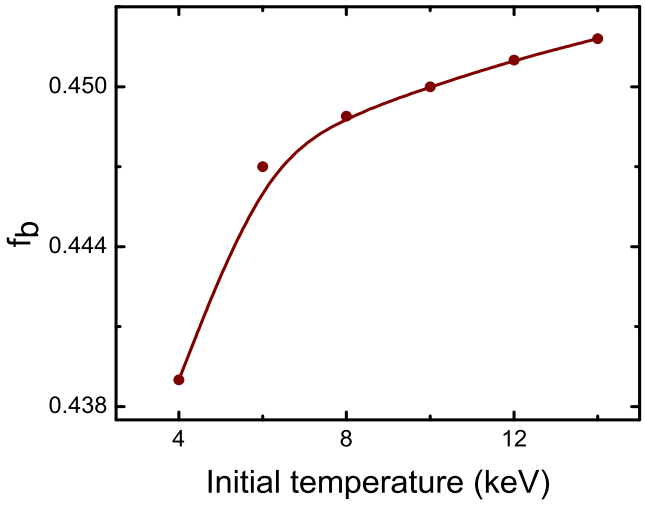

(b)

Figure 3.6: (a) Tritium breeding ratio versus time for DT_x pellets having different initial plasma temperatures. (b) Deuterium burn fraction as a function of the initial plasma temperatures.

initial temperature and fraction of tritium added, we conclude that for sufficient burning of the pellet and for tritium to behave as a catalyst, the following pellet configuration is necessary: initial pellet density = 3500gm/cc, initial plasma temperature = 4 keV and fraction of tritium added lies between 0.005 and 0.02 i.e., $0.005 \leq x \leq 0.02$

3.4 Zero dimensional model for central ignition

The gain of a DT pellet can be improved by heating only the central region to ignition temperature, under conditions that the spherical thermonuclear burn wave then propagates out, igniting the rest of the fuel. To obtain the fusion yields in centrally ignited pellets, using the zero dimensional model, modifications to the rate and energy equations are required.

In central ignition only a central portion of the pellet of radius R_i is heated to very high temperatures whereas the outer region is cold. Let R_o be the outer radius of the pellet. Thermonuclear reaction starts in the inner pellet and the radius starts expanding. Two separate regions can be distinguished: first the inner radius expands through the outer cold DT fuel till it reaches the outer radius, second the burn front has propagated to the outer radius and now the whole pellet expands freely. The second region is the same as that for volume ignition, whereas in the first region, the inner radius expands against an external pressure due to the cold outer region. The thermonuclear burn front propagates via the detonation and the high temperature thermal conductivity, so that the velocity of the burn front is the maximum of two velocities, $u_{max} = \max(u_s, u_T)$ where u_s is the velocity of the detonation wave, while u_T is the velocity of the thermal wave. The approximate analytical expressions for these velocities are obtained by applying the strong explosion approximation in a homogeneous gas mixture [95]. If R is the radius of the expanding burn front, for $R \leq R_0$, the detonation wave velocity is

$$u_s = \sqrt{\frac{(\gamma+1)^2(\gamma-1)C_V}{3\gamma-1}}\sqrt{T}, \tag{3.15}$$

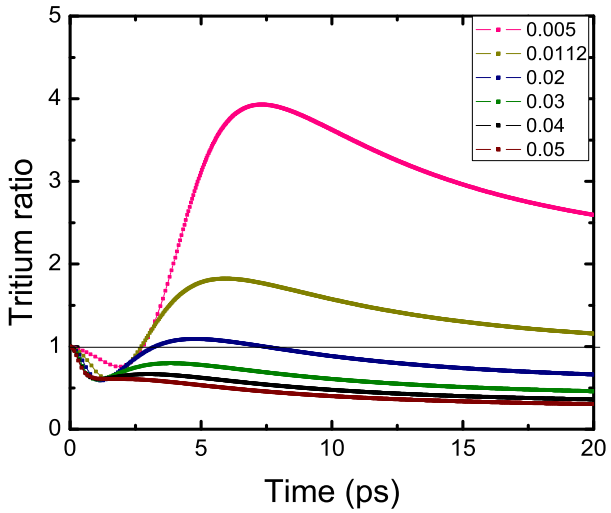

(a)

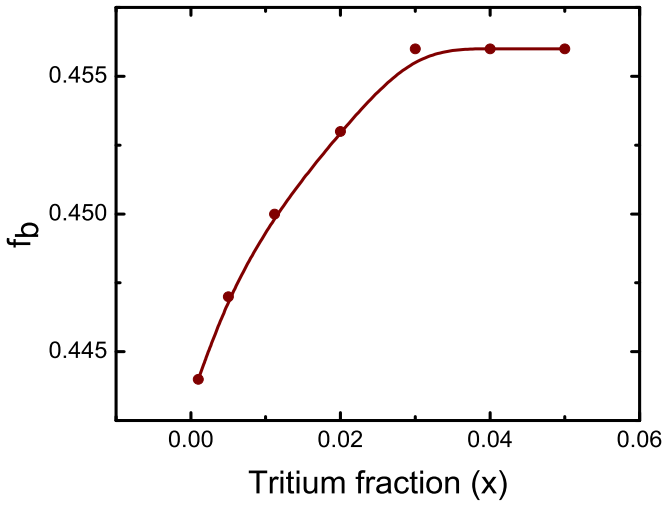

(b)

Figure 3.7: (a) Tritium breeding ratio versus time for DT_x pellets having different initial tritium fraction (x). (b) Deuterium burn fraction as a function of the initial tritium fraction (x).

where $C_V = \frac{3}{2}\frac{k_B}{\overline{A}m_A}\frac{T_{ion}+\overline{Z}T_{elec}}{T}$ is the specific heat at constant volume, γ is the specific heat ratio and $T = T_{elec} = T_{ion}$ is the temperature behind the burn front. Also the thermal wave velocity is [96]

$$u_T(x_b, T) = \frac{2.149 \times 10^{-4}\overline{A}}{(1+\overline{Z})(1+0.291\overline{Z})ln\Lambda_{ie}}\frac{T^{2.5}}{x_b}, \tag{3.16}$$

where $x_b = \rho R$ is the burn-up parameter and $\ln \Lambda_{ie}$ is the Coulomb logarithm defined in eqn. 3.6. For equimolar DT (50:50), average mass number $\overline{A} = 2.5$, average atomic number $\overline{Z} = 1$ and $C_V = 115.678\ MJ/g$. Hence the detonation and thermal velocities are $D = 3.7 \times 10^7\sqrt{T}$ and $u_T(x_b, T) = 2.08 \times 10^5\frac{T^{2.5}}{x_b \ln \Lambda_{ie}}$ both in cm/s. The maximum of the two velocities $u_{max} = \max\{u_s, u_T\}$ is chosen for our calculations. The thermonuclear burn wave propagates initially as the thermal wave and later as the detonation wave.

As long as the inner radius has not reached the outer radius of the pellet, the outer cold fuel is assumed to remain undisturbed, i.e., the outer radius does not change and the densities and temperatures are maintained at the initial values. The equation for energy balance for ions is now modified to

$$\begin{aligned}\frac{3}{2}\frac{d}{dt}(N_{ion}T_{ion}) = &\sum_j \sum_k {f_k}^j {\omega_k}^j E_j N_{j(1)} N_{j(2)} \times < \sigma v >_j \frac{1}{V} \\ &-\frac{P_{ie}}{V} - 4\pi R^2(t) u_{max}\left(\frac{N_{ion}T_{ion}}{V} - \frac{N_{io}T_{io}}{V_o}\right),\end{aligned} \tag{3.17}$$

where N_{io}, T_{io} and V_o are the total number of ions, ion temperature and volume of the outer pellet. N_{ion} is the total number of ions in the burn region and increases until the inner pellet radius becomes equal to the outer radius. Similarly, the equation for energy balance for electrons

is given by

$$\frac{3}{2}\frac{d}{dt}(N_{elec}T_{elec}) = \sum_j \sum_k (1 - {f_k}^j){\omega_k}^j E_j N_{j(1)} N_{j(2)}$$
$$\times < \sigma v >_j \frac{1}{V} + \frac{P_{ie}}{V} - \frac{P_B}{V} - P_C - 4\pi R^2(t) u_{max} \left(\frac{N_{elec}T_{elec}}{V} - \frac{N_{eo}T_{eo}}{V_o} \right), \quad (3.18)$$

where N_{eo}, T_{eo} and V_o are the total number of electrons and electron temperature in the outer pellet. The total number of particles of D and T change not only because of the fusion reactions but also because of the addition of nuclides from cold outer fuel. During a time step Δt, let the inner radius R_i expand by ΔR. Since the outer region contains only D and T (ratio 50:50), for k=1 and 3,

$$N_k^n = N_k^{n-1} + \frac{3R^2\Delta R}{R_o^3} N_{k,total}, \quad (3.19)$$

where $N_{k,total}$ is the total number of nuclides of species k within the whole pellet. The superscripts n and n-1 denote the present and previous time step values respectively. Similarly, for the electrons,

$$N_{elec}^n = N_{elec}^{n-1} + \frac{3R^2\Delta R}{R_o^3} N_{e,total}, \quad (3.20)$$

where $N_{e,total}$ is the total number of electrons within the whole pellet initially. Again, for energy conservation to hold, a portion of energy from the inner heated region bootstrap heats the region of volume $4\pi R^2 \Delta R$. If M_k is the mass number of the k^{th} nuclide, then the final temperature is

$$T_{ion}^n = \frac{T_{ion}^{n-1}(\sum_{k=1,5} M_k N_k^{n-1}) + T_{io}(\sum_{k=1,5} \frac{3R^2\Delta R}{R_o^3} M_k N_{k,total})}{\sum_{k=1,5} M_k N_k^n}. \quad (3.21)$$

Similarly, the electron temperature is modified as

$$T_{elec}^n = \frac{T_{elec}^{n-1} N_{elec}^{n-1} + T_{eo}(\frac{3R^2\Delta R}{R_o^3} N_{e,total})}{N_{elec}^n}. \quad (3.22)$$

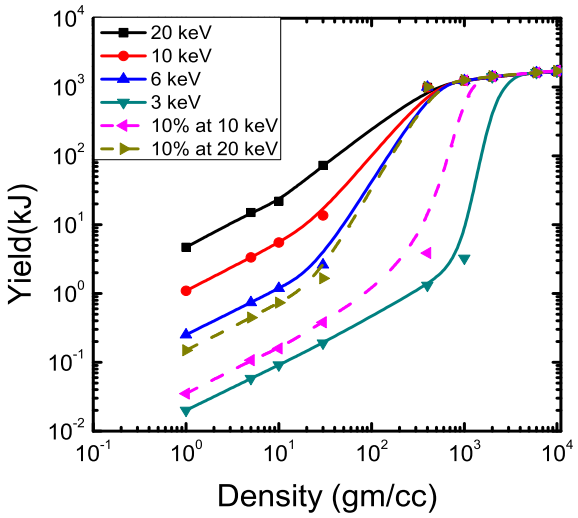

Figure 3.8: Yield Vs. density for 10 μg DT pellets having various initial temperatures.

In figure 3.8, the dashed lines show the fusion energy generated, i.e., the yields as a function of density for central 10 percent of the pellet at 10 and 20 keV, whereas the rest of the pellet at 1 keV.

The zero dimensional model is used to obtain the fusion yields for pellets having a range of densities and temperatures with 1 μg and 10 μg masses. Higher is the initial pellet temperature, more is the fusion yield because of the increase in DT and DD fusion reactions as a function of temperature. Also, as the initial pellet temperatures increase, the fusion yield attains saturation values for lower pellet densities. The results obtained are compared with the numerical results from a 3T Lagrangian simulation code and good agreement is obtained. This shows that though the zero dimensional model lacks spatial resolution, tracking the number densities and energetics of the nuclides is sufficient for obtaining the energy released in fusion. Figure 3.8 shows the fusion yields in kJ obtained for 10 μg DT pellet for a range of densities from 1 to 10,000 g/cc. Higher is the initial pellet temperature, more is the fusion yield because of the increase in DT and DD fusion reactions as a function of temperature. Also, as the initial pellet temperatures increase, the fusion yield attains saturation values for lower pellet densities. The

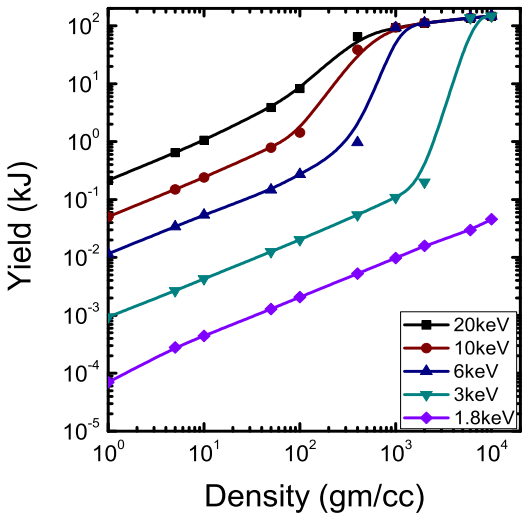

Figure 3.9: Yield Vs. density for 1 μg DT pellets having various initial temperatures.

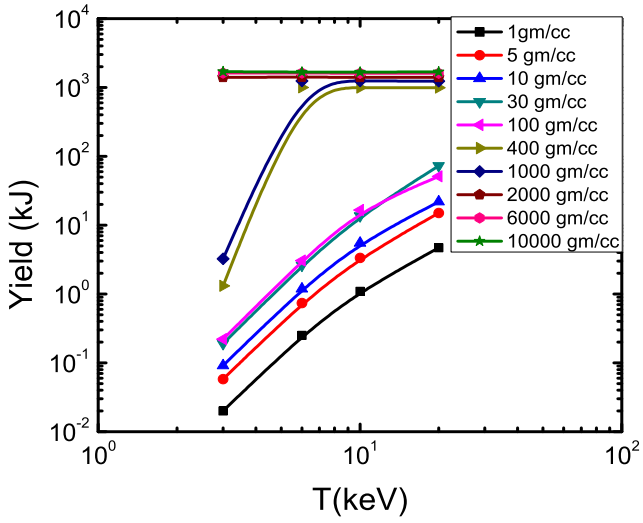

Figure 3.10: Yield Vs. temperature for 10 μg DT pellets having various initial densities.

values are also obtained for different initial temperatures of the pellet. Figure 3.9 shows the same values for a 1 μg pellet. For an initial pellet temperature of 1.8 keV, there is no steep rise in the fusion yield even for densities as high as 10,000 gm/cc showing the importance of ignition temperature in thermonuclear fusion. Details of the temperature dependence of the yield for various densities for the 10 μg pellet are shown in figure 3.10. Upto 100 gm/cc, the fusion yields are found to be low and rises slowly with temperature. Beyond this value the yields are found to increase sharply with the initial pellet temperatures and attain values of 1000 kJ. Beyond 1000 gm/cc, such high fusion yields are obtained even for low initial temperatures like 3 keV. This study quantitatively depicts the requirements of initial density and temperature for efficient thermonuclear burn in fusion pellets. Efficient high power lasers need to be developed to attain such high densities and temperatures.

3.5 Summary

In this chapter, the improved model of energy deposition via small and large angle Coulomb scattering, nuclear scattering and collective plasma effects has been used to re-evaluate a recent proposal for Tritium breeding in DT fusion pellets. Tritium breeding is found to occur even when all the radiative loss mechanisms like the Bremsstrahlung, and inverse Compton scattering effects are fully accounted for. This improved model of energy deposition has been used to obtain an optimum pellet configuration in terms of initial pellet temperature, density and tritium fraction. In this regime, tritium acts as a catalyst, helps in reducing the ignition temperature and the deuterium in the pellet burns sufficiently before the pellet disassembles. Modifications are made in the model to include central ignition of a DT pellet. Fusion yields for a range of initial densities and temperatures of the pellet are found to agree with those available in the literature.

4 Generating new analytical benchmarks for non-equilibrium radiation diffusion in finite size systems

4.1 Introduction

In the earlier chapters, a fully ionized plasma was considered so that the effect of bound-bound and bound-free transitions were neglected while considering the interaction of radiation with the medium [59]. Also, the radiation intensity was assumed to be spatially uniform [58]. For partially ionized plasmas with spatial variation, the radiation transport equation needs to be solved along with the material energy equation. Non-equilibrium radiation diffusion is an important mechanism of energy transport in Inertial Confinement Fusion, astrophysical plasmas, furnaces and heat exchangers. We devote this chapter to this important topic of radiation diffusion and derive new analytical solutions to the non-equilibrium Marshak diffusion problem in a finite planar slab, spherical shell and sphere. The variation in integrated energy densities and leakage currents are also studied. In order to linearize the radiation transport and material energy equation, the heat capacity is assumed to be proportional to the cube of the material temperature [63]. The steady state energy densities show linear variation along the depth of the planar slab, whereas non-linear dependence is observed for the spherical shell. Non-equilibrium diffusion codes can be more easily validated and verified against these new benchmark results because there is no need to consider a slab or spherical medium of very large size for avoiding

boundary effects. Analytical expressions for all the quantities of interest can be obtained for finite slab/shell width and parameter values relevant to practical problems.

4.2 Analytical solution

Using two independent methods, viz., the Laplace transform method and the Eigen function expansion method, expressions for radiation and material energy densities as a function of space and time is derived for a finite planar slab, spherical shell and sphere.

4.2.1 Planar slab

We consider a planar slab of finite thickness which is purely absorbing and homogeneous occupying $0 \leq z \leq l$. The medium is at zero temperature initially. At time t=0, a constant radiative flux (F_{inc}) is incident on the surface at z=0 as shown in figure 4.1. Neglecting hydrodynamic motion, the one group radiative transfer equation (RTE) in the diffusion approximation and the material energy balance equation (ME) are [6]

$$\frac{\partial E_r(z,t)}{\partial t} - \frac{\partial}{\partial z}[\frac{c}{3\sigma_a(T)}\frac{\partial E_r(z,t)}{\partial z}] = c\sigma_a(T)[aT^4(z,t) - E_r(z,t)], \tag{4.1}$$

$$C_V(T)\frac{\partial T(z,t)}{\partial t} = c\sigma_a(T)[E_r(z,t) - aT^4(z,t)], \tag{4.2}$$

where $E_r(z,t)$ is the radiation energy density, T(z,t) is the material temperature, $\sigma_a(T)$ is the opacity (absorption cross section), c is the speed of light, a is the radiation constant, and $C_V(T)$ is the specific heat of the material.

The Marshak boundary condition on the surface at $z = 0$ is given by

$$E_r(0,t) - \left(\frac{2}{3\sigma_a[T(0,t)]}\right)\frac{\partial E_r(0,t)}{\partial z} = \frac{4}{c}F_{inc}. \tag{4.3}$$

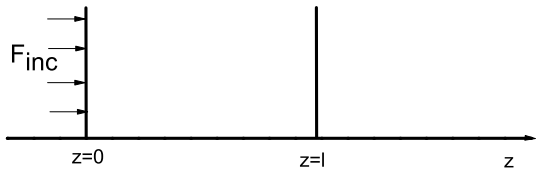

Figure 4.1: Flux incident on the left surface of a slab of thickness $z = l$

And that at $z = l$ is

$$E_r(l,t) + \left(\frac{2}{3\sigma_a[\mathrm{T}(l,t)]}\right)\frac{\partial E_r(l,t)}{\partial z} = 0. \tag{4.4}$$

The initial conditions on these two equations are

$$E_r(z,0) = T(z,0) = 0. \tag{4.5}$$

To remove the nonlinearity in the RTE (Eqn. [4.1]) and ME (Eqn. [4.2]), opacity σ_a is assumed to be independent of temperature and specific heat $C_V(T)$ is assumed to be proportional to the cube of the temperature. i.e., $C_V(T) = \alpha T^3$. The RTE and the ME are recast into the dimensionless form by introducing the dimensionless independent variables given by

$$x \equiv \sqrt{3}\sigma_a z, \tau \equiv (\frac{4ac\sigma_a}{\alpha})t. \tag{4.6}$$

The new dependent variables are given by

$$u_r(x,\tau) \equiv (\frac{c}{4})\left[\frac{E_r(z,t)}{F_{inc}}\right], u_m(x,\tau) \equiv (\frac{c}{4})\left[\frac{aT^4(z,t)}{F_{inc}}\right]. \tag{4.7}$$

With these new variables, the RTE and ME take the dimensionless form

$$\varepsilon \frac{\partial u_r(x,\tau)}{\partial \tau} = \frac{\partial^2 u_r(x,\tau)}{\partial x^2} + u_m(x,\tau) - u_r(x,\tau), \tag{4.8}$$

$$\frac{\partial u_m(x,\tau)}{\partial \tau} = u_r(x,\tau) - u_m(x,\tau), \tag{4.9}$$

with the initial conditions

$$u_r(x,0) = 0, \tag{4.10}$$

$$u_m(x,0) = 0. \tag{4.11}$$

And the boundary conditions on the surfaces are

$$u_r(0,\tau) - \frac{2}{\sqrt{3}} \frac{\partial u_r(0,\tau)}{\partial x} = 1, \tag{4.12}$$

$$u_r(b,\tau) + \frac{2}{\sqrt{3}} \frac{\partial u_r(b,\tau)}{\partial x} = 0, \tag{4.13}$$

where $b = \sqrt{3}\sigma_a l$ and the parameter ε is defined as

$$\varepsilon = \frac{4a}{\alpha}. \tag{4.14}$$

4.2.1.1 Laplace transform method

To solve Eqs. (4.8) - (4.13), we introduce the Laplace transform according to

$$\bar{f}(s) = \int_0^\infty d\tau e^{-s\tau} f(\tau), \tag{4.15}$$

to obtain

$$\varepsilon s \bar{u}_r(x,s) - \frac{\partial^2 \bar{u}_r(x,s)}{\partial x^2} = \bar{u}_m(x,s) - \bar{u}_r(x,s), \tag{4.16}$$

$$s\bar{u}_m(x,s) = \bar{u}_r(x,s) - \bar{u}_m(x,s), \tag{4.17}$$

$$\bar{u}_r(0,s) - \frac{2}{\sqrt{3}}\frac{\partial \bar{u}_r(0,s)}{\partial x} = \frac{1}{s}, \tag{4.18}$$

$$\bar{u}_r(b,s) + \frac{2}{\sqrt{3}}\frac{\partial \bar{u}_r(b,s)}{\partial x} = 0. \tag{4.19}$$

The solutions of Eqs. (4.16)-(4.19) in s space are obtained as

$$\bar{u}_r(x,s) = \frac{3\sin[\beta(s)(b-x)] + 2\sqrt{3}\beta(s)\cos[\beta(s)(b-x)]}{s[3\sin(\beta(s)b) + 4\sqrt{3}\beta(s)\cos(\beta(s)b) - 4\beta^2(s)\sin(\beta(s)b)]}, \tag{4.20}$$

$$\bar{u}_m(x,s) = \frac{3\sin[\beta(s)(b-x)] + 2\sqrt{3}\beta(s)\cos[\beta(s)(b-x)]}{s(s+1)[3\sin(\beta(s)b) + 4\sqrt{3}\beta(s)\cos(\beta(s)b) - 4\beta^2(s)\sin(\beta(s)b)]}. \tag{4.21}$$

where $\beta(s)$ is given by

$$\beta^2(s) = -\frac{s}{s+1}[1 + \varepsilon(s+1)]. \tag{4.22}$$

Before solving for the radiation and material energy densities by inverting $\bar{u}_r(x,s)$ and $\bar{u}_m(x,s)$, we first obtain the small and large τ limits of $u_r(x,\tau)$ and $u_m(x,\tau)$ from the large and small s limits of eqns. [4.20] and [4.21] respectively. Using the theorems

$$\lim_{s\to\infty}[s\bar{f}(s)] = \lim_{\tau\to 0}[f(\tau)], \tag{4.23}$$

$$\lim_{s\to 0}[s\bar{f}(s)] = \lim_{\tau\to\infty}[f(\tau)], \tag{4.24}$$

we have

$$u_r(x,0) = u_m(x,0) = 0, \tag{4.25}$$

$$u_r(x,\tau\to\infty) \to u_m(x,\tau\to\infty) \to \frac{3b + 2\sqrt{3} - 3x}{3b + 4\sqrt{3}}. \tag{4.26}$$

Thus according to eqn. [4.25], at the initial instant, both the material and radiation energy

densities are zero inside the slab. Eqn. [4.26] asserts that at infinite time the radiation and material energy density equilibrate among themselves. However, because of the finite thickness of the slab, flux leaks out of the right edge so that the energy densities vary linearly along the length of the slab.

The solutions for $u_r(x,\tau)$ and $u_m(x,\tau)$ follow from $\bar{u}_r(x,s)$ and $\bar{u}_m(x,s)$ by inverting them using the Laplace inversion theorem

$$f(\tau) = \frac{1}{2\pi i}\int_C ds e^{s\tau}\bar{f}(s), \tag{4.27}$$

where the integration contour is a line parallel to the imaginary s axis to the right of all the singularities of $\bar{f}(s)$.The contour is closed in the left half plane so that the large semi circle gives a zero contribution. Both $\bar{u}_r(x,s)$ and $\bar{u}_m(x,s)$ are single valued functions and hence there are no branch points. However, there are an infinite number of poles obtained from the roots of the transcendental equation

$$\begin{aligned} 3\sin(\beta(s)b) + 4\sqrt{3}\beta(s)\cos(\beta(s)b) - 4\beta^2(s)\sin(\beta(s)b) = 0, \\ \text{or, } \tan(\beta(s)b) = \frac{4\sqrt{3}\beta(s)}{4\beta^2(s)-3}. \end{aligned} \tag{4.28}$$

For the semi infinite slab, because of the multiple valuedness of the functions obtained by Laplace transform, inverting them using the inverse Laplace transform required evaluation of contributions from all the branch cuts. This resulted in integrals which had to be computed numerically [64]. The oscillations in the integrand resulted in difficulty in their convergence. The advantage of solving the finite problem is that because of the single valuedness of the Laplace transformed functions, the inversion is very simple. The sum of the residues at the singularities (poles) give the required solution. The roots of the transcendental equation has been obtained using MATHEMATICA [97] as shown in the graph of figure 4.2.

Corresponding to each root of $\beta(s)$, there exists two values of s, i.e., two simple poles. The

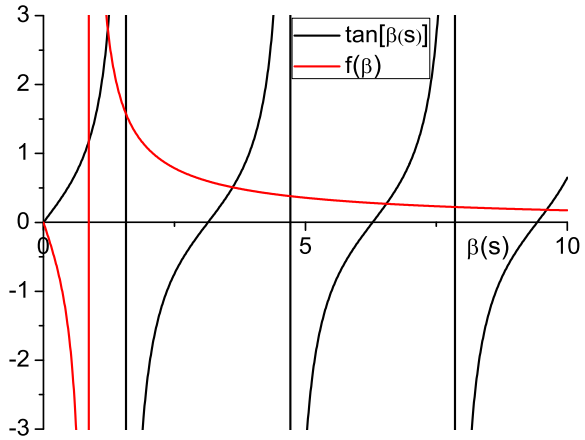

Figure 4.2: Finding the roots of the transcendental equation $\tan(\beta(s)) = f(\beta) = \frac{4\sqrt{3}\beta(s)}{4\beta^2(s)-3}$

poles are obtained from solution of eqn. [4.22] as

$$s = \frac{-[\varepsilon + \beta^2(s) + 1] \pm \sqrt{[\varepsilon + \beta^2(s) + 1]^2 - 4\varepsilon\beta^2(s)}}{2\varepsilon}. \tag{4.29}$$

According to the residue theorem, $\int_C ds e^{s\tau}\bar{f}(s) = 2\pi i \times$(sum of the residues at the singularities). The residue at s=0 gives the asymptotic (steady state) solution for the radiation and material energy densities as $u_r(x,\infty) = u_m(x,\infty) = \frac{3b+2\sqrt{3}-3x}{3b+4\sqrt{3}}$ which is also obtained by equating $\frac{\partial u_r(x,\tau)}{\partial \tau}$ and $\frac{\partial u_m(x,\tau)}{\partial \tau}$ in Eqs. (4.8) and (4.9) to zero, solving $\frac{\partial^2 u_r(x,\tau)}{\partial x^2} = 0$ and obtaining the values of the constants from the BC given by Eqs. (4.12) and (4.13).

The contribution to the time dependent part comes from the higher order poles. Adding residues from all the poles give us the complete space and time dependence of the radiation energy density as

$$u_r(x,\tau) = \frac{3b+2\sqrt{3}-3x}{3b+4\sqrt{3}} + \sum_n \frac{e^{s_n\tau}[3\sin(\beta(s_n)(b-x)) + 2\sqrt{3}\beta(s_n)\cos(\beta(s_n)(b-x))]}{s_n[Q(s_n)\cos(\beta(s_n)b) - R(s_n)\sin(\beta(s_n)b)]\frac{d\beta(s_n)}{ds}} \tag{4.30}$$

with

$$Q(s_n) = 3b + 4\sqrt{3} - 4\beta^2(s_n)b, \tag{4.31}$$

and

$$R(s_n) = 4\sqrt{3}\beta(s_n)b + 8\beta(s_n). \tag{4.32}$$

Similarly, the solution for the material energy density is

$$u_m(x,\tau) = \frac{3b + 2\sqrt{3} - 3x}{3b + 4\sqrt{3}} + \sum_n \frac{e^{s_n\tau}[3\sin(\beta(s_n)(b-x)) + 2\sqrt{3}\beta(s_n)\cos(\beta(s_n)(b-x))]}{s_n(s_n+1)[Q(s_n)\cos(\beta(s_n)b) - R(s_n)\sin(\beta(s_n)b)]\frac{d\beta(s_n)}{ds}} \tag{4.33}$$

We also consider the ε=0 case which arises when the speed of light is taken to be infinite so that radiation is not retarded initially. At infinite time, the radiation and material energy densities assume the same spatial dependence as for $\varepsilon \neq 0$ case.

$$u_r(x, \tau \to \infty) \to u_m(x, \tau \to \infty) \to \frac{3b + 2\sqrt{3} - 3x}{3b + 4\sqrt{3}}. \tag{4.34}$$

However, for $\tau = 0$, as $s \to \infty$ for $\varepsilon = 0$, we obtain $\beta = i$ where $i = \sqrt{-1}$. Thus,

$$u_r(x,0) = \frac{3\sinh(b-x) + 2\sqrt{3}\cosh(b-x)}{7\sinh(b) + 4\sqrt{3}\cosh(b)}, \tag{4.35}$$

$$u_m(x,0) = 0. \tag{4.36}$$

Thus the material energy density is zero at $\tau = 0$ as predicted by the initial condition. However, because of the absence of retardation effects, the radiation energy density attains a finite value consistent with the incoming flux of radiation. This behavior is in agreement with that obtained in the case of a semi infinite planar slab for the no retardation case.

The solution $u_r(x,\tau)$ and $u_m(x,\tau)$ for $\varepsilon = 0$ is obtained by inverting Eqs. (4.20) and (4.21)

using inverse Laplace transform as in the general case with $\varepsilon = 0$. The difference from the $\varepsilon \neq 0$ case is that only one pole is obtained corresponding to a value of beta i.e., $s = -\frac{\beta^2(s)}{\beta^2(s)+1}$.

4.2.1.2 Eigenfunction expansion method

To solve eqns. [4.8] - [4.13] using eigenfunction expansion method, we write the solution as the sum of an asymptotic (i.e., infinite time) and a transient part. Let us denote the asymptotic solutions for radiation and material energy densities by $u_r^0(x)$ and $u_m^0(x)$ respectively. Similarly the transient parts are denoted by $u_r^1(x,\tau)$ and $u_m^1(x,\tau)$. Then,

$$u_r(x,\tau) = u_r^0(x) + u_r^1(x,\tau), \tag{4.37}$$

$$u_m(x,\tau) = u_m^0(x) + u_m^1(x,\tau). \tag{4.38}$$

Obtaining the asymptotic solution

After infinite time, both $u_r(x,\tau)$ and $u_m(x,\tau)$ attain the asymptotic value so that $\frac{\partial u_r(x,\tau)}{\partial \tau} = 0$ and $\frac{\partial u_m(x,\tau)}{\partial \tau} = 0$. Therefore, $u_r(x,\tau) = u_m(x,\tau)$ and hence from eqn. [4.8],

$$\frac{\partial^2 u_r(x,\tau)}{\partial x^2} = 0. \tag{4.39}$$

The solution is $u_r^0(x,\tau) = c + dx$. The values of the constants c and d can be obtained from the BC given by eqns. [4.12] and [4.13]. Omitting the algebra, the obtained solution is

$$u_r^0(x,\tau) = \frac{2 + \sqrt{3}b - \sqrt{3}x}{4 + \sqrt{3}b}. \tag{4.40}$$

Obtaining the transient solution

The equations for the transient parts $u_r^1(x,\tau)$ and $u_m^1(x,\tau)$ are

$$\varepsilon\frac{\partial u_r^1(x,\tau)}{\partial \tau} = \frac{\partial^2 u_r^1(x,\tau)}{\partial x^2} + u_m^1(x,\tau) - u_r^1(x,\tau), \tag{4.41}$$

$$\frac{\partial u_m^1(x,\tau)}{\partial \tau} = u_r^1(x,\tau) - u_m^1(x,\tau). \tag{4.42}$$

with the initial conditions

$$u_r^1(x,0) = -u_r^0(x) \tag{4.43}$$

$$u_m^1(x,0) = -u_m^0(x) \tag{4.44}$$

$$\tag{4.45}$$

and the homogeneous BC on the surfaces are

$$u_r^1(0,\tau) - \frac{2}{\sqrt{3}}\frac{\partial u_r^1(0,\tau)}{\partial x} = 0, \tag{4.46}$$

$$u_r^1(b,\tau) + \frac{2}{\sqrt{3}}\frac{\partial u_r^1(b,\tau)}{\partial x} = 0. \tag{4.47}$$

The eigen value equation (EVE) is given by

$$\frac{\partial^2 \phi}{\partial x^2} + \beta^2\phi = 0 \tag{4.48}$$

where ϕ is the eigenvector and β is the eigenvalue. BCs on ϕ are

$$\phi(0,\tau) - \frac{2}{\sqrt{3}}\frac{\partial \phi(0,\tau)}{\partial x} = 0, \tag{4.49}$$

$$\phi(b,\tau) + \frac{2}{\sqrt{3}}\frac{\partial \phi(b,\tau)}{\partial x} = 0. \tag{4.50}$$

The EVE can be solved and we can determine an infinite set of normalized and orthogonal eigen functions and corresponding eigen values. Thus corresponding to a particular eigen value we

have

$$\frac{\partial^2 \phi_n}{\partial x^2} + \beta_n^2 \phi_n = 0, \tag{4.51}$$

$$\int_0^b \phi_m(x)\phi_n(x)dx = \delta_{mn}, m, n = 1, 2, 3, ... \tag{4.52}$$

As these form a complete set, we expand the solutions in terms of these eigen functions:

$$u_r^1(x, \tau) = \sum_n a_n(\tau)\phi_n(x), \tag{4.53}$$

$$u_m^1(x, \tau) = \sum_n b_n(\tau)\phi_n(x), \tag{4.54}$$

where the expansion coefficients $a_n(\tau)$ and $b_n(\tau)$ have to be determined. From the orthogonal and normalization conditions of $\phi_n(x)$ we have

$$a_n(\tau) = \int_0^b \phi_n(x)u_r^1(x, \tau)dx, \tag{4.55}$$

$$b_n(\tau) = \int_0^b \phi_n(x)u_m^1(x, \tau)dx. \tag{4.56}$$

Multiplying both sides of eqns. [4.41] and [4.42] with $\phi_n(x)$, integrating over x from 0 to b, and using the boundary conditions at the surfaces viz. eqns. [4.46], [4.47], [4.49] and [4.50] along with eqns. [4.55] and [4.56], we obtain ODEs involving the expansion coefficients $a_n(\tau)$ and $b_n(\tau)$.

$$\varepsilon \frac{da_n(\tau)}{d\tau} + (1 + \beta_n^2)a_n(\tau) - b_n(\tau) = 0, \tag{4.57}$$

$$\frac{db_n(\tau)}{d\tau} + b_n(\tau) - a_n(\tau) = 0, \tag{4.58}$$

with the initial condition on the expansion coefficients as

$$a_n(0) = -\int_0^b \phi_n(x) u_r^0(x) dx, \tag{4.59}$$

$$b_n(0) = -\int_0^b \phi_n(x) u_m^0(x) dx. \tag{4.60}$$

The solution of the EVE, i.e., eqn. [4.98] is given by

$$\phi(x) = A\sin(\beta x + B) = C^*[\sin(\beta x) + \frac{2\beta}{\sqrt{3}}\cos(\beta x)]. \tag{4.61}$$

From the normalization condition of the eigenfuncion ϕ i.e., $\int_0^b \phi^2(x)dx = 1$ and the BC on ϕ at x=0 (Eqn. [4.49]), the value of the normalization constant is obtained as

$$C^* = \sqrt{\frac{12\beta}{4\sqrt{3}\beta + (6\beta + 8\beta^3)b + (4\beta^2 - 3)\sin(2\beta b) - 4\sqrt{3}\beta\cos(2\beta b)}}. \tag{4.62}$$

The eigen values are obtained by applying the BC on ϕ i.e., eqns. [4.49] and [4.50]. The conditions are

$$\sin B - \frac{2}{\sqrt{3}}\beta\cos B = 0, \tag{4.63}$$

$$(\cos(\beta b) - \frac{2}{\sqrt{3}}\beta\sin(\beta b))\sin B + (\sin(\beta b) + \frac{2}{\sqrt{3}}\beta\cos(\beta b))\cos B = 0. \tag{4.64}$$

We will have nontrivial solutions if the system in sinB and cosB is singular so that the determinant of coefficients vanishes. This condition gives us the same transcendental equation viz. eqn. [4.28] for the eigenvalue β. As in the Laplace transform method, the eigenvalues are obtained as roots of this equation. For a particular eigenvalue β_n, the ODEs involving the expansion coefficients $a_n(\tau)$ and $b_n(\tau)$ are solved using MATHEMATICA and $\phi_n(x)$ is obtained from eqn. [4.61]. Summing the contribution from all the eigenvalues give the transient solutions for scaled radiation and material energy densities using eqns. [4.53] and [4.54]. Adding the steady state

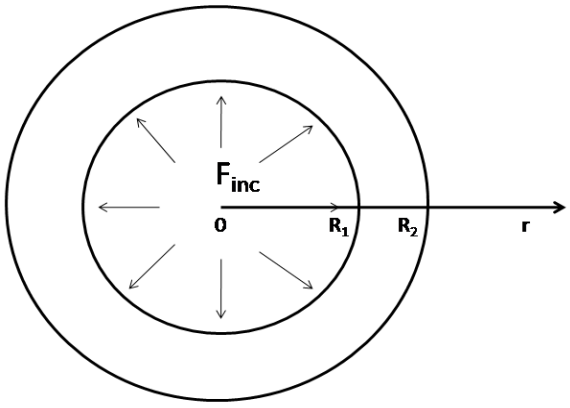

Figure 4.3: Flux incident on the inner surface of a spherical shell of inner radius R_1 and outer radius R_2.

solution to the transient part gives the final solution.

4.2.2 Spherical shell

Analogous to the planar slab problem, in spherical geometry we consider a spherical shell of inner and outer radii R_1 and R_2 respectively (figure 4.3). Under the same assumptions, with a time independent radiative flux (F_{inc}) incident on the inner surface of the shell, the one group radiative transfer equation (RTE) in the diffusion approximation and the material energy balance equation (ME) in spherical geometry are

$$\frac{\partial E_r(r,t)}{\partial t} - \frac{1}{r^2}\frac{\partial}{\partial r}[\frac{r^2 c}{3\sigma_a(T)}\frac{\partial E_r(r,t)}{\partial r}] = c\sigma_a(T)[aT^4(r,t) - E_r(r,t)], \tag{4.65}$$

$$C_V(T)\frac{\partial T(r,t)}{\partial t} = c\sigma_a(T)[E_r(r,t) - aT^4(r,t)], \tag{4.66}$$

with the same notations as used in Subsec. 4.2.1

The Marshak boundary condition on the inner surface at $r = R_1$ is given by

$$E_r(R_1,t) - \left(\frac{2}{3\sigma_a[T(R_1,t)]}\right)\frac{\partial E_r(R_1,t)}{\partial r} = \frac{4}{c}F_{inc}. \tag{4.67}$$

And that at $r = R_2$ is

$$E_r(R_2, t) + \left(\frac{2}{3\sigma_a[T(R_2, t)]}\right) \frac{\partial E_r(R_2, t)}{\partial r} = 0. \tag{4.68}$$

With new dimensionless variables introduced in Subsec. 4.2.1, the RTE and ME take the dimensionless form

$$\varepsilon \frac{\partial u_r(x,\tau)}{\partial \tau} = \frac{1}{x^2}\frac{\partial}{\partial x}(x^2 \frac{\partial u_r(x,\tau)}{\partial x}) + u_m(x,\tau) - u_r(x,\tau), \tag{4.69}$$

$$\frac{\partial u_m(x,\tau)}{\partial \tau} = u_r(x,\tau) - u_m(x,\tau), \tag{4.70}$$

with the initial conditions

$$u_r(x, 0) = 0, \tag{4.71}$$

$$u_m(x, 0) = 0. \tag{4.72}$$

And the boundary conditions on the surfaces are

$$u_r(X_1,\tau) - \frac{2}{\sqrt{3}}\frac{\partial u_r(X_1,\tau)}{\partial x} = 1, \tag{4.73}$$

$$u_r(X_2,\tau) + \frac{2}{\sqrt{3}}\frac{\partial u_r(X_2,\tau)}{\partial x} = 0, \tag{4.74}$$

where $x = \sqrt{3}\sigma_a r$. Changing variable $u_r(x,\tau)$ to $w(x,\tau) = u_r(x,\tau)x$ and $u_m(x,\tau)$ to $g(x,\tau) = u_m(x,\tau)x$, the equations simplify to

$$\varepsilon \frac{\partial w(x,\tau)}{\partial \tau} = \frac{\partial^2 w(x,\tau)}{\partial x^2} + g(x,\tau) - w(x,\tau), \tag{4.75}$$

$$\frac{\partial g(x,\tau)}{\partial \tau} = w(x,\tau) - g(x,\tau). \tag{4.76}$$

4.2.2.1 Laplace transform method

Applying Laplace transform, the solution in s space are obtained as

$$\bar{u}_r(x,s) = \frac{A}{\beta(s)x}\sin(\beta(s)x + B), \tag{4.77}$$

$$\bar{u}_m(x,s) = \frac{\bar{u}_r(x,s)}{s+1}, \tag{4.78}$$

with the constants A and B obtained from the BCs

$$\bar{u}_r(X_1,s) - \frac{2}{\sqrt{3}}\frac{\partial \bar{u}_r(X_1,s)}{\partial x} = \frac{1}{s}, \tag{4.79}$$

$$\bar{u}_r(X_2,s) + \frac{2}{\sqrt{3}}\frac{\partial \bar{u}_r(X_2,s)}{\partial x} = 0. \tag{4.80}$$

Then the Laplace transformed radiation energy density is given by

$$\bar{u} = \frac{\sqrt{3}X_1^2[(2-\sqrt{3}X_2)\sin(\beta(s)(X_2-x)) - 2\beta(s)X_2\cos(\beta(s)(X_2-x))]}{sx[S(s)\sin\beta(s)(X_2-X_1) - T(s)\cos(\beta(s)(X_2-X_1))]}, \tag{4.81}$$

with

$$S(s) = (4\beta^2(s)-3)X_1X_2 - 2\sqrt{3}(X_2-X_1) + 4, \tag{4.82}$$

and

$$T(s) = 4\beta(s)(X_2-X_1) + 4\sqrt{3}\beta(s)X_1X_2. \tag{4.83}$$

As in the case of the finite planar slab, the solutions for $u_r(x,\tau)$ and $u_m(x,\tau)$ follow from $\bar{u}_r(x,s)$ and $\bar{u}_m(x,s)$ by inverting them using the Laplace inversion theorem. An infinite num-

ber of poles are obtained from the roots of the transcendental equation

$$\tan(\beta(s)(X_2 - X_1)) = \frac{4\sqrt{3}\beta(s)X_2X_1 + 4\beta(s)(X_2 - X_1)}{(4\beta(s)^2 - 3)X_1X_2 - 2\sqrt{3}(X_2 - X_1) + 4}. \tag{4.84}$$

Summing over the residues at all the poles, the radiation energy density is obtained as

$$u_r(x,\tau) = \frac{\sqrt{3}X_1^2X_2^2 + X_1^2x(2 - \sqrt{3}X_2)}{x[2X_1^2 - \sqrt{3}X_1^2X_2 + \sqrt{3}X_1X_2^2 + 2X_2^2]}$$
$$+ \sum_n \left(\frac{[(2 - \sqrt{3}X_2)\sin(\beta(s_n)(X_2 - x)) - 2\beta(s_n)X_2\cos(\beta(s_n)(X_2 - x))]}{[Y(s_n)\sin\beta(s_n)(X_2 - X_1) + Z(s_n)\cos(\beta(s_n)(X_2 - X_1))]} \times \frac{e^{s_n\tau}\sqrt{3}X_1^2}{s_nx\frac{d\beta(s_n)}{ds}} \right) \tag{4.85}$$

with

$$Y(s_n) = 4\beta^2(s_n)(X_2^2 + X_1^2) + 4\sqrt{3}\beta(s_n)X_1X_2(X_2 - X_1), \tag{4.86}$$

and

$$Z(s_n) = 4\beta^2(s_n)X_1X_2(X_2 - X_1) - 3X_1X_2(X_2 - X_1) - 2\sqrt{3}(X_1^2 + X_2^2). \tag{4.87}$$

Similarly, the solution for the material energy density follows the same form as that for the radiation energy density with an extra $(s_n + 1)$ in the denominator of the second term.

4.2.2.2 Eigenfunction expansion method

In a manner similar to the finite planar slab, the solution is assumed to be the sum of an asymptotic (i.e., infinite time) and a transient part given by eqns. [4.37] and [4.38].

Obtaining the asymptotic solution

The asymptotic solution is

$$u_r^0(x) = u_m^0(x) = \frac{\sqrt{3}X_1^2X_2^2 + X_1^2x(2-\sqrt{3}X_2)}{x(2X_1^2 - \sqrt{3}X_1^2X_2 + \sqrt{3}X_1X_2^2 + 2X_2^2)}, \tag{4.88}$$

$$\frac{\partial u_r^0(x)}{\partial x} = \frac{\partial u_m^0(x)}{\partial x} = \frac{3X_1^3X_2^3(X_1 - X_2) - 2\sqrt{3}X_1^2X_2^2(X_1^2 + X_2^2)}{x^2(2X_1^2 - \sqrt{3}X_1^2X_2 + \sqrt{3}X_1X_2^2 + 2X_2^2)^2}. \tag{4.89}$$

The outgoing flux from the surface of the sphere j+ in the asymptotic limit is

$$u_r^0(X_2) - \frac{2}{\sqrt{3}}\frac{\partial u_r^0(X_2,\tau)}{\partial x} = \frac{4X_1^2}{2X_1^2 - \sqrt{3}X_1^2X_2 + \sqrt{3}X_1X_2^2 + 2X_2^2}, \tag{4.90}$$

and the flux j- coming out of the inner surface is

$$u_r^0(X_1) + \frac{2}{\sqrt{3}}\frac{\partial u_r^0(X_1,\tau)}{\partial x} = \frac{4X_1^6 + 3X_1^4X_2^2 - 4\sqrt{3}X_1^4X_2 + 4\sqrt{3}X_1^3X_2^2 - 6X_1^3X_2^3 + 3X_1^2X_2^4 - 4X_2^4}{(2X_1^2 - \sqrt{3}X_1^2X_2 + \sqrt{3}X_1X_2^2 + 2X_2^2)^2}. \tag{4.91}$$

Obtaining the transient solution

The equations for the transient parts $u_r^1(x,\tau)$ and $u_m^1(x,\tau)$ are

$$\varepsilon\frac{\partial u_r^1(x,\tau)}{\partial \tau} = \frac{1}{x^2}\frac{\partial}{\partial x}(x^2\frac{\partial u_r^1(x,\tau)}{\partial x}) + u_m^1(x,\tau) - u_r^1(x,\tau), \tag{4.92}$$

$$\frac{\partial u_m^1(x,\tau)}{\partial \tau} = u_r^1(x,\tau) - u_m^1(x,\tau), \tag{4.93}$$

with the initial conditions

$$u_r^1(x,0) = -u_r^0(x), \tag{4.94}$$

$$u_m^1(x,0) = -u_m^0(x), \tag{4.95}$$

with the homogeneous BC on the inner and outer surface

$$u_r^1(X_1,\tau) - \frac{2}{\sqrt{3}}\frac{\partial u_r^1(X_1,\tau)}{\partial x} = 0, \tag{4.96}$$

$$u_r^1(X_2,\tau) + \frac{2}{\sqrt{3}}\frac{\partial u_r^1(X_2,\tau)}{\partial x} = 0. \tag{4.97}$$

The eigen value equation (EVE) is given by

$$\frac{1}{x^2}\frac{\partial}{\partial x}(x^2\frac{\partial \phi}{\partial x}) + \beta^2\phi = 0. \tag{4.98}$$

BCs on ϕ are

$$\phi(X_1) - \frac{2}{\sqrt{3}}\frac{\partial \phi(X_1)}{\partial x} = 0, \tag{4.99}$$

$$\phi(X_2) + \frac{2}{\sqrt{3}}\frac{\partial \phi(X_2)}{\partial x} = 0. \tag{4.100}$$

The EVE can be solved and we can determine an infinite set of normalized and orthogonal eigen functions and corresponding eigen values. Thus corresponding to a particular eigen value we have

$$\frac{1}{x^2}\frac{\partial}{\partial x}(x^2\frac{\partial \phi_n}{\partial x}) + \beta_n^2\phi_n = 0, \tag{4.101}$$

$$\int_{X_1}^{X_2} \phi_m(x)\phi_n(x)4\pi x^2 dx = \delta_{mn}, m, n = 1, 2, 3, ... \tag{4.102}$$

Following the same steps as for the finite planar slab, by integrating over the volume $\frac{4\pi x^3}{3}$ with x going from X_1 to X_2, we obtain the solution of the eigenvalue equation as

$$\phi(x) = \frac{C^*}{x}\left[\sin(\beta x) + \cos(\beta x)\frac{(X_2 - \frac{2}{\sqrt{3}})\sin(\beta X_2) + \frac{2X_2\beta}{\sqrt{3}}\cos(\beta X_2)}{\frac{2X_2\beta}{\sqrt{3}}\sin(\beta X_2) - (X_2 - \frac{2}{\sqrt{3}})\cos(\beta X_2)}\right], \tag{4.103}$$

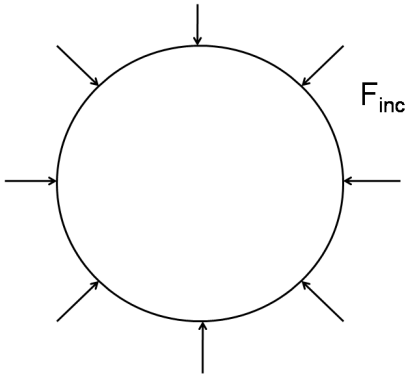

Figure 4.4: Radiation flux incident on the outer surface of a sphere.

with $C^* = A\cos B$. From the normalization condition of the eigenfuncion ϕ i.e., $\int_{X_1}^{X_2} \phi^2(x) 4\pi x^2 dx = 1$, the value of the normalization constant is obtained as

$$C^* = \sqrt{\frac{1}{4\pi \int_{X_1}^{X_2} \frac{[(X_2 - \frac{2}{\sqrt{3}}) \sin\beta(X_2 - x) + \frac{2X_2\beta}{\sqrt{3}} \cos\beta(X_2 - x)]^2}{[\frac{2X_2\beta}{\sqrt{3}} \sin(\beta X_2) - (X_2 - \frac{2}{\sqrt{3}}) \cos(\beta X_2)]^2} dx}}. \tag{4.104}$$

From the b.c. on ϕ, the same transcendental equation (eqn. [4.84]) as in the Laplace transform method is obtained for the eigenvalue β. Finally, the scaled radiation and material energy densities are obtained.

4.2.3 Sphere

We consider a sphere of radius R with a radiative flux incident on the outer surface as shown in figure 4.4 The radiation transport and material equation are the same as eqns. [4.69] and [4.70]. The boundary conditions on the surface and centre are given by

$$u_r(X, \tau) + \frac{2}{\sqrt{3}} \frac{\partial u_r(X, \tau)}{\partial x} = 0, \tag{4.105}$$

$$u_r(0, \tau) = \text{finite}. \tag{4.106}$$

4.2.3.1 Laplace transform method

In a manner similar to the spherical shell, the Laplace transformed radiation energy density is given by

$$\bar{u}_r(x,s) = \frac{\sqrt{3}X^2 \sin(\beta(s_n)x)}{sx[(\sqrt{3}X-2)\sin(\beta(s_n)X) + 2\beta(s_n)X\cos(\beta X)]}. \tag{4.107}$$

The transcendental equation in this case is

$$\tan(\beta(s_n)X) = \frac{2\beta(s_n)X}{2-\sqrt{3}X}. \tag{4.108}$$

The radiation energy density is obtained as

$$u_r(x,\tau) = 1 + \sum_n \frac{e^{s_n\tau}\sqrt{3}\sin(\beta(s_n)X)}{s_n x[\sqrt{3}\cos(\beta(s_n)X) - 2\beta(s_n)\sin(\beta(s_n)X)]\frac{d\beta(s_n)}{ds}}. \tag{4.109}$$

4.2.3.2 Eigenfunction expansion method

The asymptotic solution is obtained as

$$u_r^0(x) = u_m^0(x) = 1, \tag{4.110}$$

and as in the finite spherical shell, we obtain the solution of the eigenvalue equation as

$$\phi(x) = \sqrt{\frac{\beta}{\pi[2\beta X - \sin(2\beta X)]}}\frac{\sin(\beta x)}{x}, \tag{4.111}$$

with the same transcendental equation 4.108 for the eigenvalue β. The scaled radiation and material energy densities are also obtained in a manner similar to the planar slab and spherical shell.

4.3 Results and discussions

4.3.1 Planar slab

For the finite planar slab, at early stages (τ=0.01) the radiation energy density falls rapidly from the left surface where radiation is incident as shown in figure 4.5. As time proceeds, the values of energy densities increase and the variation with distance keeps on attaining linearity. At infinite time, the steady state values are linear with position as given by eqn. [4.26]. Similarly, the material energy density initially exhibits slight non-linear variation and finally attains the linearity (figure 4.6). The non-linear variation at early stages occurs due to net absorption of energy by the initially cold material (as $u_r(x,0) = u_m(x,0) = 0$). Initially, the material energy density is found to lag behind the radiation energy densities and finally equilibrate as time proceeds (beyond τ=10). In this work, all the results have been obtained by considering contribution from the first 30 roots of the transcendental equation. The value of opacity σ_a is chosen to be 100 and ε equals 0.1. For a heat wave traveling into a thin plate and composite planar slab, a similar linear variation in temperature with distance was observed though difference existed in the space and time dependent behaviour due to heat conduction approximation [98],[99].

The first derivatives w.r.t. position of the analytical radiation and material energy density are plotted in figures 4.7 and 4.8. As the radiation and material energy densities decrease with x, the derivative has negative values. The derivative has a greater negative value at the left compared to the right zone. As both radiation and material energy densities keep on increasing with time due to radiation diffusion, magnitude of the gradient decreases for the left and increases for the right sides. The gradient of both radiation and material energy densities obtain a constant value of $\frac{-3}{3+4\sqrt{3}} = -0.30217$ after infinite time showing that there is a constant leakage of flux from the right surface due to the finite thickness. This result is different from the semi-infinite slab result where at infinite time, the entire halfspace is at a constant temperature with a uniform radiation field and hence there is no gradient and no flux [63].

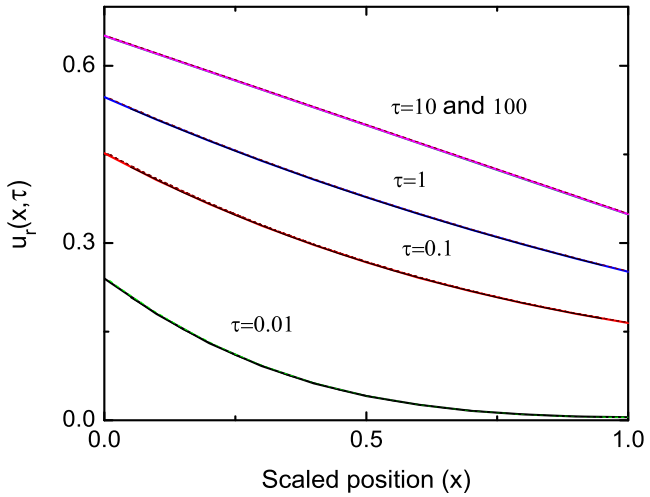

Figure 4.5: Scaled radiation energy density $u_r(x,\tau)$ Vs. position (x) in the slab of scaled thickness $b = 1$ at different times for $\varepsilon = 0.1$.

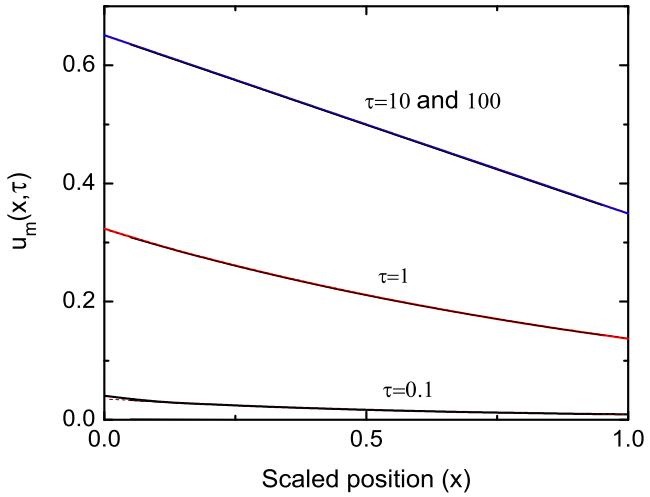

Figure 4.6: Scaled material energy density $u_m(x,\tau)$ Vs. position (x) in the slab at different times for $\varepsilon = 0.1$.

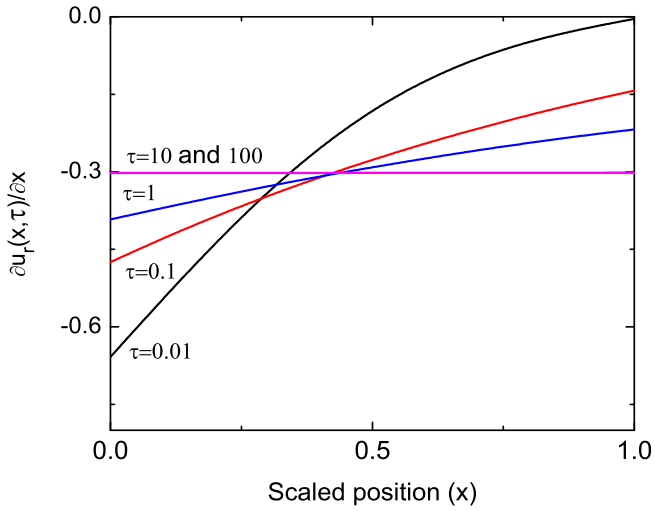

Figure 4.7: Space derivative of scaled radiation energy density $\partial u_r(x,\tau)/\partial x$ Vs. position (x) in the slab at different times.

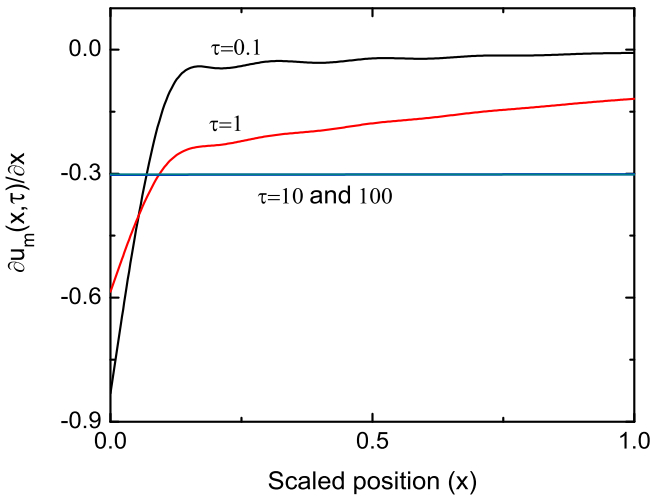

Figure 4.8: Space derivative of scaled material energy density $\partial u_m(x,\tau)/\partial x$ Vs. position (x) in the slab at different times.

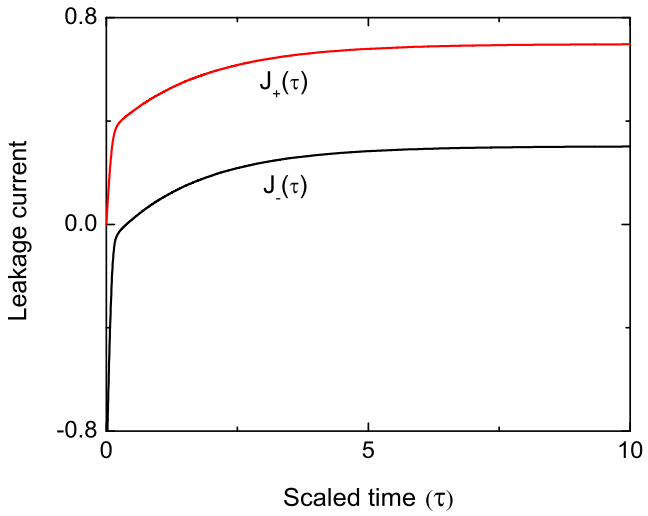

Figure 4.9: Leakage currents $J_-(\tau)$ and $J_+(\tau)$ from the left and right surfaces of the slab respectively.

The current of radiation leaking out from the left and right surfaces of the slab are $J_-(\tau) = u_r(0,\tau) + \frac{2}{\sqrt{3}}\frac{\partial u_r(0,\tau)}{\partial x}$ and $J_+(\tau) = u_r(b,\tau) - \frac{2}{\sqrt{3}}\frac{\partial u_r(b,\tau)}{\partial x}$. The leakage currents are plotted as a function of time in figure 4.9. It is found that though $J_-(\tau)$ is negative initially, it attains a constant positive value of 0.30217 after saturation. $J_+(\tau)$ is zero initially as the incident flux has not reached the right face. However it rises rapidly and reaches a saturation value of 0.6978. The energy densities and leakage currents at the left and right surfaces are also related as $u_r(0,\tau) + u_r(b,\tau) = 1$ and $J_-(\tau) + J_+(\tau) = 1$.

The averaged or integrated radiation and material energy densities are given by $\psi_r(\tau) = \int_0^b u_r(x,\tau)dx$ and $\psi_m(\tau) = \int_0^b u_m(x,\tau)dx$ respectively. The steady state integrated value is 0.5 as seen from figure 4.10. The integrated material energy density is also found to lag the radiation energy density at early times but finally the two equilibrate.

To check the consistency of the final results, we add Eqs. (4.8) and (4.9) and integrate over x from 0 to b, yielding

$$\int_0^b (\varepsilon\frac{\partial u_r(x,\tau)}{\partial \tau} + \frac{\partial u_m(x,\tau)}{\partial \tau})dx = \int_0^b \frac{\partial^2 u_r(x,\tau)}{\partial x^2}dx = \frac{\partial u_r(b,\tau)}{\partial x} - \frac{\partial u_r(0,\tau)}{\partial x},$$

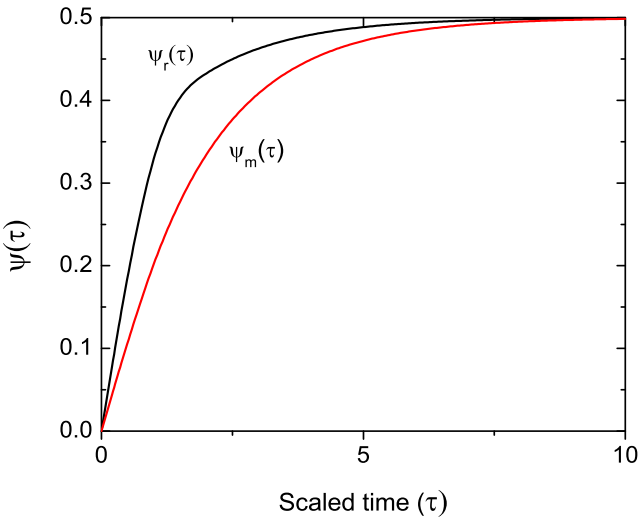

Figure 4.10: Integrated radiation ($\psi_r(\tau)$) and material energy densities ($\psi_m(\tau)$) in the slab as a function of scaled time τ.

i.e.,

$$\varepsilon\frac{\partial\psi_r(\tau)}{\partial\tau}+\frac{\partial\psi_m(\tau)}{\partial\tau}=\frac{\partial u_r(b,\tau)}{\partial x}-\frac{\partial u_r(0,\tau)}{\partial x}. \tag{4.112}$$

Using the expressions for the energy densities, their first derivatives in space and the integrated quantities, we find that both the left and right hand sides reduce to

$\sum_n \frac{e^{s_n\tau}}{[Q(s_n)\cos(\beta(s_n)b)-R(s_n)\sin(\beta(s_n)b)]\frac{d\beta(s_n)}{ds}} \times [\frac{3}{\beta(s_n)}(1-\cos(\beta(s_n)b))+2\sqrt{3}\sin(\beta(s_n)b)](\varepsilon+\frac{1}{s_n+1})$ proving the consistency of the obtained solutions.

As there are infinite number of residues, the exact solution is obtained only on adding all of them. However, the contribution from the poles decrease very sharply. To study convergence, we plot percentage error as a function of number of roots of the transcendental equation considered. As seen from figure 4.11, 2.1 $\%$ error in the value of $u_r(0,2.5)$ is observed on considering only the first two roots i.e., the steady state result and residue for the two non zero poles. The errors arising due to non inclusion of higher order terms is more initially as the higher order poles

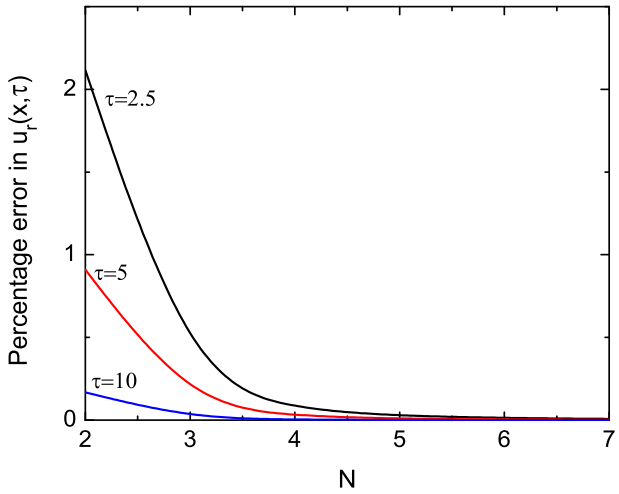

Figure 4.11: Percentage error in the radiation energy density $u_r(x,\tau)$ in the slab as a function of number of roots considered (N).

contribute only at very small times because of the exponential term. The error falls sharply to a negligible value (0.005%) on considering the contribution from the first 6 roots i.e., first 11 poles. More accurate results can be obtained by adding residues from higher order poles.

Figure 4.12 shows the plot of radiation energy density $u_r(x,\tau)$ as a function of space and time for $\varepsilon = 0$. Contrary to the results for finite ε, the radiation energy density attains a finite value even at very early times due to the absence of retardation effects. However, the material energy density shows the same trend as for finite ε.

4.3.2 Spherical shell

For the spherical shell, initially (τ=0.01) the radiation energy density falls rapidly from the inner surface (scaled radius $X_1 = 1$) where radiation is incident towards the outer surface (scaled radius $X_2 = 2$) as shown in figure 4.13. Though the trend is similar to the planar slab, the values of the scaled energy densities are less. Also, contrary to the planar case, the variation in energy densities remain sharper in the inner meshes compared to the outer ones and the variations in

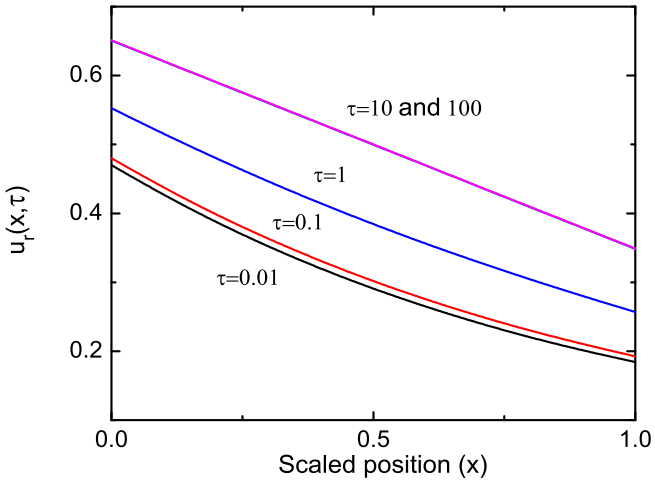

Figure 4.12: Scaled radiation energy density $u_r(x,\tau)$ Vs. position (x) in the slab of scaled thickness $b = 1$ at different times for $\varepsilon = 0$.

energy densities are not linear with position even after attaining steady state. This is evident because the mass of the material to be heated in the radially outward direction increases. Similar to the planar slab, the material energy density lags behind the radiation energy densities at early stages and finally reaches equilibrium (beyond τ=10) [figure 4.14]. Magnitude of derivative of analytical radiation and material energy densities remain higher in the inner meshes as compared to outer ones at all times [figures 4.15 and 4.16]. The leakage currents from the inner and outer surfaces of the spherical shell are $J_-(\tau) = u_r(X_1,\tau) + \frac{2}{\sqrt{3}}\frac{\partial u_r(X_1,\tau)}{\partial x}$,

$J_+(\tau) = u_r(X_2,\tau) - \frac{2}{\sqrt{3}}\frac{\partial u_r(X_2,\tau)}{\partial x}$.

The variation in $J_+(\tau)$ is similar to planar slab though the values are less. However, $J_-(\tau)$ remains negative throughout as radiation always diffuses outwards in order to maintain the flux boundary conditions (figure 4.17). As the derivative $\partial u_r(x,\tau)/\partial x$ is more negative for inner radii, $u_r(X_1,\tau) + u_r(X_2,\tau) < 1$ which leads to $J_+(\tau) + J_-(\tau) < 1$. For the case considered, $X_1 = 1$ and $X_2 = 2$, it is found that $2u_r(X_1,\tau) < 1$. As $J_-(\tau) = 2u_r(X,\tau) - 1$, hence $J_-(\tau)$ is negative. The averaged or integrated radiation and material energy densities are given by

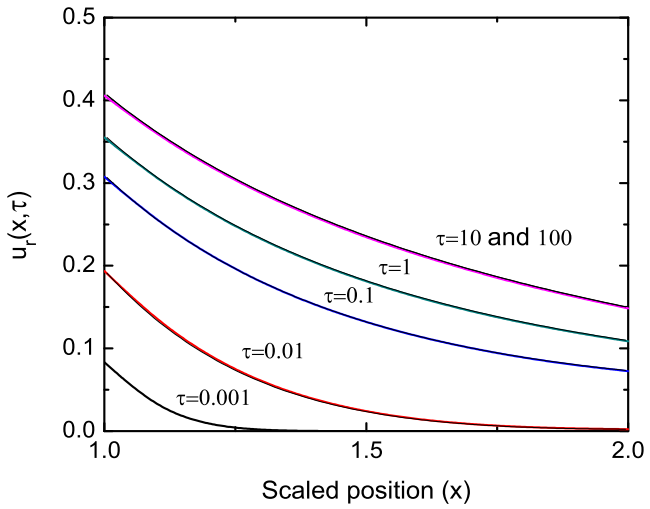

Figure 4.13: Scaled radiation energy density $u_r(x,\tau)$ Vs. position (x) in a spherical shell of scaled inner radius $X_1 = 1$ and outer radius $X_2 = 2$ at different times for $\varepsilon = 0.1$.

$\psi_r(\tau) = \int_{X_1}^{X_2} u_r(x,\tau) 4\pi x^2 dx$ and $\psi_m(\tau) = \int_{X_1}^{X_2} u_m(x,\tau) 4\pi x^2 dx$. and plotted in figure 4.18. The integrated material energy density is also found to lag the radiation energy density at early times but finally the two equilibrate to a value of 0.25.

To check the consistency of the final results, we add Eqs. (4.69) and (4.70) and integrate over x from X_1 to X_2, yielding

$$\int_{X_1}^{X_2} (\varepsilon \frac{\partial u_r(x,\tau)}{\partial \tau} + \frac{\partial u_m(x,\tau)}{\partial \tau}) 4\pi x^2 dx = 4\pi (X_2^2 \frac{\partial u_r(X_2,\tau)}{\partial x} - X_1^2 \frac{\partial u_r(X_1,\tau)}{\partial x}). \quad (4.113)$$

Using the expressions for the energy densities, we find that both the left and right hand sides reduce to the same expression proving the consistency of the obtained solutions.

As for the planar slab, convergence of relative error in radiation energy density for spherical shell on increasing contribution from higher order poles is found to follow the same trend. However, the values of relative errors are slightly higher (3.4% for $u_r(0, 2.5)$ for contribution from first 2 roots) than the planar slab as shown in figure 4.19. Thus for these finite systems,

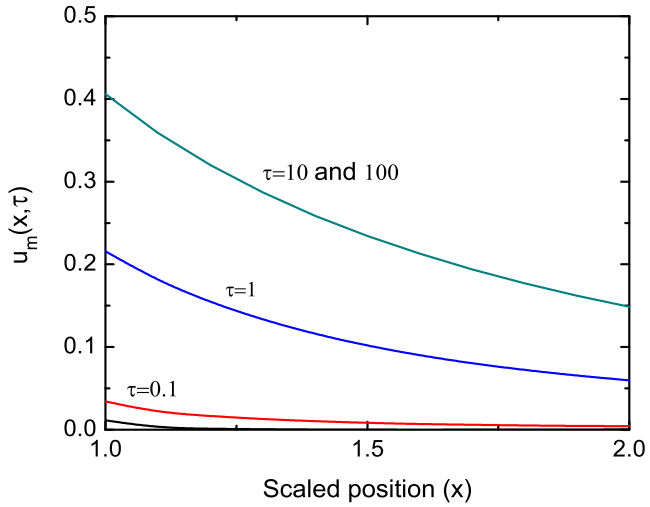

Figure 4.14: Scaled material energy density $u_m(x,\tau)$ Vs. position in a spherical shell of scaled inner radius $X_1 = 1$ and outer radius $X_2 = 2$ at different times for $\varepsilon = 0.1$.

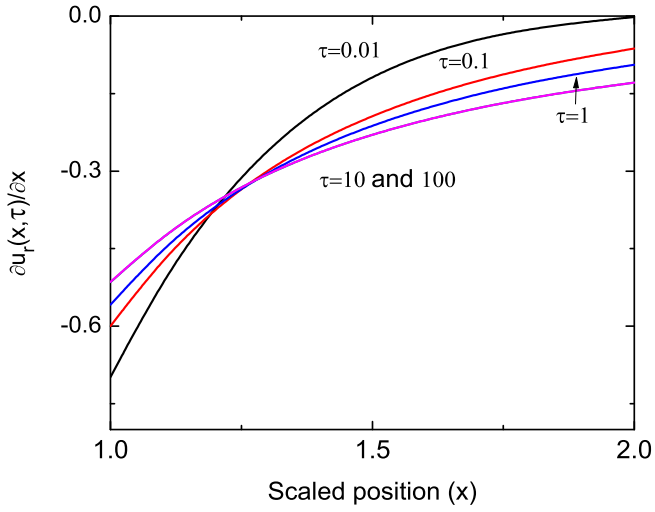

Figure 4.15: Space derivative of scaled radiation energy density $\partial u_r(x,\tau)/\partial x$ Vs. position (x) in the spherical shell at different times.

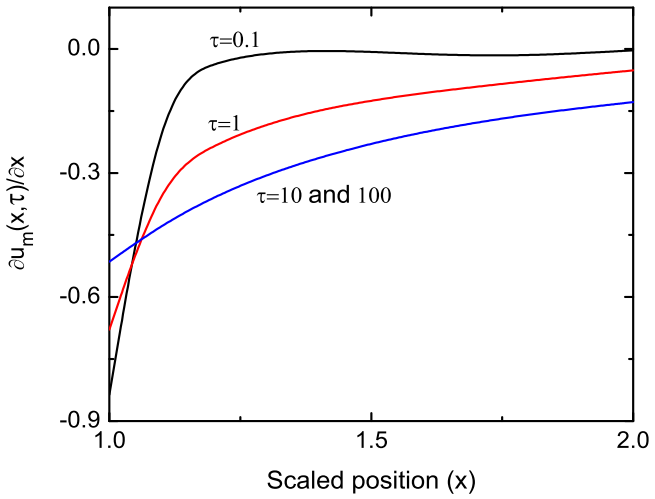

Figure 4.16: Space derivative of scaled material energy density $\partial u_m(x,\tau)/\partial x$ Vs. position (x) in the spherical shell at different times.

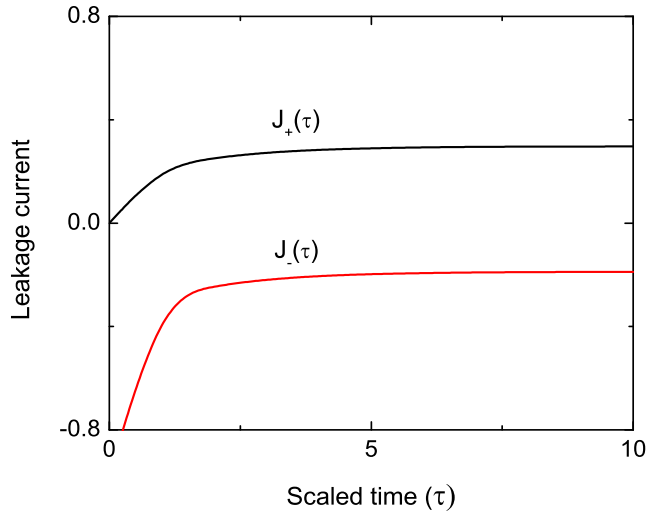

Figure 4.17: Leakage currents $J_{-}(\tau)$ and $J_{+}(\tau)$ from the inner and outer surfaces of the spherical shell respectively.

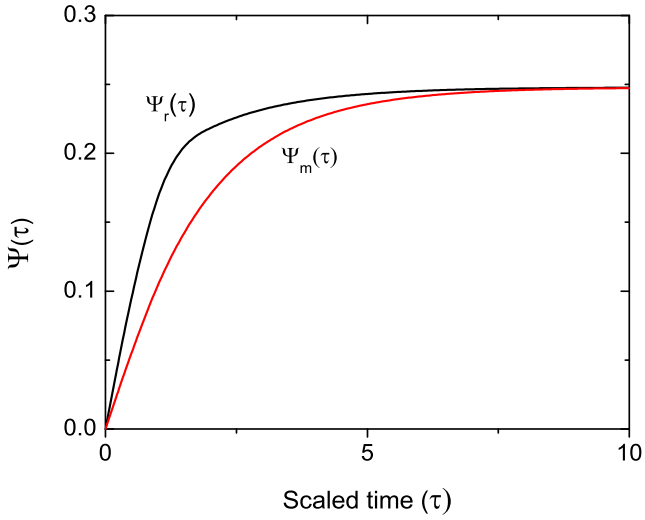

Figure 4.18: Integrated radiation ($\psi_r(\tau)$) and material energy densities ($\psi_m(\tau)$) in the spherical shell as a function of scaled time τ.

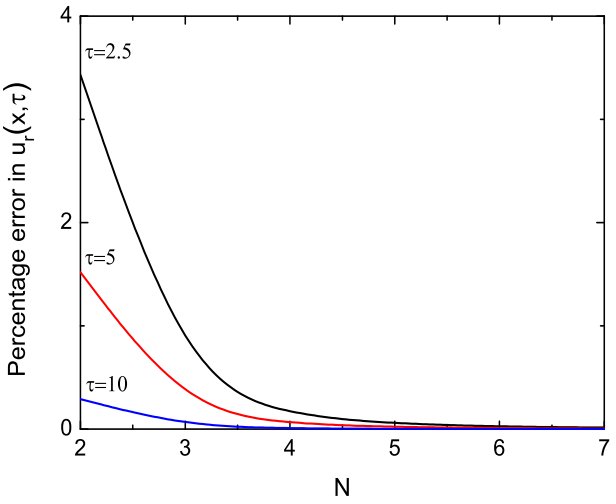

Figure 4.19: Percentage error in the radiation energy density $u_r(x, \tau)$ in the spherical shell as a function of number of roots considered (N).

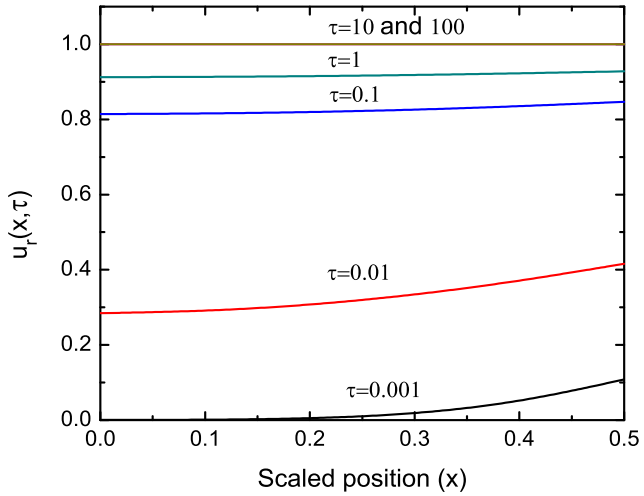

Figure 4.20: Scaled radiation energy density $u_r(x, \tau)$ Vs. position (x) in a sphere of scaled radius X= 0.5.

energy densities in terms of series solutions are found to converge quickly and depending on the required degree of accuracy, the number of poles to be considered is decided.

4.3.3 Sphere

The scaled radiation and material energy densities for a sphere of scaled radius x=0.5 are shown in figures 4.20 and 4.21. Both the scaled radiation and material energy densities attain a steady state value of 1 implying that the sphere finally attains the temperature of the incident radiation as expected. The material energy density lags behind the radiation energy density as usual and the results are found to be consistent.

4.4 Summary

In this chapter, the time dependent non equilibrium radiation diffusion problem has been solved analytically for finite planar slab, spherical shell and sphere with a constant radiation flux inci-

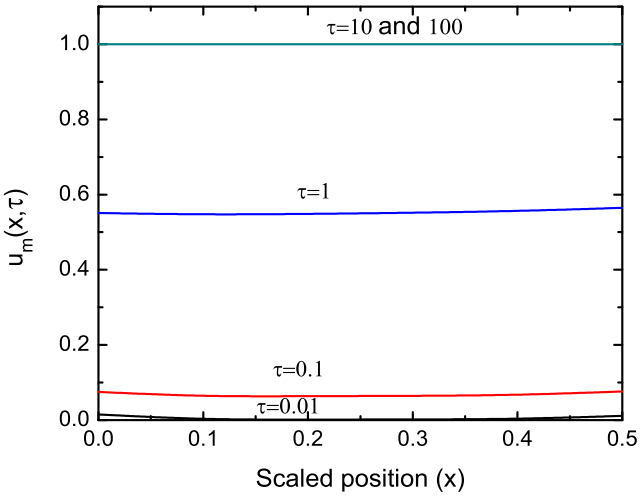

Figure 4.21: Scaled material energy density $u_r(x, \tau)$ Vs. position (x) in a sphere of scaled radius X= 0.5.

dent on the surface. The observed trend in temporal and spatial variation of energy densities, leakage currents, integral quantities, etc. has been explained physically. The results obtained in this work can serve as new and useful benchmarks for non equilibrium radiation diffusion codes in both planar and spherical geometries. The same methodology can be applied to any other finite size systems like layered media with various boundary conditions.

5 One dimensional hydrodynamic, radiation diffusion and transport simulation

5.1 Introduction

The zero dimensional model is successful in obtaining the proper reaction yields and reaction dynamics going on in time. However, to study more complex processes like shock propagation in ICF plasmas, pellet implosion and explosion either in a direct drive fusion or via x-rays in a hohlraum for the indirect drive, the actual spatial variation is to be considered. Thus, to have a better understanding of the processes taking place in a thermonuclear plasma, at least one dimensional hydrodynamic simulation study need to be performed. In this chapter, we develop a fully implicit one dimensional hydrodynamic code in the Lagrangian geometry for planar, cylindrical and spherical cases. We validate the code in planar geometry using the benchmark results of shock tube problem [15] and in spherical geometry using Sedov's point explosion problem [16]. Results for Noh's problem have also been generated in both spherical and cylindrical geometries [17].

As the temperature of a material increases, the radiation energy keeps on increasing at a rate greater than the material energy [4]. At high temperatures, the internal energy of the material changes because of radiation interaction in addition to that due to hydrodynamic compression. To obtain the energy flowing from radiation to matter, the radiation transport equation needs

to be solved. We develop a finite difference radiation diffusion code and generate results for the finite and infinite planar slabs and also a finite spherical shell. Radiation transport equation has also been solved numerically using the discrete ordinates method and results generated for Marshak wave propagation in both planar and spherical geometries. As the hydrodynamic motion is slow compared to radiation diffusion or transport, the material is assumed to be static while solving the radiation intensity within the medium.

5.2 Implicit finite difference scheme for solving the hydrodynamic equations

5.2.0.1 Grid structure

For hydrodynamic calculations using a Lagrangian grid, the medium is divided into a number of cells as shown in figure 5.1. The coordinate of the i th vertex is denoted by r_i and the region between the $(i-1)^{th}$ and i^{th} vertices is the i^{th} cell. The density of the i^{th} grid is ρ_i and its mass is given by

$$m_i = \acute{c} \times \rho_i \times (r_i^{\delta} - r_{i-1}^{\delta}), \tag{5.1}$$

with $\acute{c} = 1, \pi, (4/3) \times \pi$ and $\delta = 1, 2, 3$ for planar, cylindrical and spherical geometries respectively. Velocity of the i^{th} vertex is denoted by u_i and $P_i, V_i, T_{ion,i}, T_{elec,i}, E_{ion,i}$ and $E_{elec,i}$ are the total pressure, specific volume, temperature and the specific internal energy of ions and electrons in the i^{th} mesh respectively.

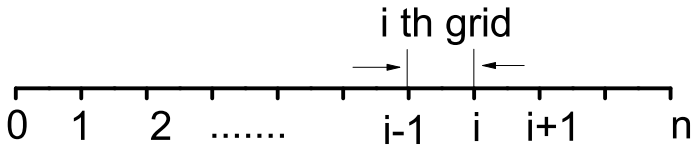

Figure 5.1: Grid structure.

5.2.0.2 Lagrangian step

During a time interval Δt, the vertices r_i of the cells move as (with an error in position $O(\Delta t)^2$)

$$\tilde{r_i} = r_i + u_i^\star \Delta t, \tag{5.2}$$

$$u_i^\star = (1/2)(u_i + \tilde{u}_i), \tag{5.3}$$

where $u_i^\star$ is the average of velocity values at the beginning and end of the Lagrangian step, u_i and $\tilde{u}_i$, respectively.

5.2.0.3 Discretized form of the hydrodynamic equations

In the Lagrangian formulation of hydrodynamics, the mass of each cell remains constant thereby enforcing mass conservation.

The Lagrangian differential equation for the conservation of momentum is :

$$\rho \frac{d\vec{u}}{dt} = -\vec{\nabla} P. \tag{5.4}$$

Here, the total pressure is the sum of the electron and ion pressures i.e. $P = P_{ion} + P_{elec}$.

In ICF plasmas, the Debye length is much less than the electron mean free path so that

there is no charge separation over the length scale of interest [3]. This allows us to assume that electron fluid and ion fluid charge densities and velocities are equal. Thus the plasma behaves as a single fluid though the ions and electrons posses different temperatures.

Eqn. [5.4] can be discretized, for the velocity $\tilde{u}_i$ at the end of the time step, in terms of the pressures $P_i^{1/2}$and $P_{i+1}^{1/2}$ in the i^{th} and $(i+1)^{th}$ meshes after half time step [74]:

$$\tilde{u}_i = u_i - \frac{(P_{i+1}^{1/2} - P_i^{1/2})\Delta t}{\rho_{i+1}(r_{i+1/2} - r_i) + \rho_i(r_i - r_{i-1/2})}. \tag{5.5}$$

The velocity in the i^{th} mesh $\tilde{u}_i$ is determined by the pressure in the i^{th} and $(i+1)^{th}$ meshes and hence all the meshes are connected. Mass conservation equation can be used to eliminate the pressures at half time step to obtain an equation relating the present time step velocities in the adjacent meshes as follows:

The equation describing conservation of mass is

$$\frac{d\rho}{dt} = -\rho(\vec{\nabla}.\vec{u}), \tag{5.6}$$

where ρ is the mass density of the medium. This equation can be rewritten in terms of pressure using the relation, $\frac{dP}{dt} = \left(\frac{dP}{d\rho}\right)_S \frac{d\rho}{dt} = c_s^2 \frac{d\rho}{dt}$ where $c_s = \sqrt{\left(\frac{dP}{d\rho}\right)_S}$ is the adiabatic sound speed. Therefore, eqn. [5.6] becomes

$$\frac{dP}{dt} = -c_s^2 \rho \vec{\nabla}.\vec{u}. \tag{5.7}$$

This can be written for all the one dimensional co-ordinate systems as

$$\frac{dP}{dt} = -c_s^2 \rho \frac{1}{r^\alpha} \frac{d}{dr} r^\alpha u, \tag{5.8}$$

where $\alpha = 0, 1, 2$ for planar, cylindrical and spherical geometries. This equation can be dis-

cretized to obtain the change in total pressure along a Lagrangian trajectory in terms of the velocity $\tilde{u}_i$ at the end of the time step [74]:

$$P_i^{1/2} = P_i + q_i - \rho_i c_{s,i}^2 \frac{1}{r_{i-1/2}^{\alpha}} \times [\frac{r_i^{\alpha}\tilde{u}_i - r_{i-1}^{\alpha}\tilde{u}_{i-1}}{r_i - r_{i-1}}]\frac{\Delta t}{2}, \tag{5.9}$$

and

$$P_{i+1}^{1/2} = P_{i+1} + q_{i+1} - \rho_{i+1} c_{s,i+1}^2 \frac{1}{r_{i+1/2}^{\alpha}} \times [\frac{r_{i+1}^{\alpha}\tilde{u}_{i+1} - r_i^{\alpha}\tilde{u}_i}{r_{i+1} - r_i}]\frac{\Delta t}{2}. \tag{5.10}$$

Here, q_i is the quadratic Von Neumann and Richtmyer artificial viscosity in the i^{th} mesh [22]:

$$q_i = \frac{\acute{k}(\rho_i \Delta x_i)^2}{V_i}(\frac{dV_i}{dt})^2 \tag{5.11}$$

where $\acute{k}$ ($\simeq 3$) is a dimensionless constant. Using eqns. [5.9] and [5.10] , $P_i^{1/2}$and $P_{i+1}^{1/2}$ in eqn. [5.5] are eliminated to obtain a tridiagonal system of equations for $\tilde{u}_i$:

$$-A_i\tilde{u}_{i+1} + B_i\tilde{u}_i - C_i\tilde{u}_{i-1} = D_i \tag{5.12}$$

where

$$A_i = \frac{\rho_{i+1}(c_{s,i+1}\Delta t)^2}{2(\rho\Delta r)_i} \times \frac{r_{i+1}^{\alpha}}{r_{i+1/2}^{\alpha}(r_{i+1} - r_i)}, \tag{5.13}$$

$$B_i = 1 + \frac{\rho_{i+1}(c_{s,i+1}\Delta t)^2}{2(\rho\Delta r)_i} \times \frac{r_i^{\alpha}}{r_{i+1/2}^{\alpha}(r_{i+1} - r_i)} + \frac{\rho_i(c_{s,i}\Delta t)^2}{2(\rho\Delta r)_i} \times \frac{r_i^{\alpha}}{r_{i-1/2}^{\alpha}(r_i - r_{i-1})}, \tag{5.14}$$

$$C_i = \frac{\rho_i (c_{s,i}\Delta t)^2}{2(\rho\Delta r)_i} \times \frac{r_{i-1}^{\alpha}}{r_{i-1/2}^{\alpha}(r_i - r_{i-1})} \tag{5.15}$$

$$D_i = u_i - \frac{\Delta t}{(\rho\Delta r)_i}[P_{i+1} + q_{i+1} - P_i - q_i], \tag{5.16}$$

with

$$(\rho\Delta r)_i = \rho_{i+1}(r_{i+1/2} - r_i) + \rho_i(r_i - r_{i-1/2}). \tag{5.17}$$

The energy equations, for the ions and electrons, expressed in terms of temperature are

$$\rho[C_{V\,ion}\frac{\partial T_{ion}}{\partial t} + \frac{\partial E_{ion}}{\partial V}\frac{\partial V}{\partial t}] = -\frac{P_{ion}}{V}\frac{\partial V}{\partial t} - P_{ie} \tag{5.18}$$

and

$$\rho[C_{V\,elec}\frac{\partial T_{elec}}{\partial t} + \frac{\partial E_{elec}}{\partial V}\frac{\partial V}{\partial t}] = -\frac{P_{elec}}{V}\frac{\partial V}{\partial t} + P_{ie}. \tag{5.19}$$

where E_{ion} and E_{elec} are the specific internal energies and V is specific volume. P_{ie} is the ion-electron energy exchange term given by

$$P_{ie}(\mathrm{Tergs/cm^3/\mu s}) = 2.704 \times 10^{-40} n_{elec}\, n_{ion} \times \frac{T_{ion} - T_{elec}}{T_{elec}^{1.5}} M^{-1} Z^2 \times \ln\Lambda, \tag{5.20}$$

with ion and electron temperatures expressed in keV. Further, 'n_{elec}' and 'n_{ion}' are the number densities of electrons and ions, M is the mass number and Z is the charge of the ions. Here the Coulomb logarithm for ion-electron collision is [90]

$$\ln\Lambda = \max\{1,\ (23 - \ln[(n_{elec})^{0.5} Z\, T_{elec}^{-1.5}])\} \tag{5.21}$$

with T_{elec} expressed in eV. The discrete form of the energy equations for ions and electrons are

$$T_{ion,i}^{n,k} = T_{ion,i}^{n-1} - (P_{ion,i}^{n,k-1}\ \Delta V_i^{n,k} + \frac{P_{ie}^{n,k-1}\Delta t}{\rho_i^{n,k-1}} + \delta_{ion}^{n,k-1}\Delta V_i^{n,k})/C_{Vion,i}^{n,k-1} \tag{5.22}$$

and

$$\begin{aligned} T_{elec,i}^{n,k} &= T_{elec,i}^{n,k-1} + \frac{\rho_i^{n,k-1}C_{Velec,i}^{n,k-1}(T_{elec,i}^{n-1} - T_{elec,i}^{n,k-1})}{\Delta t H_i^{n,k-1}} \\ &- \frac{(P_{elec}^{n,k-1} + \delta_{elec}^{n,k-1})\rho_i^{n,k-1}\Delta V_i^{n,k}}{\Delta t H_i^{n,k-1}} + P_{ie}^{n,k-1}/H_i^{n,k-1} \end{aligned} \tag{5.23}$$

where

$$H_i^{n,k-1} = \frac{\rho_i^{n,k}C_{Velec,i}^{n,k-1}}{\Delta t_n}, \tag{5.24}$$

$$\delta_{ion}^{n,k-1} = (\frac{\partial E_{ion}}{\partial V})_i^{n,k-1}, \tag{5.25}$$

$$\delta_{elec}^{n,k-1} = (\frac{\partial E_{elec}}{\partial V})_i^{n,k-1}. \tag{5.26}$$

$$\tag{5.27}$$

with ‘n’ and ‘k’ denoting the time step and iteration index respectively.

5.2.1 Results

We have investigated the performance of the scheme using the following benchmark problems:

Shock tube problem

The shock tube is the most convenient and widely used tool for obtaining high temperatures in the laboratory and for studying the chemical physics of gases. It is essentially a device in which a plane shock wave is produced by the sudden bursting of a diaphragm which separates a gas at high pressure from one at lower pressure [15]. After the bursting of the diaphragm a compression wave is formed in the low pressure gas, this rapidly steepening to form a shock

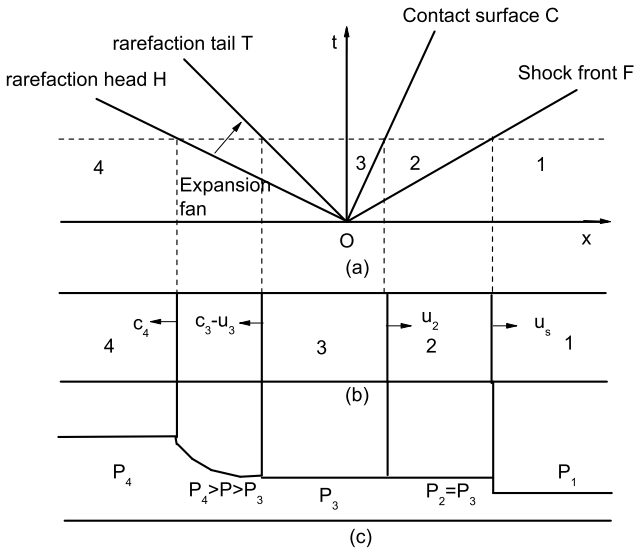

Figure 5.2: (a) The (x,t) diagram in a shock tube. (b) Velocities of the fronts relative to the shock tube and (c) Illustrative pressure profiles at time t.

front. Simultaneously, an expansion or rarefaction wave moves back into the high-pressure gas with sound speed where the pressure fall is smooth. Figure 5.2 (a) is an (x,t) diagram for a shock wave in a tube in which the driver gas at high pressure P_4 in the region 4 is being expanded through the expansion fan to a lower pressure P_3 behind the contact surface in the region 3. The limits of the expansion fan are formed by the head and tail of the rarefaction wave. Region 2 denotes the region between the shock front and contact surface whereas the region 1 is undisturbed low pressure region. At a time t following this event the velocities of the fronts relative to the shock tube are shown in figure 5.2 (b), while the pressure profiles are shown in figure 5.2 (c).

It is convenient to consider the gas motion in relation to the shock front and hence we consider the equations for conservation of mass, momentum and energy in terms of velocity v

measured in shock-fixed coordinates.

$$\rho_2 v_2 = \rho_1 v_1 = m, \tag{5.28}$$

$$P_2 + \rho_2 v_2^2 = P_1 + \rho_1 v_1^2, \tag{5.29}$$

$$\rho_2 v_2 (H_2 + \frac{1}{2} v_2^2) = \rho_1 v_1 (H_1 + \frac{1}{2} v_1^2), \tag{5.30}$$

$$v_1 = u_s - u_1, v_2 = u_s - u_2. \tag{5.31}$$

where H is the enthalpy per unit mass, u_s is the shock velocity relative to the tube, ρ is the density and u is the particle velocity relative to the shock tube. For an ideal gas the enthalpy H is given by

$$H = E + \frac{P}{\rho} = \frac{c^2}{\gamma_1 - 1}, \tag{5.32}$$

$$E = \frac{P}{\rho(\gamma_1 - 1)}, c = \sqrt{\frac{\gamma_1 P}{\rho}} \tag{5.33}$$

where E is the specific internal energy, c is the local sound speed and γ is the specific heat ratio. The shock strength is defined as the fractional change in pressure due to shock compression, i.e., $s = (P_2 - P_1)/P_1$ so that eqns. (5.28)-(5.31) can be explicitly written as

$$P_2 = P_1(1 + s), \tag{5.34}$$

$$\rho_2 = \rho_1 \frac{1 + g^+ s}{1 + g^- s}, \tag{5.35}$$

$$c_2 = c_1 \sqrt{\frac{(1 + s)(1 + g^- s)}{1 + g^+ s}}, \tag{5.36}$$

$$u_s = u_1 + c_1 \sqrt{1 + g^+ s}, \tag{5.37}$$

$$u_2 = u_1 + c_1 \frac{s}{\gamma_1 \sqrt{1 + g^+ s}}, \tag{5.38}$$

$$g^\pm = \frac{\gamma_1 \pm 1}{2\gamma_1}. \tag{5.39}$$

where it has been assumed that γ_1 remains unchanged even after the shock compression. At contact discontinuity which separates regions 2 and 3, the mass flux is zero. Hence,

$$P_3 = P_2, u_3 = u_2 = u_c, \tag{5.40}$$

where u_c is the speed of the contact discontinuity. It moves with the same velocity as the two gases on either side of it. Behind CD, a trailing fan of rarefaction wave moves towards left with the head of the RW fan moving with velocity $c_4 - u_4 = c_4$ towards left, whereas the tail end moves with velocity $c_3 - u_3$. Inside the fan region, the expansion occurs isentropically such that $u + \frac{2c}{\gamma - 1}$ is conserved. Thus,

$$\begin{aligned} u_3 + \frac{2c_3}{\gamma_4 - 1} &= u_4 + \frac{2c_4}{\gamma_4 - 1} \\ \text{i.e., } c_3 &= c_4 - \frac{\gamma_4 - 1}{2} u_3. \end{aligned} \tag{5.41}$$

Having known c_3, we can write P_3 and ρ_3 using adiabatic relation $P_3 \propto \rho_3^{\gamma_4}$ and sound speed $c_3^2 = \frac{\gamma_4 P_3}{\rho_3}$.

$$P_3 = P_4 (\frac{c_3}{c_4})^{1/a}, \rho_3 = \rho_4 (\frac{P_3}{P_4})^{1/\gamma_4}, a = \frac{\gamma_4 - 1}{2\gamma_4}. \tag{5.42}$$

assuming that γ_4 remains unchanged even after rarefaction. The self-similar solution inside the RW fan region can be written as

$$c = \frac{\gamma_4 - 1}{\gamma_4 + 1} \frac{z}{t} + \frac{2}{\gamma_4 + 1} c_4, \tag{5.43}$$

$$P = P_4 (\frac{c}{c_4})^{1/a}, \rho = \rho_4 (\frac{P}{P_4})^{1/\gamma_4}, \tag{5.44}$$

$$u = u_4 + 2\frac{c_4 - c}{\gamma_4 - 1}. \tag{5.45}$$

Assuming the lower pressure gas also to be at rest at t=0, the shock strength s can be obtained

by solving the following algebraic equation:

$$F(s) = 1 - \frac{bs}{\sqrt{1+g^{+}s}} - p(1+s)^{a} = 0, \tag{5.46}$$

$$b = \frac{c_1(\gamma_4 - 1)}{2c_4\gamma_1}, p = (\frac{P_1}{P_4})^{a}. \tag{5.47}$$

The axial distance is obtained by the product of the velocities in the respective regions and the given time t. For verifying the results obtained from our code with the analytical results, we consider ideal gas of D-T with specific heat ratio 5/3 filled within a tube of length 20 cm. At time t=0, the diaphragm is at the centre of the tube i.e., at x=10 cm. On the left side of the diaphragm, the driver gas is at a density of 1 gm/cc and pressure 0.12 Mbar. The test gas on the right is at a pressure of 0.012 Mbar and density 0.1 gm/cc. The internal energy of both sides is 0.18 Tergs/gm. The tube is divided into 200 meshes each of thickness 0.1 cm. Figure 5.3 shows the density, pressure, velocity and internal energy as a function of distance at a time 10μs. Comparison with the analytical results (solid lines) is also shown.

Sedov's self similar point explosion problem

The self similar problem of a strong point explosion was formulated and solved by Sedov [16]. The problem considers a perfect gas with constant specific heats and density ρ_0 in which a large amount of energy E is liberated at a point instantaneously. The shock wave propagates through the gas starting from the point where the energy is released. For numerical simulation, the energy E is assumed to be liberated in the first two meshes. The process is considered at a larger time t when the radius of the shock front $R(t) >> r_0$, the radius of the region in which energy is released. It is also assumed that the stage of the process is sufficiently early so that the shock wave has not moved too far from the source. This ascertains that the shock strength is sufficiently large and it is possible to neglect the initial gas pressure P_0 or counter pressure in comparison with the pressure behind the shock wave [4].

Under the above assumptions, the gas motion is determined by four independent variables,

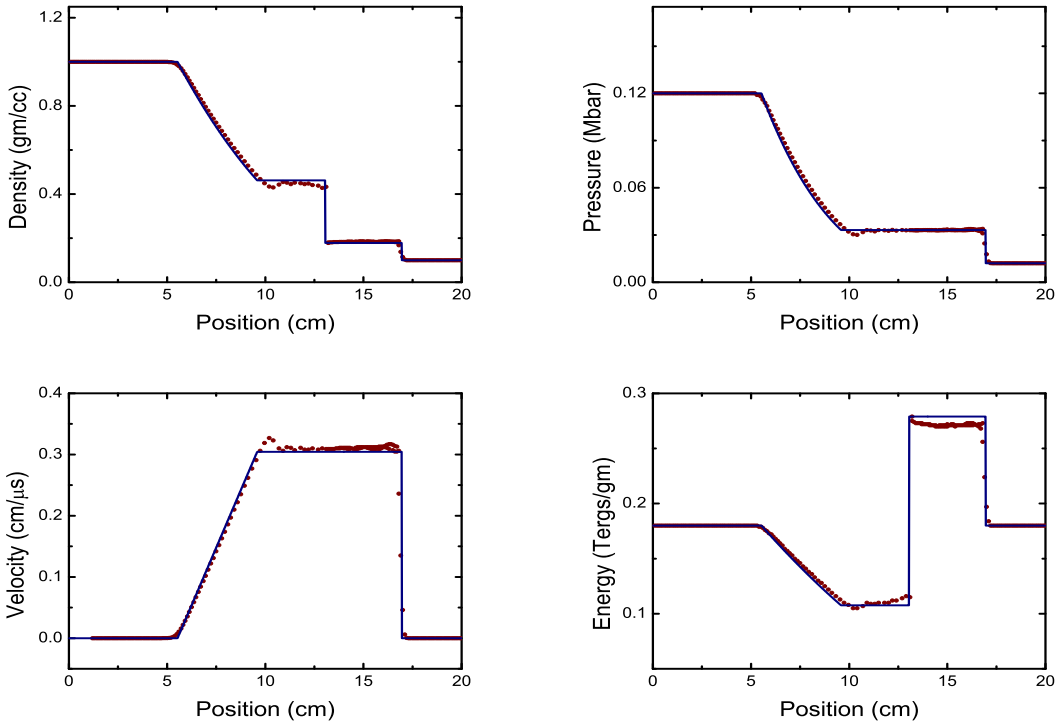

Figure 5.3: Comparison of the variables obtained from the simulation data in the pure hydrodynamic case (points) with the analytical solutions (lines) for the shock tube problem.

viz, amount of energy released E, initial uniform density ρ_0, distance from the centre of the explosion r and time t. The dimensionless quantity $\xi = r/R$ serves as the similarity variable. The motion of the wavefront R(t) is governed by the relationship

$$R = \xi_0 (\frac{E}{\rho_0})^{1/5} t^{2/5}, \tag{5.48}$$

where ξ_0 is an independent variable. The propagation velocity of the shock wave is

$$u_s = \frac{2}{5} \xi_0^{5/2} (\frac{E}{\rho_0})^{1/2} R^{-3/2}. \tag{5.49}$$

The parameters behind the shock front using the limiting formulas for a strong shock wave are

$$u_1 = \frac{2}{\gamma + 1} u_s, \tag{5.50}$$

$$P_1 = \frac{2}{\gamma + 1} \rho_0 u_s^2, \tag{5.51}$$

$$\rho_1 = \rho_0 \frac{\gamma + 1}{\gamma - 1}, \tag{5.52}$$

$$T_1 = \frac{P_1}{(\gamma - 1)\rho_1 C_V}. \tag{5.53}$$

where C_V is the specific heat at constant volume and $\gamma = C_P/C_V$ is the ratio of specific heats. The distributions of velocity, pressure and density w.r.t. the radius are determined as functions of the dimensionless variable $\xi = r/R$. Since the motion is self-similar, the solution can be expressed in the form

$$u = u_1(t)\tilde{u}(\xi), \;\; P = P_1(t)\tilde{P}(\xi), \;\; \rho = \rho_1 \tilde{\rho}(\xi), \tag{5.54}$$

where $\tilde{u}, \tilde{P}$ and $\tilde{\rho}$ are new dimensionless functions. The hydrodynamic equations, which are a

system of three PDE's, are transformed into a system of three ordinary first-order differential equations for the three unknown functions $\tilde{u}, \tilde{P}$ and $\tilde{\rho}$ by substituting the expressions given by eqn. [5.54] into the hydrodynamic equations for the spherically symmetric case and transforming from r and t to ξ. The boundary condition satisfied by the solution at the shock front ($r = R$ or $\xi = 1$) is $\tilde{u} = \tilde{P} = \tilde{\rho} = 1$. The dimensionless parameter ξ_0, which depends on the specific heat ratio γ is obtained from the condition of conservation of energy evaluated with the solution obtained. Also, the distributions of velocity, pressure, density and temperature behind the shock front are generated numerically using the hydrodynamics code without taking radiation interaction into account. Ideal D-T gas of density $\rho_0 = 1\ \mathrm{gm/cc}$ and $\gamma = 1.4$ is filled inside a sphere of 1 cm radius with the region divided into 100 radial meshes each of width 0.01 cm. The initial internal energy per unit mass is chosen as $10^5\ \mathrm{Tergs/gm}$ for the first two meshes and zero for all the other meshes. An initial time step of $10^{-6}\ \mu s$ is chosen and the thermodynamic variables are obtained after a time $0.2\ \mu s$. As in the case of the problem of shock propagation in aluminum, the total energy equation is solved assuming that electrons and ions are at the same temperature (the material temperature). In figure 5.4. we compare the distribution of the functions $P/P_1, u/u_1, \rho/\rho_1$ and T/T_1 with respect to r/R obtained exactly by solving the ODEs as explained above (solid lines) with the results generated from our code (dots). Good agreement between the numerical and theoretical results is observed. As is characteristic of a strong explosion, the gas density decreases extremely rapidly as we move away from the shock front as seen from figure 5.4. In the vicinity of the front the pressure decreases as we move towards the centre by a factor of 2 to 3 and then remains constant whereas the velocity curve rapidly becomes a straight line passing through the origin. The temperatures are very high at the centre and decreases smoothly at the shock front. As the particles at the centre are heated by a strong shock, they have very high entropy and hence high temperatures.

Noh's problem

Noh's problem in spherical and cylindrical coordinates consists of a sphere or cylinder of

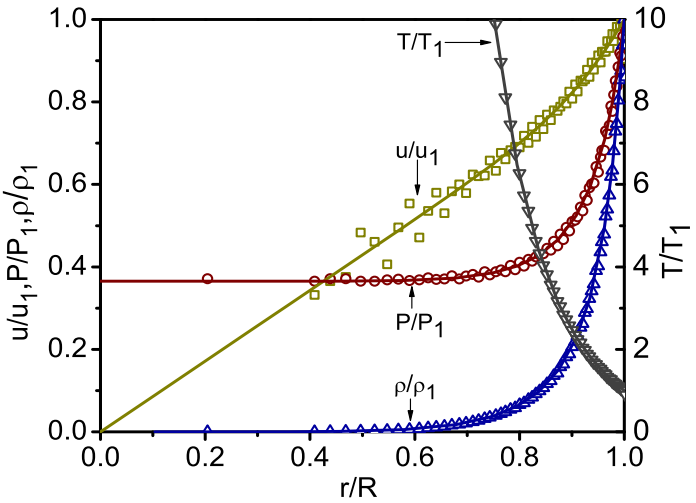

Figure 5.4: Comparison of the scaled variables obtained from the simulation data in the pure hydrodynamic case (points) with the self similar solutions (lines) for the point explosion problem. Specific internal energy $E = 10^5$ Tergs/gm is deposited in the inner two meshes and $\gamma = 1.4$.

uniform density ρ_0 and radius r_0 initially. At t=0, all the interior points start moving radially towards the centre with a given uniform velocity u_0. The hydrodynamic equations governing an isentropic flow in one dimension is given by

$$\frac{\partial \rho}{\partial t} + u\frac{\partial \rho}{\partial r} + \rho(\frac{\partial u}{\partial r} + \frac{Nu}{r}) = 0, \tag{5.55}$$

$$\rho(\frac{\partial u}{\partial t} + u\frac{\partial u}{\partial r}) + \frac{\partial P}{\partial r} = 0, \tag{5.56}$$

$$\frac{\partial S}{\partial t} + u\frac{\partial S}{\partial r} = 0, \tag{5.57}$$

where $\rho(r,t), P(r,t), u(r,t)$ and $S(r,t)$ are respectively, the density, pressure, velocity and entropy of the medium at point r at time t. N = 0, 1 and 2 for planar, cylindrical and spherical geometry. In eqn. [5.57], the flow has been assumed to be inviscid and nonconducting so that the entropy remains constant along the moving trajectory of a fluid element. The problem was solved analytically by W. F. Noh for an ideal gas and for a more general equation of state by

Roy A. Axford using LIE group transformation [17, 100].

At time t=0, all the points move radially towards the centre and immediately a shock wave is reflected from the centre for $t > 0$. This shock wave continues moving outwards compressing the medium behind it. Thus, at any instant of time t, the whole region is divided into two zones, the shocked zone and the unshocked zone. The spatial profiles of the flow variables at any instant of time are

$$\rho_1 = \rho_0(\frac{\gamma+1}{\gamma-1})^{N+1}, \tag{5.58}$$

$$P_1 = -u_0 u_s \rho_1, \tag{5.59}$$

$$E_1 = \frac{-u_0 u_s}{\gamma-1}, \tag{5.60}$$

$$u_1 = 0, \tag{5.61}$$

$$u_s = -\frac{u_0(\gamma-1)}{2}, \tag{5.62}$$

behind the shock front. At the shock front, the values are:

$$\rho_s = \rho_0(\frac{\gamma+1}{\gamma-1})^{N+1}, \tag{5.63}$$

$$P_s = 0, \tag{5.64}$$

$$E_s = 0, \tag{5.65}$$

$$u_s = u_0. \tag{5.66}$$

And ahead of the shock front,

$$\rho(r,t) = \rho_0(1 - \frac{u_0 t}{r})^N, \tag{5.67}$$

$$P_0 = 0, \tag{5.68}$$

$$E_0 = 0, \tag{5.69}$$

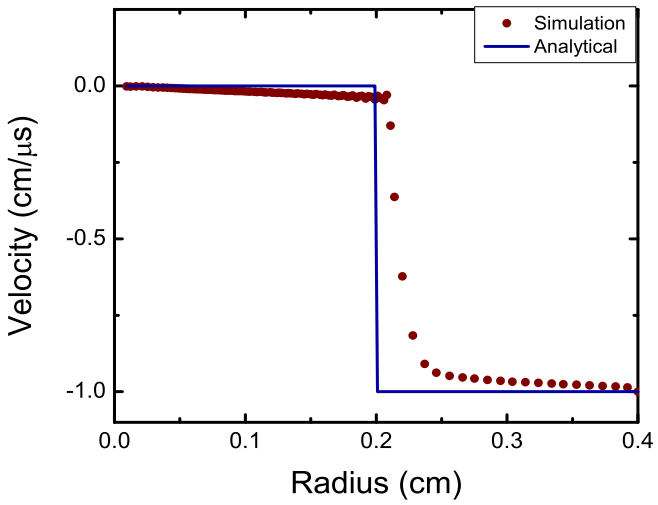

a)

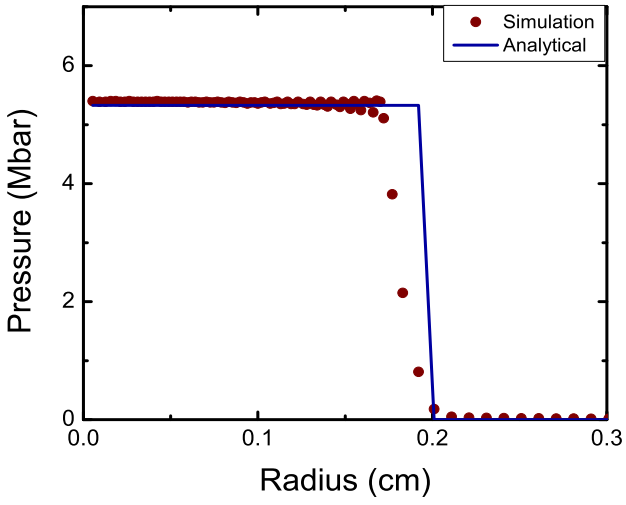

b)

Figure 5.5: Comparison of a) the velocities from the simulation data with the analytical solutions for the Noh problem in spherical geometry and b) the pressures in cylindrical geometry at time $t = 0.6$ μsec.

for a given u_0. The uniform velocity u_0 with which the points move towards the centre is taken to be $1\ \mathrm{cm}/\mu\mathrm{sec}$ i.e., $u_0 = 1\ \mathrm{cm}/\mu\mathrm{sec}$, initial density $\rho_0 = 1\ \mathrm{gm/cc}$ and $\gamma = 5/3$. Then the velocity $u_s = 1/3\ \mathrm{cm}/\mu\mathrm{sec}$, so that at $t = 0.6\ \mu\mathrm{sec}$, the shock front appears at r=0.2 cm. Using the fully implicit hydrodynamic code, the spatial profiles of the flow variables are obtained at $t = 0.6\ \mu\mathrm{sec}$ with 100 meshes each having a width of 0.01cm. The spatial velocity profile for a sphere and spatial temperature profile for a cylinder as obtained from the simulation as well as the analytical values are plotted in figure 5.5.

5.3 Finite difference method for solving the radiation diffusion equation

In this section, we present the finite difference solution to the radiation diffusion equation coupled to the material energy equation defined in the previous chapter. As the radiation diffusion is faster than hydrodynamic motion, the medium is assumed to remain static during the time required to attain the steady state.

Planar slab

We assume that the opacity is temperature independent and the heat capacity is proportional to the cube of the temperature, $C_V = \alpha T^3(z,t)$. Then, for a material energy density $\theta = aT^4(z,t)$ and radiation flux $F(z,t) = -\frac{c}{3\sigma_a}\frac{\partial E_r(z,t)}{\partial z}$, the radiation and material energy density equations along with the boundary conditions for a finite slab of thickness l are

$$\frac{\partial E_r(z,t)}{\partial t} + \frac{\partial F(z,t)}{\partial z} = c\sigma_a(\theta(z,t) - E_r(z,t)), \tag{5.70}$$

$$\frac{1}{c}\frac{\partial \theta(z,t)}{\partial t} = \epsilon\sigma_a(E_r(z,t) - \theta(z,t)), \tag{5.71}$$

$$cE_r(0,t) + 2F(0,t) = 4F_{inc}, \tag{5.72}$$

$$cE_r(l,t) - 2F(l,t) = 0. \tag{5.73}$$

Time differencing is performed using a fully implicit backward Euler scheme. Spatial discretization is performed on a staggered mesh where the independent spatial variable z and the flux F are evaluated at cell edges and the energy densities represent cell averages at the cell centers. The finite difference equations for the radiation and material energy densities are obtained as [64]

$$(1+\frac{\sigma_a}{\gamma_a+\epsilon\sigma_a})\gamma_a E_{r,i}^{n+1}+\frac{1}{c\Delta z_i}(F_{i+1/2}^{n+1}-F_{i-1/2}^{n+1})=\gamma_a E_{r,i}^{n}+\frac{\sigma_a\gamma_a}{\gamma_a+\epsilon\sigma_a}\theta_i^n, \tag{5.74}$$

$$\theta_i^{n+1}=\frac{\gamma_a}{\gamma_a+\epsilon\sigma_a}\theta_i^n+\frac{\epsilon\sigma_a}{\gamma_a+\epsilon\sigma_a}E_{r,i}^{n+1}, \tag{5.75}$$

where $\gamma_a=1/(c\Delta t)$ and $\Delta z_i=z_{i+1/2}-z_{i-1/2}$. The energy density is assumed to be a piecewise linear function in space and we define two fluxes at the cell edge, one from the left and one from the right.

$$F_{l,i+1/2}^{n+1}=-\frac{2c}{3\sigma_a}\frac{E_{r,i+1/2}^{n+1}-E_{r,i}^{n+1}}{\Delta z_i}, \tag{5.76}$$

$$F_{r,i+1/2}^{n+1}=-\frac{2c}{3\sigma_a}\frac{E_{r,i+1}^{n+1}-E_{r,i+1/2}^{n+1}}{\Delta z_{i+1}}. \tag{5.77}$$

The edge value of the radiation energy density is a weighted average of the cell center quantities. Finally a tridiagonal system of equations is obtained for the radiation energy density at time n+1 as

$$\begin{aligned}-E_{r,i-1}^{n+1}+[1+\frac{\Delta z_{i-1/2}}{\Delta z_{i+1/2}}+3\sigma_a\Delta z_i\Delta z_{i-1/2}\gamma_a(1+\sigma_a/(\gamma_a+\epsilon\sigma_a))]E_{r,i}^{n+1}\\ -\frac{\Delta z_{i-1/2}}{\Delta z_{i+1/2}}E_{r,i+1}^{n+1}=3\sigma_a\Delta z_i\Delta z_{i-1/2}\gamma_a E_{r,i}^{n}+\frac{3\sigma_a^2\Delta z_i\Delta z_{i-1/2}\gamma_a}{\gamma_a+\epsilon\sigma_a}\theta_i^n,\end{aligned} \tag{5.78}$$

where $\Delta z_{i+1/2}=\frac{1}{2}(\Delta z_i+\Delta z_{i+1})$. Applying the BCs for the first and last cell, the radiation

energy density equations for the first cell is

$$[1+2(\frac{\Delta z_1}{\Delta z_{3/2}}+\frac{4}{3\sigma_a\Delta z_{3/2}})^{-1}+3\sigma_a\Delta z_1\Delta z_{3/2}\gamma_a(1+\frac{\sigma_a}{\gamma_a+\epsilon\sigma_a})]E_{r,1}^{n+1}-E_{r,2}^{n+1}$$
$$=3\sigma_a\Delta z_1\Delta z_{3/2}\gamma_a(E_{r,1}^n+\frac{\sigma_a}{\gamma_a+\epsilon\sigma_a}\theta_1^n)+\frac{8}{c}F_{inc}(\frac{\Delta z_1}{\Delta z_{3/2}}+\frac{4}{3\sigma_a\Delta z_{3/2}})^{-1}. \quad (5.79)$$

And that for the last cell is

$$[1+(\frac{\Delta z_N}{2\Delta z_{N-1/2}}+\frac{2}{3\sigma_a\Delta z_{N-1/2}})^{-1}+3\sigma_a\Delta z_N\Delta z_{N-1/2}\gamma_a(1+\frac{\sigma_a}{\gamma_a+\epsilon\sigma_a})]E_{r,N}^{n+1}$$
$$-E_{r,N-1}^{n+1}=3\sigma_a\Delta z_N\Delta z_{N-1/2}\gamma_a(E_{r,N}^n+\frac{\sigma_a}{\gamma_a+\epsilon\sigma_a}\theta_N^n). \quad (5.80)$$

Spherical shell

In this section, we derive the finite difference equations for obtaining the radiation and material energy densities for a spherical shell of inner radius R_1 and outer radius R_2. Using the transformation $E_r'(r,t)=E_r(r,t)r$ and $\theta'=aT^4(r,t)r$, the flux is defined as $F(r,t)=-\frac{c}{3\sigma_a}\frac{\partial E_r'(r,t)}{\partial r}$. Then the equations for transformed radiation and material energy densities and the boundary conditions are

$$\frac{\partial E_r'(r,t)}{\partial t}+\frac{\partial F(r,t)}{\partial r}=c\sigma_a(\theta'(r,t)-E_r'(r,t)), \quad (5.81)$$
$$\frac{1}{c}\frac{\partial\theta'(r,t)}{\partial t}=\epsilon\sigma_a(E_r'(r,t)-\theta'(r,t)), \quad (5.82)$$
$$(\frac{1}{R_1}+\frac{2}{3\sigma_aR_1^2})E_r'(R_1,t)+\frac{2}{c}\frac{F(R_1,t)}{R_1}=\frac{4F_{inc}}{c}, \quad (5.83)$$
$$(\frac{1}{R_2}-\frac{2}{3\sigma_aR_2^2})E_r'(R_1,t)-\frac{2}{c}\frac{F(R_2,t)}{R_2}=0. \quad (5.84)$$

Using finite differencing in space and time as done for the plane slab, the tridiagonal equation

for energy density (in terms of the transformed variables E'_r and θ') of the inner cells is

$$-E'^{n+1}_{r,i-1} + [1 + \frac{\Delta r_{i-1/2}}{\Delta r_{i+1/2}} + 3\sigma_a \Delta r_i \Delta r_{i-1/2}\gamma_a(1 + \frac{\sigma_a}{\gamma_a + \epsilon\sigma_a})]E'^{n+1}_{r,i}$$
$$-\frac{\Delta r_{i-1/2}}{\Delta r_{i+1/2}}E'^{n+1}_{r,i+1} = 3\sigma_a \Delta r_i \Delta r_{i-1/2}\gamma_a E'^{n}_{r,i} + \frac{3\sigma_a^2 \Delta r_i \Delta r_{i-1/2}\gamma_a}{\gamma_a + \epsilon\sigma_a}\theta'^{n}_i. \quad (5.85)$$

From the BC on the surface of the first and last cell, we obtain the equation relating the energy densities for the first cell as

$$[1 + 2\frac{(2 + 3\sigma_a R_1)\Delta r_{3/2}}{4R_1 + 3\sigma_a R_1 \Delta r_1 + 2\Delta r_1} + 3\sigma_a \Delta r_1 \Delta r_{3/2}\gamma_a(1 + \frac{\sigma_a}{\gamma_a + \epsilon\sigma_a})]E'^{n+1}_{r,1} - E'^{n+1}_{r,2}$$
$$= 3\sigma_a \Delta r_1 \Delta r_{3/2}\gamma_a(E'^{n}_{r,1} + \frac{\sigma_a \theta'^{n}_1}{\gamma_a + \epsilon\sigma_a}) + \frac{24F_{inc}}{c}\frac{1}{\frac{4}{R_1\sigma_a\Delta r_{3/2}} + \frac{3\Delta r_1}{\Delta r_{3/2}R_1} + \frac{2\Delta r_1}{R_1^2\sigma_a\Delta r_{3/2}}}]. \quad (5.86)$$

Similarly, the equation for the last cell is

$$[1 + \frac{2\Delta r_{N-1/2}(3\sigma_a R_2 - 2)}{(3\sigma_a R_2 - 2)\Delta r_N + 4R_2} + 3\sigma_a \Delta r_N \Delta r_{N-1/2}\gamma(1 + \frac{\sigma_a}{\gamma_a + \epsilon\sigma_a})]E'^{n+1}_{r,N}$$
$$-E'^{n+1}_{r,N-1} = 3\sigma_a \Delta r_\Delta r_{N-1/2}\gamma_a(E'^{n}_{r,N} + \frac{\sigma_a \theta'^{n}_N}{\gamma_a + \epsilon\sigma_a}). \quad (5.87)$$

5.3.1 Results

5.3.1.1 Planar slab

Finite planar slab

The radiation and material energy densities obtained from finite difference analysis are plotted in figures 5.6 and 5.7 along with the analytical results for a slab of width $b = 1$. To obtain a normalized solution that is comparable to analytical solution, we choose $F_{inc} = c/4$, so that E_r and θ directly correspond to u_r and u_m respectively. The numerical results obtained from finite difference analysis are found to converge for a mesh width $\Delta z = 5.7733 \times 10^{-5}$ cm. A time step of $\Delta t = 3.33 \times 10^{-15}$ s is chosen upto a scaled time $\tau = 0.1$. Beyond this time, a coarser

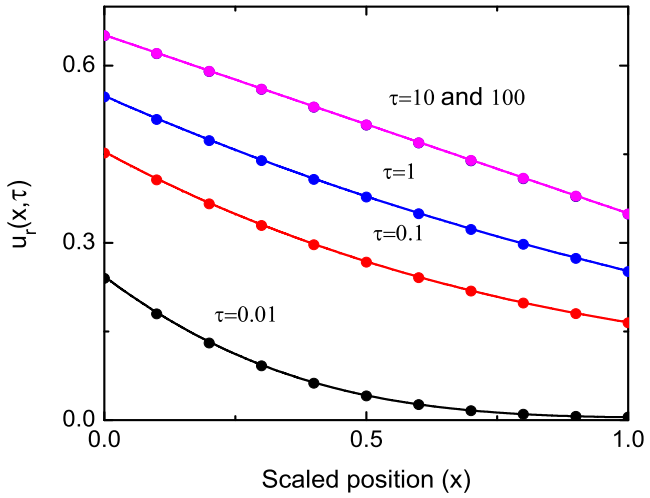

Figure 5.6: Scaled radiation energy density $u_r(x,\tau)$ Vs. position (x) in the slab of scaled thickness b=1 at different times for $\epsilon = 0.1$. The symbols stand for analytical values whereas lines represent the results obtained from finite difference method.

time step of $\Delta t = 3.33 \times 10^{-12}$ s is found to be sufficient for obtaining the converged values. The numerical results are found to agree with the analytical ones with an error $< 1\%$ at early stages ($\tau = 0.01$). The error reduces further as time progresses.

Infinite planar slab

The same finite difference diffusion program for the finite planar slab is used for obtaining the radiation and material energy densities for an infinite slab. The main modification is that the radiation energy density in the last cell is zero, i.e., $E_N^{n+1} = 0$ as radiation can never reach the other end of the infinite slab. In figure 5.8, the scaled material and radiation energy densities have been plotted as a function of the scaled depth $\sigma_a z$ in the slab. The results agree with those obtained by Su and Olson [64] both numerically and semi-analytically.

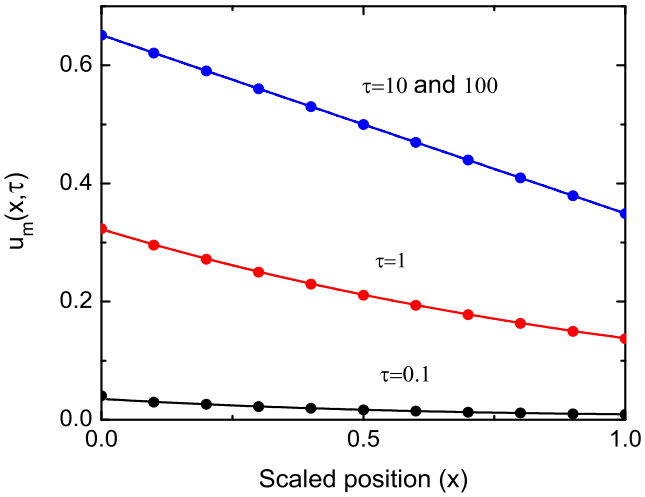

Figure 5.7: Scaled material energy density $u_m(x,\tau)$ Vs. position (x) in the slab at different times for $\epsilon = 0.1$. The symbols stand for analytical values whereas lines represent the results obtained from finite difference method.

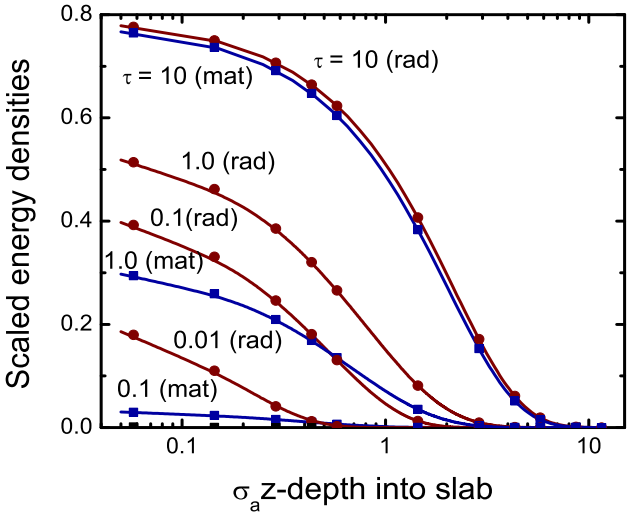

Figure 5.8: Scaled radiation $u_r(x,\tau)$ and material energy density $u_m(x,\tau)$ Vs. slab depth at different times for $\epsilon = 0.1$. The symbols stand for analytical values whereas lines represent the results obtained from finite difference method.

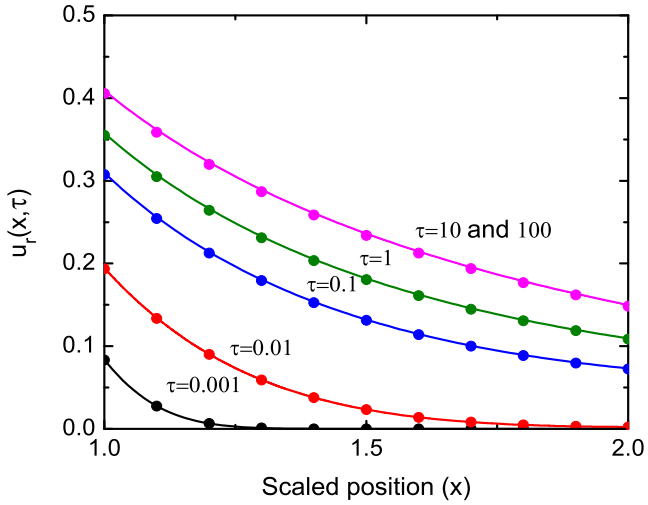

Figure 5.9: Scaled radiation energy density $u_r(x,\tau)$ Vs. position (x) in a spherical shell of scaled inner radius $X_1 = 1$ and outer radius $X_2 = 2$ at different times for $\epsilon = 0.1$. The symbols stand for analytical values whereas lines represent the results obtained from finite difference method.

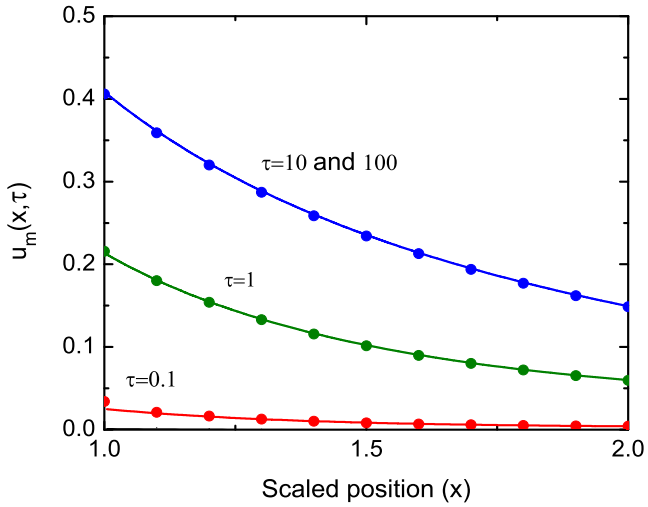

Figure 5.10: Scaled material energy density $u_m(x,\tau)$ Vs. position in a spherical shell of scaled inner radius $X_1 = 1$ and outer radius $X_2 = 2$ at different times for $\epsilon = 0.1$. The symbols stand for analytical values whereas lines represent the results obtained from finite difference method.

5.3.1.2 Spherical shell

Numerical results for energy densities in the spherical shell are obtained from finite difference analysis using the same mesh width and time step as used for the planar slab. Good agreement between the analytical and numerical results establish the validity of finite difference radiation diffusion in spherical geometry. Magnitude of derivative of analytical radiation and material energy densities remains higher in the inner meshes as compared to outer ones at all times [figures 5.9 and 5.10].

5.4 Discrete ordinates method for solving the radiation transport equation

In the Gray approximation, or one group model, the time dependent radiation transport equation in a stationary medium is

$$\frac{1}{c}\frac{\partial I(\vec{r},\vec{\Omega},t)}{\partial t} + \vec{\Omega}.\vec{\nabla} I(\vec{r},\vec{\Omega},t) + (\sigma_R(T)+\sigma_s) I(\vec{r},\vec{\Omega},t) = \frac{\sigma_R(T)B(T)}{4\pi} + \frac{\sigma_s}{4\pi}\int I(\vec{r},\vec{\Omega}',t)d\vec{\Omega}', \tag{5.88}$$

where $I(\vec{r},\vec{\Omega},t)$ is the radiation intensity, due to photons moving in the direction $\vec{\Omega}$, at space point $\vec{r}$ and time t. Here $\sigma_R(T)$ is the one group radiation opacity, which is assumed to be calculated by Rosseland weighing, at electron temperature T (the subscript of T_{elec} is dropped for convenience). As already mentioned, B(T) is the radiation energy flux emitted by the medium which is given by the Stefan-Boltzmann's law $B(T) = acT^4$. The radiation constant a is $\simeq 137$ if T is in keV and c in $cm/\mu s$. This formula for the emission rate follows from the local thermodynamic equilibrium (LTE) approximation, which is assumed in the present model. The scattering cross-section σ_s, representing Thomson scattering is assumed to be isotropic and independent of temperature. In the Lagrangian framework the radiation transport equation for a

planar medium is

$$\frac{1}{c}\rho\frac{\partial}{\partial t}(\frac{I}{\rho}) + \mu\frac{\partial I}{\partial x} + (\sigma_R(T) + \sigma_s)I(x,\mu,t) = \frac{\sigma_R(T)B(T)}{2} + \frac{\sigma_s}{2}\int_{-1}^{1} I(x,\mu\prime,t)d\mu\prime, \tag{5.89}$$

where $I(x,\mu,t)$ is the radiation intensity along a direction at an angle $cos^{-1}(\mu)$ to the x axis. The term $\rho\frac{\partial}{\partial t}(\frac{I}{\rho})$ in this equation arises due to the Lagrange scheme used in solving the hydrodynamic equations.

Backward difference formula for the time derivative gives

$$\mu\frac{\partial I^{n,k}}{\partial x} + [\sigma_R^{n,k-1} + (c\Delta t)^{-1} + \sigma_s]I^{n,k} = \frac{\sigma_R^{n,k-1}B^{n,k-1}}{2} + \frac{\sigma_s}{2}\int_{-1}^{1} I^{n,k}(\mu\prime)d\mu\prime + \frac{\rho^{n,k-1}}{\rho^{n-1}}I^{n-1}(c\Delta t)^{-1}. \tag{5.90}$$

Here, ‘n’ and ‘k’ denote the time step and iteration index for temperature respectively. This iteration arises because the opacity $\sigma_R(T)$ and the radiation emission rate $\sigma_R(T)B(T)$ are functions of the local temperature T. The converged spatial temperature distribution is assumed to be known for the hydrodynamic cycle for the previous time step. Starting with the corresponding values of $\sigma_R(T)$ and B(T) , denoted by $\sigma_R^{n,0}$ and $B^{n,0}$, the radiation energy fluxes are obtained from the solution of the transport equation (Eqn. [5.90]). The method of solution, well known in neutron transport theory, is briefly discussed below. This is used in the electron energy equation of hydrodynamics (Eqn. [6.3]) to obtain a new temperature distribution and corresponding values of $\sigma_R^{n,1}$ and $B^{n,1}$. The transport equation is again solved using these new estimates and the iterations are continued until the temperature distribution converges.

Finally the transport equation can be expressed in conservation form in spherical geometry

as

$$\frac{\mu}{r^2}\frac{\partial}{\partial r}(r^2 I^{n,k}) + \frac{\partial}{\partial \mu}[\frac{(1-\mu^2)I^{n,k}}{r}] + \sigma I^{n,k} = Q(r,\mu), \tag{5.91}$$

with

$$\sigma = \sigma_R^{n,k-1} + (c\Delta t)^{-1} + \sigma_s, \tag{5.92}$$

$$Q(r,\mu) = \frac{\sigma_R^{n,k-1} B^{n,k-1}}{2} + \frac{\sigma_s}{2}\int_{-1}^{1} I^{n,k}(\mu\prime)d\mu\prime + \frac{\rho^{n,k-1}}{\rho^{n-1}} I^{n-1}(c\Delta t)^{-1}, \tag{5.93}$$

where, the second term in eqn. [5.91] accounts for angular redistribution of photons during free flight. This term arises as a result of the local coordinate system used to describe the direction of propagation of photons. If this term is omitted, eqn. [5.91] reduces to that for planar medium and therefore a common method of solution can be applied.

A slightly more accurate linearization [101] can be introduced in Eqs. [5.90] and [5.91] by replacing $B^{n,k-1}$ with $B^{n,k}$. Then, a first order Taylor expansion can be used for the approximation $B^{n,k} = B^{n,k-1} + (\partial B/\partial T)^{n,k-1}(T^{n,k} - T^{n,k-1})$ from which $(T^{n,k} - T^{n,k-1})$ can be eliminated using eqn. [6.3]. The convergence of this modified method for treating the non-linearity of the Planck function may be better compared to the simple iteration method. However, for the problems considered in this thesis we have successfully used the iteration method.

To solve eqn. [5.91], it is written in the discrete angle variable as [26]

$$\frac{\mu_m}{r^2}\frac{\partial}{\partial r}(r^2 I_m) + \frac{2}{r\omega_m}(\alpha_{m+1/2} I_{m+1/2} - \alpha_{m-1/2} I_{m-1/2}) + \sigma I_m = Q_m, \tag{5.94}$$

where the indices ‘n’ and ‘k’ on I have been suppressed. Here m refers to a particular value of μ in the angular range [-1,1] which is divided into M directions. The parameter ω_m is the weight attached to this direction whose value has been fixed according to the Gauss quadrature and $\alpha_{m\pm1/2}$ are the angular difference coefficients. I_m and $I_{m\pm1/2}$ are the intensities at the centres

and the edges of the angular cell respectively. The angle integrated balance equation for photons is satisfied if the "α-coefficients" obey the condition

$$\Sigma_{m=1}^{M}[\alpha_{m+1/2}I_{m+1/2} - \alpha_{m-1/2}I_{m-1/2}] = 0. \tag{5.95}$$

As photons traversing along $\mu = \pm 1$ are not redistributed during the flight, the α-coefficients also obey the boundary conditions

$$\alpha_{1/2} = \alpha_{M+1/2} = 0. \tag{5.96}$$

For a spatially uniform and isotropic angular flux, eqn. [5.94] yields the recursion relation

$$\alpha_{m+1/2} = \alpha_{m-1/2} - \omega_m \mu_m, \tag{5.97}$$

as the intensity $I(r, \mu)$ is a constant in this case.

The finite difference version of eqn. [5.94] in space is derived by integrating over a cell of volume V_i bounded by surfaces $A_{i\pm 1/2}$ where $V_i = 4\pi \int_{r-1/2}^{r+1/2} r^2 dr = \frac{4\pi}{3}(r_{i+1/2}^3 - r_{i-1/2}^3)$ and $A_{i\pm 1/2} = 4\pi r_{i\pm 1/2}^2$. The discrete form of the transport equation in space and angle is thus obtained as

$$\begin{aligned}\frac{\mu_m}{V_i}[A_{i+1/2}I_{m,i+1/2} - A_{i-1/2}I_{m,i-1/2}] + \frac{2(A_{i+1/2} - A_{i-1/2})}{\omega_m V_i} \\ \times[\alpha_{m+1/2}I_{m+1/2,i} - \alpha_{m-1/2}I_{m-1/2,i}] + \sigma I_{m,i} = Q_{m,i}.\end{aligned} \tag{5.98}$$

The cell average intensity and source are given by

$$I_{m,i} = \frac{1}{V_i} 4\pi \int_{r_{i-1/2}}^{r_{i+1/2}} r^2 I_m(r) dr, \tag{5.99}$$

and

$$Q_{m,i} = \frac{1}{V_i} 4\pi \int_{r_{i-1/2}}^{r_{i+1/2}} r^2 Q_m(r) dr, \tag{5.100}$$

respectively, where 'i' specifies the spatial mesh.

As mentioned earlier, planar geometry equations are obtained if the terms involving $\alpha_{m\pm1/2}$ are omitted and the replacements $V_i = r_{i+1/2} - r_{i-1/2}$ and $A_{i+1/2} = 1$ are made. Thus, both geometries can be treated on the same lines using this approach. The difference scheme is completed by assuming that the intensity varies exponentially between the two adjacent faces of a cell both spatially and angularly so that the centered intensity $I_{m,i}$ can be expressed as [102]:

$$I_{m,i} = I_{m,i-1/2}\ exp\ [-\frac{1}{2}(r_{i+1/2} - r_{i-1/2})], \tag{5.101}$$

$$I_{m,i} = I_{m,i+1/2}\ exp\ [+\frac{1}{2}(r_{i+1/2} - r_{i-1/2})], \tag{5.102}$$

where the radii $r_{i+1/2}$ and $r_{i-1/2}$ are expressed in particle mean free paths. These relations show that

$$I^2_{m,i} = I_{m,i-1/2} I_{m,i+1/2}, \tag{5.103}$$

for the spatial direction. Similarly, for the angular direction one gets

$$I^2_{m,i} = I_{m-1/2,i} I_{m+1/2,i}. \tag{5.104}$$

Use of these difference schemes guarantees positivity of all the angular fluxes if $Q_{m,i}$ are posi-

tive. The symmetry of the intensity at the centre of the sphere is enforced by the conditions

$$I_{M+1-m,1/2} = I_{m,1/2},\ \ m = 1, 2, ..., M/2. \tag{5.105}$$

Dividing the spatial range into L intervals, for a vacuum boundary at $r_{L+1/2}$, we have

$$I_{m,L+1/2} = 0,\ \ m = 1, 2, ..., M/2 \tag{5.106}$$

i.e, at the rightmost boundary the intensities are zero for all directions pointing towards the medium. Alternately, boundary sources, if present, can also be specified.

An iterative method is used to solve the transport equation to treat the scattering term. The radiation densities at the centre of the meshes are taken from the previous time step, thereby providing the source explicitly. The intensities $I_{1/2,i}$ for all meshes do not occur in eqn. [5.98] as $\alpha_{1/2} = 0$. Then the intensities $I_{3/2,i}$ are eliminated from this equation using the upwind scheme $I_{3/2,i} = I_{1,i}$. Starting from the boundary condition, viz. eqn. [5.106], eqn. [5.98] and eqn. [5.103] can be used to determine these two intensities for all the spatial meshes 'i'. Thereafter together with eqn. [5.104], the intensities for all the negative values of μ_m can be solved for. At the centre, the reflecting boundary condition given by eqn. [5.105] provide the starting intensities for the outward sweeps through all the spatial and angular meshes with positive values of μ_m.

This completes one space-angle sweep providing new estimates of radiation energy flux (at the mesh centres) given by:

$$E_{Ri}^{n,k} = \sum_m \omega_m I_{m,i} / \sum_m \omega_m \tag{5.107}$$

where the sum extends over all directions M. The mesh-angle sweeps are repeated until the scattering source distribution converges to a specified accuracy. The rate of radiation energy

absorbed by unit mass of the material in the i^{th} mesh is

$$\varepsilon_i = \sigma_{Ri}^{n,k-1}[E_{Ri}^{n,k} - B_i^{n,k-1}]/\rho_i^{n,k}, \tag{5.108}$$

thus providing the material temperatures in the i^{th} mesh at that time step using the material energy equations, viz.

$$\rho[C_{V\,ion}\frac{\partial T_{ion}}{\partial t} + \frac{\partial E_{ion}}{\partial V}\frac{\partial V}{\partial t}] = -P_{ie}, \tag{5.109}$$

$$\rho[C_{V\,elec}\frac{\partial T_{elec}}{\partial t} + \frac{\partial E_{elec}}{\partial V}\frac{\partial V}{\partial t}] = \sigma_R(T_{elec})[E_R(r, T_{elec}) - B(T_{elec})] + P_{ie} \tag{5.110}$$

by ignoring hydrodynamic motion, i.e., considering the meshes to be fixed.

5.4.1 Results

We have investigated the performance of the scheme using these benchmark problems:

Marshak wave problem

In figure 5.11, we plot the scaled radiation and material energy densities $u_r(x,\tau)$ and $u_m(x,\tau)$ as functions of position in the slab at different times for $\epsilon = 0.1$. For numerical simulation we have chosen opacity $\sigma_a = 100cm^{-1}$ and mesh width $\Delta z = 10^{-3}cm$ in order to maintain $\sigma_a \Delta z = 0.1$. Comparison with the analytical results show good agreement at later times, whereas there is slight disagreement at earlier times. As the analytical results are obtained for the Marshak diffusion problem whereas our results employ the full radiation transport, slight difference at earlier times is expected because of larger penetration for diffusion approximation. For $\sigma_a = 0.558cm^{-1}$, and mesh width $\Delta z = 0.1792cm$, the comparison between the analytical and numerical solution for the scaled radiation temperature $(T_r/T_{inc})^4$ and material temperature $(T_m/T_{inc})^4$ are shown in figures 5.12 and 5.13 respectively.

Steady state radiative heat flux The steady state radiative heat flux through a finite planar

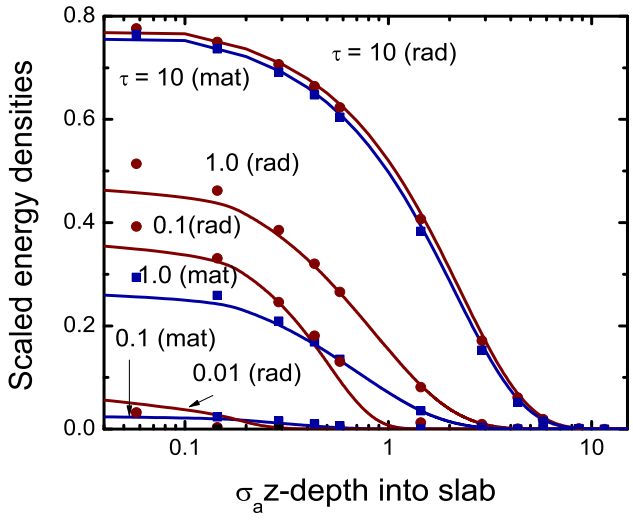

Figure 5.11: Linear plot of the radiation energy density and material energy density as functions of position in the slab at different times. The symbols represent the analytical solutions.

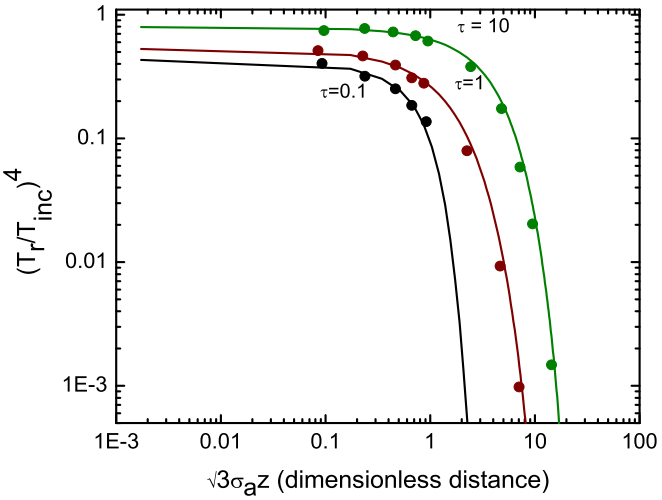

Figure 5.12: Linear plot of the scaled radiation temperature density $(T_r/T_{inc})^4$ as functions of position in the slab at different times. The symbols represent the analytical solutions.

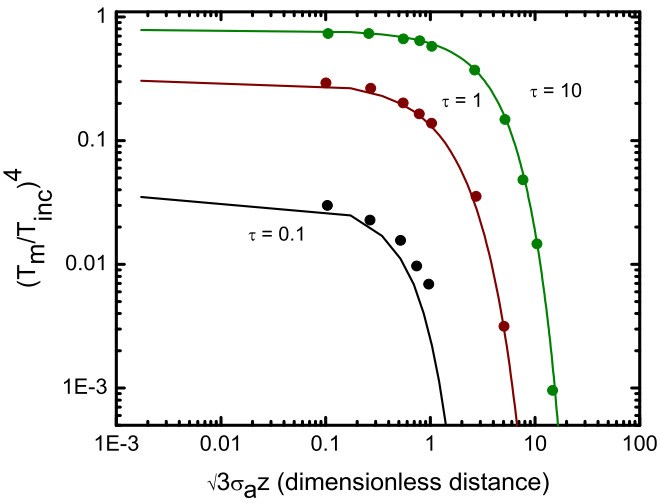

Figure 5.13: Linear plot of the scaled material temperature density $(T_m/T_{inc})^4$ as functions of position in the slab at different times. The symbols represent the analytical solutions.

slab containing a Grey absorbing and emitting gas of optical depth τ is given by

$$F_T = \frac{\sigma_B(T_2^4 - T_1^4)}{R(t)}, \tag{5.111}$$

where the interpolation distance R(t) is given by $1 + 3\tau/4 + (\tau/4)/(1 + 3.8070\tau)$. τ is the optical thickness of the medium, σ_B is the Stefan Boltzmann constant, T_1 and T_2 are the temperatures on two sides of the slab. This expression is accurate to 0.3% [103]

For the purpose of numerical simulation, we consider a slab of material 0.5 cm thick, of density $\rho = 10$ g/cc, specific heat 10^{12}ergs/g/eV and initial temperature of 100eV driven by a blackbody at 4keV. The value of opacity is $\sigma_a = 10\text{cm}^{-1}$ and the blackbody boundary condition is applied at 0.05cm. This slab has an optical thickness of τ = 5. As observed in figure 5.14, initially the radiation flux is high on the incident surface and falls off with distance. As time progresses, it penetrates more into the slab with a slight drop on the surface. Finally, at 1.37×10^{-9} s, the steady state value of $5.476 \times 10^{25}\text{ergs/cm}^2\text{/s}$ is attained which is in good

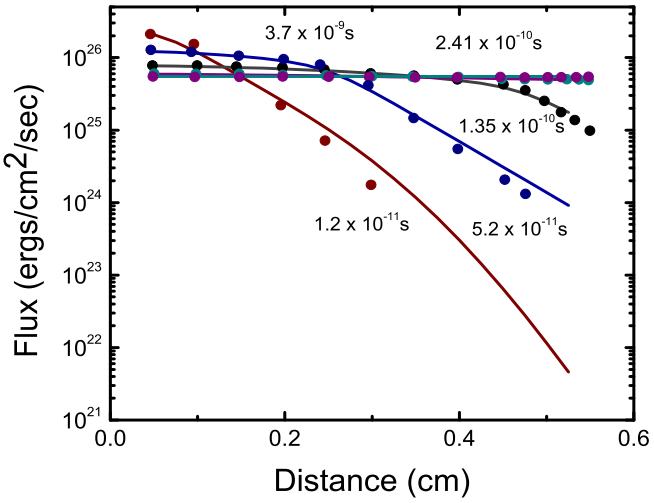

Figure 5.14: Radiation flux Vs. position at consecutive times. The symbols represent the solutions generated by Wilson [104]

agreement with the theoretical value of $5.31 \times 10^{25}\mathrm{ergs/cm^2/s}$ obtained from eqn. [5.111] and also with earlier numerically obtained value of $5.54 \times 10^{25}\mathrm{ergs/cm^2/s}$ [104]. A time step of 10^{-16} s and a mesh width of 2.5×10^{-2} cm has been used for these simulations. The radiation energy density and temperature as a function of position are shown in figures 5.15 and 5.16, respectively.

Marshak wave problem in spherical geometry In the literature, though there are plenty of results on radiation transport in planar geometry, that in spherical geometry is scarce. Honrubia has generated results for Marshak wave propagation problem in spherical geometry using 1D-radiation hydrodynamics code called SARA that implicitly solves the multigroup radiation transport equations [93]. We generate results for radiation and material energy densities in a sphere using opacity $\sigma = 100\mathrm{cm}^{-1}$ and mesh width $\Delta z = 10^{-3}$ cm as for the planar case. The radius of the sphere is chosen to be 0.05 cm and a time independent radiative flux $= c/4$ falls on the surface of the sphere. The plots for scaled radiation and material energy densities are similar to planar case at earlier times. At steady state, the radiation and material temperatures become

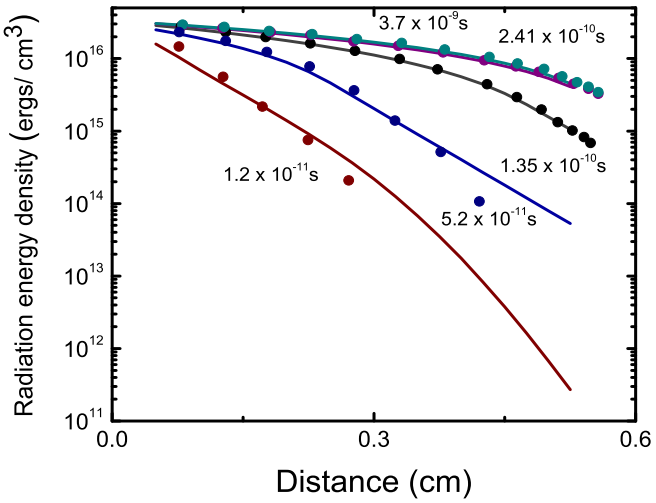

Figure 5.15: Radiation energy density Vs. position in the slab at consecutive times. The symbols represent the solutions generated by Wilson [104]

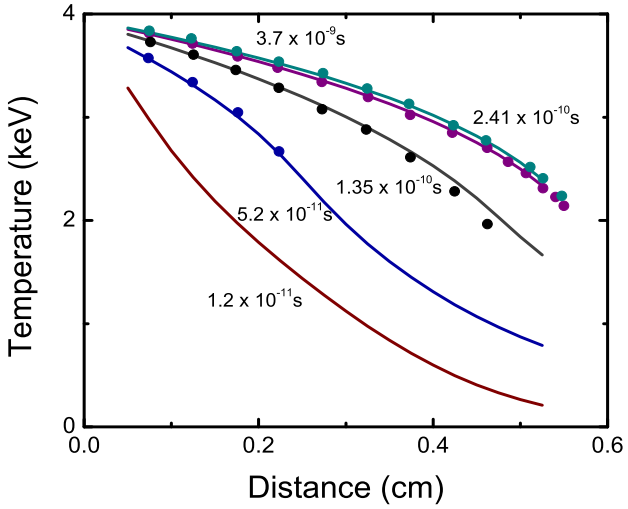

Figure 5.16: Radiation temperature Vs. position at consecutive times. The symbols represent the solutions generated by Wilson [104]

equal to 1 and is almost constant throughout the sphere as there is no loss from the centre. In the planar case, as there is loss from the other side of the finite slab, at steady state, the temperatures are found to decrease away from the incident surface. The results for spherical geometry are shown in figure 5.17. Let us consider a simplified case where radiation is not emitted by the material. We derive an analytical solution for the steady state under diffusion approximation with the plasma having a constant opacity and neglecting the heating and cooling rates. In this case, the time independent diffusion equation without emission term is

$$\vec{\nabla}.(-\frac{c}{3\sigma_a}\vec{\nabla}I) = -c\sigma_a I. \tag{5.112}$$

In spherical coordinates,

$$-\frac{c}{3\sigma_a}[\frac{\partial^2 I}{\partial r^2} + \frac{2}{r}\frac{\partial I}{\partial r}] = -c\sigma_a I \tag{5.113}$$

$$\text{or, } \frac{\partial^2 I}{\partial r^2} + \frac{2}{r}\frac{\partial I}{\partial r} - 3\sigma_a^2 I = 0 \tag{5.114}$$

as the opacity σ_a is assumed to be a constant. Let us change the variable I to J=Ir. Hence,

$$I = J/r, \tag{5.115}$$

$$\frac{\partial I}{\partial r} = \frac{1}{r}\frac{\partial I}{\partial r} - \frac{J}{r^2}, \tag{5.116}$$

$$\text{and } \frac{\partial^2 I}{\partial r^2} = -\frac{2}{r^2}\frac{\partial J}{\partial r} + \frac{1}{r}\frac{\partial^2 J}{\partial r^2} + \frac{2J}{r^3}. \tag{5.117}$$

Substituting in eqn. [5.114], the time independent diffusion equation in J becomes

$$\frac{\partial^2 J}{\partial r^2} - 3\sigma_a^2 J = 0, \tag{5.118}$$

which is a second order differential equation with constant coefficients. The solutions to this equation are $\exp(+\sqrt{3}\sigma_a)$ and $\exp(-\sqrt{3}\sigma_a)$ i.e., $\exp(\lambda x)$ and $\exp(-\lambda x)$ with $\lambda = \sqrt{3}\sigma_a$.

Hence, the solutions for I are $\frac{\exp(\lambda r)}{r}$ and $\frac{\exp(-\lambda r)}{r}$. Linear combinations of the solution yield $\frac{2\sinh(\lambda r)}{r}$ and $\frac{2\cosh(\lambda r)}{r}$ as the solutions. As the solution $\cosh(\lambda r)$ diverges at r=0, the solution for I is $\frac{A\sinh(\lambda r)}{r}$ with A as the multiplication constant. In diffusion theory, the flux of radiation falling on the sphere is given by

$$\frac{I}{4} + \frac{D}{2}\frac{\partial I}{\partial r} = \frac{acT_{inc}^4}{4} \quad \text{at } r = R \tag{5.119}$$

where T_{inc} is the incident radiation temperature and R is the radius of the sphere. If T(r)is the radiation temperature at a distance r from the centre, then

$$acT(r)^4 = \frac{A\sinh(\lambda r)}{r}, \tag{5.120}$$

and

$$\frac{acT_0^4}{4} = \frac{A\sinh(\lambda R)}{4R} + \frac{DA}{2}[\frac{\lambda}{R}\cosh(\lambda R) - \frac{\sinh(\lambda R)}{R^2}]. \tag{5.121}$$

Dividing,

$$T(r) = T_0[\frac{1}{2}\frac{R}{\frac{\sinh(\lambda R)}{2} + D(\lambda\cosh(\lambda R) - \frac{\sinh(\lambda R)}{R})}\frac{\sinh(\lambda r)}{r}]^{1/4}. \tag{5.122}$$

Steady state scaled radiation temperatures within the sphere obtained from our radiation transport code (for order 2 and 4 in the discrete ordinates method on switching off the emission term) are compared to the analytical solution in figure 5.18. Results obtained for lower order agrees better with the analytical results as expected.

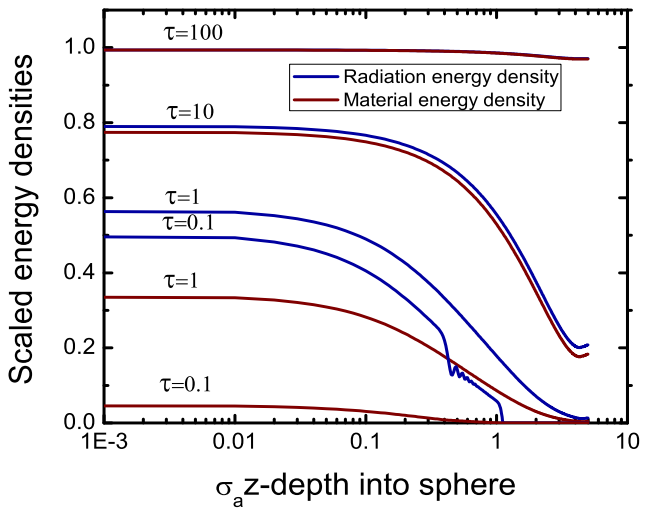

Figure 5.17: Radiation and material energy densities in a sphere at consecutive times.

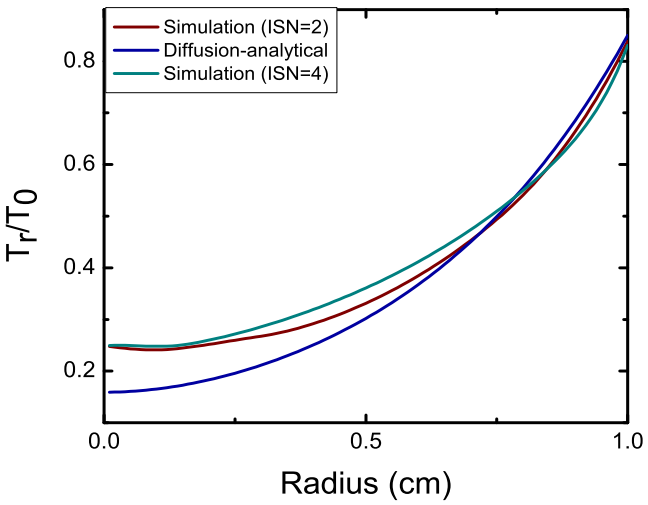

Figure 5.18: Steady state radiation temperatures within a sphere with no emission.

5.5 Summary

In this chapter we develop numerical codes for hydrodynamic motion of the medium, radiation diffusion and transport and validate them using analytical or semi-analytical results. The Lagrangian hydrodynamic code is solved implicitly by solving the system of equations for the velocities in the adjacent meshes at each time step. The code is able to reproduce analytical results in all the three geometries. Results obtained from the finite difference radiation diffusion program agrees with the analytical results derived in the earlier chapter for finite systems and also for the infinite planar slab. Radiation transport equation is solved using the discrete ordinates method and compared with available results. New results are also obtained for radiation transport through a sphere. These codes serve as starting point for developing the radiation hydrodynamics code in the next chapter.

6 Fully implicit 1D radiation hydrodynamics: validation and verification

6.1 Introduction

Radiation hydrodynamics is a dynamical description of fluid material interacting with electromagnetic radiation and is appropriate whenever radiation governs the transport of energy and momentum in the fluid [105]. In the earlier chapter, we develop codes for determining the radiation field in a material when its state, i.e., temperature and density distributions are known. At moderate densities and temperatures, the radiation energy density and radiation pressure are negligible in comparison with the energy and pressure of the fluid. As the velocity of light is much greater than the fluid velocity, the energy flux in the fluid and the radiant energy flux can become comparable, even if the radiant energy density is much less than the energy density of the fluid. At high enough temperatures, the radiant pressure dominates as it is proportional to the fourth power of the temperature whereas the material pressure is directly proportional to the temperature [4]. In this chapter, we develop a fully implicit radiation hydrodynamics code applicable for systems where radiative transfer and interaction between radiation and the fluid have a substantial effect on both the state and motion of the medium. The results obtained from this fully implicit radiation hydrodynamics code in the planar geometry agrees well with the scaling law for radiation driven strong shock propagation in aluminium [107]. Good agreement

is obtained between the numerical results for the point explosion problem with radiation interaction and the point explosion with heat conduction as obtained by Meyer ter Vehn [76]. Having, thus, benchmarked the code, self convergence of the method w.r.t. time step is studied in detail for both the planar and spherical problems [78]. Spatial as well as temporal convergence rates are $\simeq 1$ as expected from the difference forms of mass, momentum and energy conservation equations. This shows that the asymptotic convergence rate of the code is realized properly. Earlier studies on the non-equilibrium radiation diffusion calculations show that the accuracy of the solution increases on converging the non-linearities within a time step and increasing benefit is obtained as the problem becomes more and more nonlinear and faster [34], [35].

6.2 Implicit radiation hydrodynamics

Radiation hydrodynamic simulation is performed by coupling the implicit finite difference hydrodynamics with discrete ordinates radiation transport. In the low radiation energy density regime, radiation momentum deposition to the material is not important so that radiation is coupled only to electron energy equation via absorption and emission processes. In this case, the terms O(u/c) can be neglected from the hydrodynamics as well as radiation transport equations. Also, the equations for conservation of mass and momentum remain unchanged as the radiation energy density and work done by the radiation pressure forces are neglected. A term describing the radiation absorption and emission is introduced into the electron energy equation as

$$\rho[C_{V elec}\frac{\partial T_{elec}}{\partial t} + \frac{\partial E_{elec}}{\partial V}\frac{\partial V}{\partial t}] = -\frac{P_{elec}}{V}\frac{\partial V}{\partial t} + \sigma_R(T_{elec})[E_R(r, T_{elec}) - B(T_{elec})] + P_{ie}. \quad (6.1)$$

The discrete form of the energy equations for ions and electrons are

$$T_{ion,i}^{n,k} = T_{ion,i}^{n-1} - (P_{ion,i}^{n,k-1}\,\Delta V_i^{n,k} + \frac{P_{ie}^{n,k-1}\Delta t}{\rho_i^{n,k-1}} + \delta_{ion}^{n,k-1}\Delta V_i^{n,k})/C_{Vion,i}^{n,k-1}, \tag{6.2}$$

and

$$T_{elec,i}^{n,k} = T_{elec,i}^{n,k-1} + \frac{\rho_i^{n,k-1}C_{Velec,i}^{n,k-1}(T_{elec,i}^{n-1} - T_{elec,i}^{n,k-1})}{\Delta t G_i^{n,k-1}}$$
$$+(\frac{\sigma_{Ri}^{n,k-1}}{G_i^{n,k-1}})(E_{Ri}^{n,k} - B_i^{n,k-1}) - \frac{(P_{elec}^{n,k-1} + \delta_{elec}^{n,k-1})\rho_i^{n,k-1}\Delta V_i^{n,k}}{\Delta t G_i^{n,k-1}} + P_{ie}^{n,k-1}/G_i^{n,k-1}, \tag{6.3}$$

where

$$G_i^{n,k-1} = \frac{\rho_i^{n,k}C_{Velec,i}^{n,k-1}}{\Delta t_n} + \sigma_{Ri}^{n,k-1}C_{v,Ri}^{n,k-1}, \tag{6.4}$$

$$\delta_{ion}^{n,k-1} = (\frac{\partial E_{ion}}{\partial V})_i^{n,k-1}, \tag{6.5}$$

$$\delta_{elec}^{n,k-1} = (\frac{\partial E_{elec}}{\partial V})_i^{n,k-1}, \tag{6.6}$$

$$C_{vRi}^{n,k-1} = 4ac(T_{elec,i}^{n,k-1})^3, \tag{6.7}$$

with ‘n’ and ‘k’ denoting the time step and iteration index respectively. Also, the constants $a(= 4\sigma_B/c)$, σ_B and c denote the radiation constant, Stefan-Boltzmann’s constant and the speed of light respectively. Stefan-Boltzmann’s law, $B(T_{elec}) = acT_{elec}^4$, has been used explicitly in these equations.

In the high energy density regime, the total pressure is $P = P_{ion} + P_{elec} + P_{rad}$. Here the radiation pressure is given by $P_{rad} = U/3$ with $U(r,t) = \frac{1}{c}\int I(\Omega)d\Omega$ being the radiation energy density. Also, the total energy is the sum of the radiation and material energies.

We begin the simulation by dividing the sample volume into ‘L’ meshes of equal width. The initial position and velocity of all the vertices are defined according to the problem under consideration. Also the initial pressure, temperature and internal energy of all the meshes are

entered as input.

For any time step, the temperature of the incident radiation is obtained by interpolating the data for the radiation temperature as a function of time (as in the case of shock propagation in aluminium sheet or an ICF pellet implosion in a hohlraum). All the thermodynamic parameters for this time step are initialized using their corresponding values in the previous time step. It is important to note that the velocity u_i in Eqns. [5.3] and [5.16] and position r_i in eqn. [5.2] are the old variables and remain constant unless the pressure and temperature iterations for this time step converge.

The temperature iterations begin by solving the radiation transport equation for all the meshes which gives the energy flowing from radiation to matter.

The 1D Lagrangian step is a leapfrog scheme where new radial velocities $\tilde{u}_i$ arise due to acceleration by pressure gradient evaluated at half time step. This leads to a time implicit algorithm. The first step in the pressure iteration starts by solving the tridiagonal system of equations for the velocity of all the vertices. The sound speed is obtained from the equation of state (EOS) of that material. The new velocities and positions of all the vertices are obtained which are used to calculate the new density and change in volume of all the meshes. The total pressure is obtained by adding the Von Neumann and Richtmeyer artificial viscosity to the ion and electron pressures and solving the energy equations which takes into account both the energy flow from radiation and the work done by (or on) the meshes due to expansion (or contraction). The energy equations for ions and electrons are solved using the corresponding material EOS which provides the pressure and the specific heat at constant volume of the material (both ions and electrons). The hydrodynamic variables like the position, density, internal energy and velocity of all the meshes are updated. The convergence criterion for the total pressure is checked and if the relative error is greater than a fixed error criterion, the iteration for pressure is continued, i.e, the code goes back to solve the tridiagonal equations to obtain the velocities, positions, energies and so on. When the pressure converges according to the error criterion, the convergence for

the electron temperature is checked in a similar manner. The maximum value of the error in electron temperature for all the meshes is noted and if this value exceeds the value acceptable by the error criterion, the temperature iterations are continued, i.e, transport equation, tridiagonal system of equations for velocity, etc, are solved, until the error criterion is satisfied. Thus the method is fully implicit as the velocities of all the vertices are obtained by solving a set of simultaneous equations. Also, both the temperature and pressure are converged simultaneously using the iterative method. Once both the pressure and temperature distributions converge, the position of the shock front is obtained by noting the pressure change and the new time step is estimated as follows:

The time step Δt is chosen so as to satisfy the Courant condition which demands that it is less than the time for a sound signal with velocity c_s to traverse the grid spacing Δx, $\frac{c_s \Delta t}{\Delta x} < C$ where the reduction factor C is referred to as the Courant number. The stability analysis of Von Neumann introduces additional reduction in time step due to the material compressibility [106].

The order of the S_n approximation may take the values 2, 4, 6 and 8. All the results presented in this chapter have been generated using S_n approximation of order 4.

The above procedure is repeated up to the time we are interested in following the evolution of the system. The solution method described above is clearly depicted in the flowchart given in figure 6.2. The time step index is denoted by ‘nh’ and ‘dt’ is the time step taken. The iteration indices for electron temperature and total pressure are expressed as ‘npt’ and ‘npp’ respectively. ‘Error1’ and ‘Error2’ are the fractional errors in pressure and temperature respectively whereas ‘eta1’ and ‘eta2’ are those acceptable by the error criterion.

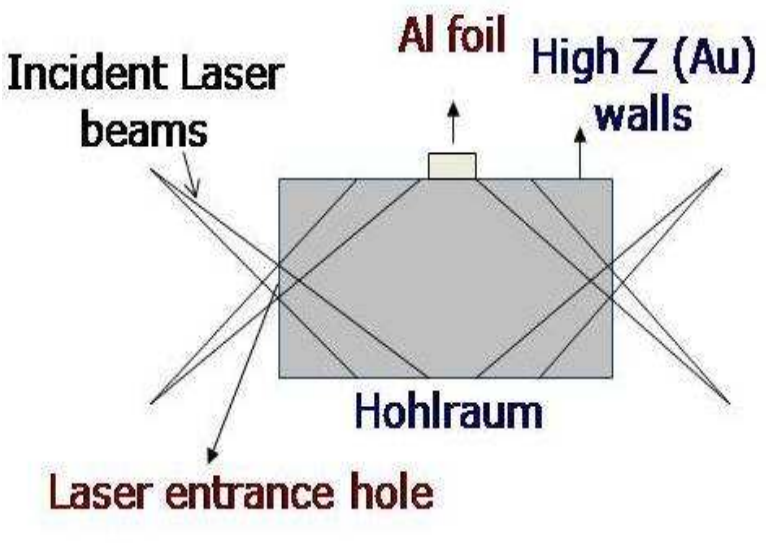

Figure 6.1: Section of a cylindrical hohlraum with a hole in the wall on which an aluminium foil is placed.

6.3 Results

6.3.1 Investigation of the performance of the scheme using benchmark problems

6.3.1.1 Shock propagation in Aluminium

In the indirect drive inertial confinement fusion, high power laser beams are focused on the inner walls of high Z cavities or hohlraums, converting the driver energy to x-rays which implode the capsule. If the x-ray from the hohlraum is allowed to fall on an aluminium foil over a hole in the cavity, the low Z material absorbs the radiation and ablates generating a shock wave as illustrated schematically in 6.1. Using strong shock wave theory, the radiation temperature in the cavity T_r can be correlated to the shock velocity u_s. The scaling law derived for aluminium is $T_r = 0.0126 u_s^{0.63}$, where T_r is in units of eV and u_s is in units of cm/s for a temperature range of 100-250 eV [107].

For the purpose of simulation, an aluminium foil of thickness 0.6 mm and unit cross section is chosen. It is subdivided into 300 meshes each of width 2×10^{-4} cm. An initial guess value of $10^{-7}\mu s$ is used for the time step. The equilibrium density of Al is 2.71 gm/cc. In the discrete ordinates method four angles are chosen. As the temperature attained for this test problem is somewhat low, the total energy equation is solved assuming that electrons and ions are at the same temperature (the material temperature). The EOS and Rosseland opacity for aluminium are given by

$$E = \frac{PV}{\gamma - 1} = \epsilon T^{\mu} V^{\nu}, \tag{6.8}$$

$$\sigma_R = l^{-1} T^{-\mu_R} V^{-\nu_R}. \tag{6.9}$$

Here $V = 1/\rho$ is the specific volume and $\gamma = 1 + \nu/(\mu - 1)$ is the adiabatic index. These power law functions, of temperature and density, where $\epsilon = 12.5$ in units of $10^{14} g^{\nu} cm^{2-3\nu} s^{-2} keV^{-\mu}$, l=5 in units of $g^{\nu_R} cm^{1-3\nu_R} keV^{-\mu_R}$, $\mu = 1.145, \nu = 0.063, \mu_R = 3.8$ and $\nu_R = 1.5$ are the fitting parameters, are quite accurate in the temperature range of interest [108].

Using the fully implicit radiation hydrodynamics code, a number of simulations are carried out for different values of time independent incident radiation fluxes or temperatures. Corresponding shock velocities are then determined after the decay of initial transients. In figure 6.3. we show the comparison between the numerically obtained shock velocities for different radiation temperatures (points) and the scaling law for aluminium (line) mentioned earlier. Good agreement is observed in the temperature range where the scaling law is valid.

Figure 6.4. shows the various thermodynamic variables like velocity, pressure, density and material temperature after 2.5 ns when the radiation profile shown in figure 6.5 is incident on the outermost mesh. This radiation temperature profile is chosen so as to achieve nearly isentropic compression of the fuel pellet. The pulse is shaped in such a way that the pressure on the target surface gradually increases, so that the generated shock rises in strength. From figure 6.4.

we observe that the outer meshes have ablated outwards while a shock wave has propagated inwards. At 2.5 ns, the shock is observed at 0.5 mm showing a peak in pressure and density. As the outer region has ablated, they move outwards with high velocities. The outermost mesh has moved to 1.2 mm. The meshes at the shock front move inwards showing negative velocities. Also the temperature profile shows that the region behind the the shock gets heated to about 160 eV. In figure 6.6. we plot the distance traversed by the shock front as a function of time for the above radiation temperature profile. The shock velocity changes from 3.54 to 5.46 $cm/\mu s$ at 1.5 ns when the incident radiation temperature increases to 200 eV.

All the runs in this study were done on a Pentium(4) computer having 1GB of RAM operating at 3.4 GHz.

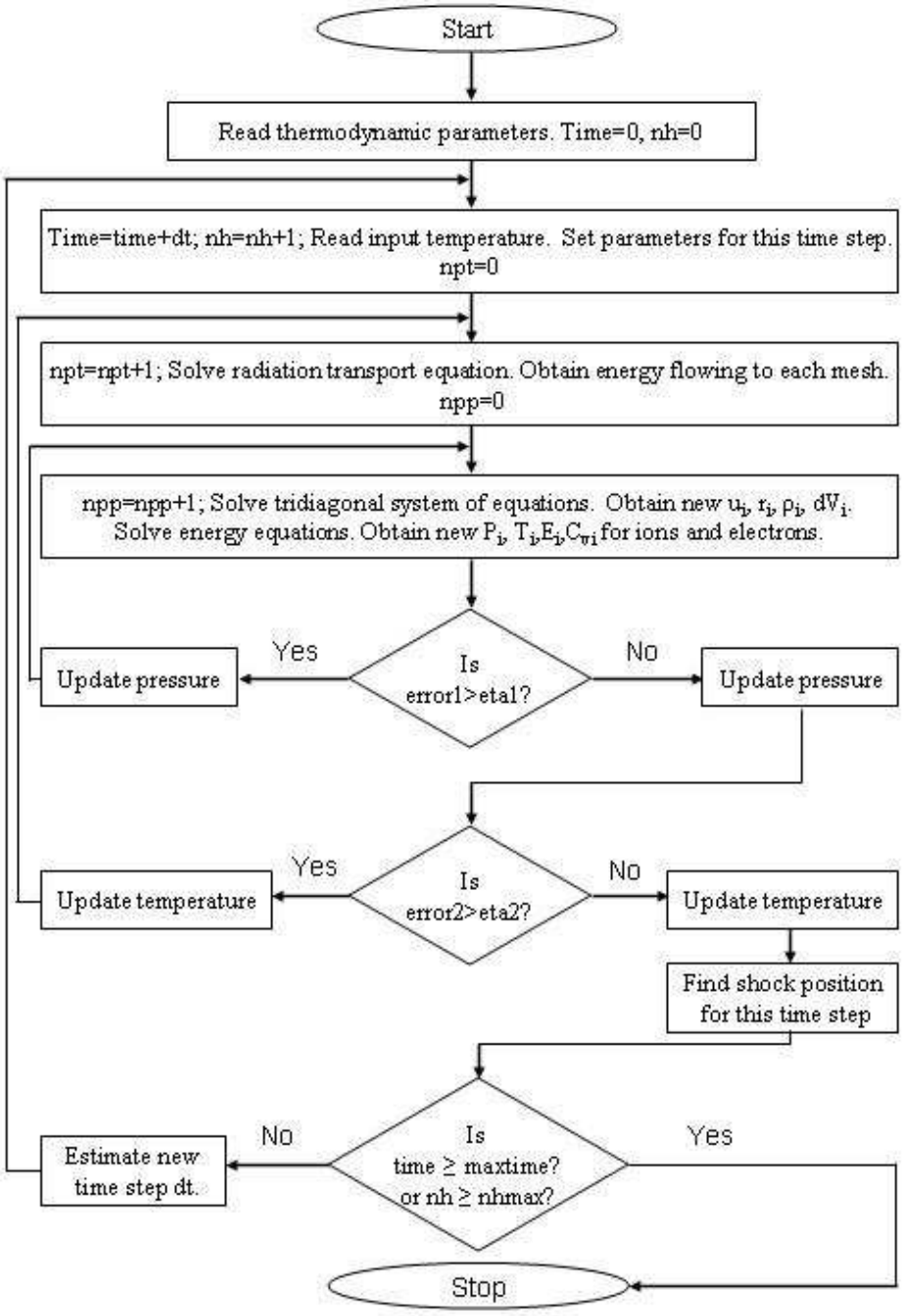

Figure 6.2: Flowchart for the Implicit 1D Radiation Hydrodynamics. Here, 'nh' is the time step index and 'dt' is the time step taken. The iteration indices for electron temperature and total pressure are 'npt' and 'npp' respectively. 'Error1' and 'Error2' are the fractional errors in pressure and temperature respectively whereas 'eta1' and 'eta2' are those acceptable by the error criterion.

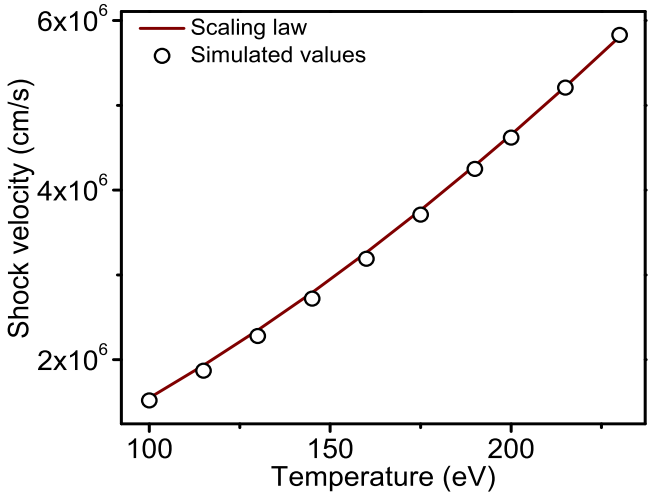

Figure 6.3: Comparison of simulation data (points) with scaling law (line) relating shock velocity with the radiation temperature for aluminium.

6.3.1.2 Point explosion problem with heat conduction

P. Reinicke and J. Meyer-ter-Vehn (RMV) analyzed the problem of point explosion with nonlinear heat conduction for an ideal gas equation of state and a heat conductivity depending on temperature and density in a power law form [76]. The problem combines the hydrodynamic (Sedov) point explosion with the spherically expanding nonlinear thermal wave. The RMV problem is a good test to determine the accuracy of coupling two distinct physics processes: hydrodynamics and radiation diffusion. Later on, Shestakov presented the results of point explosion with heat conduction using a coupled hydrodynamic diffusion code [77]. We generate the results for the point explosion including radiation interaction using our fully implicit radiation hydrodynamics code. In the heat conduction approximation, the energy equation is written as

$$\frac{\partial}{\partial t}(\rho E) + \vec{\nabla}.(\vec{u}(\rho E + P)) = -\vec{\nabla}.\vec{H}_f, \tag{6.10}$$

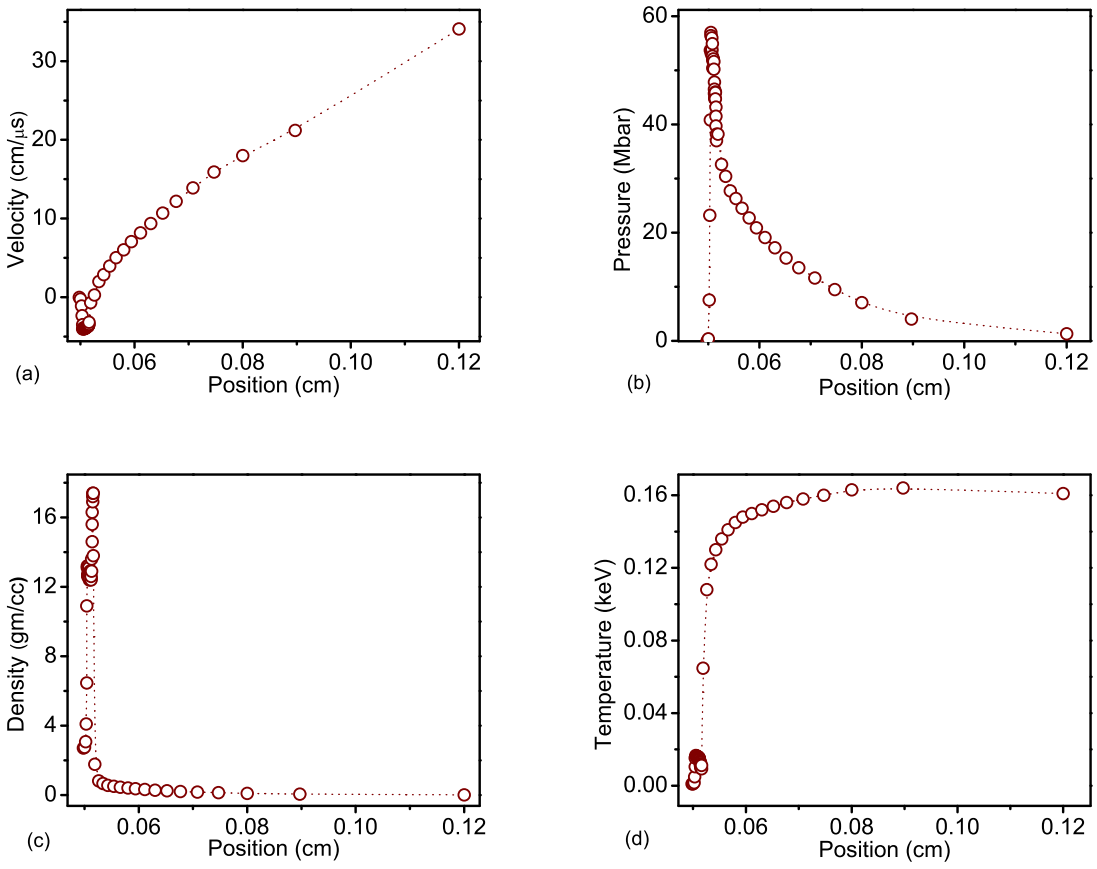

Figure 6.4: Profiles of the thermodynamic variables: (a) velocity, (b) pressure, (c) density and (d) temperature in the region behind the shock as a function of position at t = 2.5 ns. The region ahead of the shock is undisturbed and retain initial values of the variables. The incident radiation temperature on the Al foil is shown in figure 6.5.

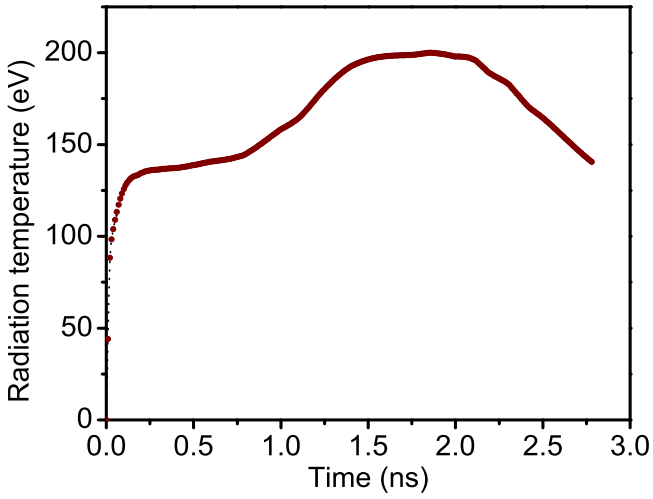

Figure 6.5: Radiation temperature profile in the hohlraum for strong shock propagation in aluminium.

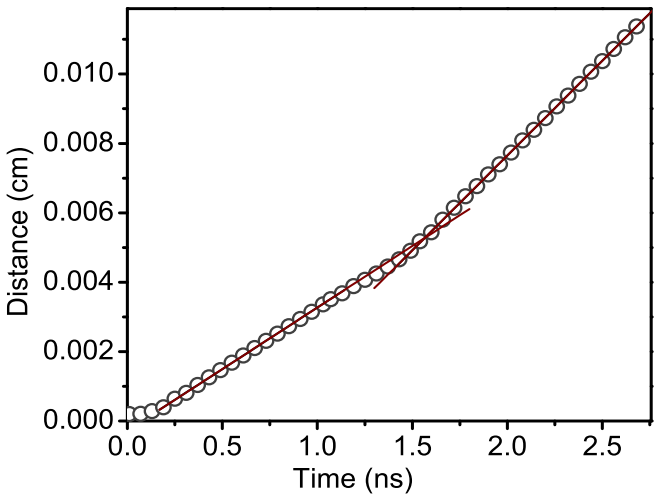

Figure 6.6: Distance traversed by the shock front Vs. time in Al foil for incident radiation temperature shown in figure 6.5. The two slopes correspond to the two plateaus in the radiation profile.

where the heat flux $\vec{H}_f = -\chi\vec{\nabla}T$ and the conductivity is of the form $\chi = \chi_0\rho^{a_0}T^{b_0}$ where χ_0, a_0 and b_0 are constants. The conductivity can be related to Rosseland opacity as follows: $\vec{H}_f = -\frac{c}{3\sigma_R}\vec{\nabla}E_R$ in the heat conduction approximation. Now, $E_R = aT^4$ and therefore, $\vec{H}_f = -\frac{4acT^3}{3\sigma_R}\vec{\nabla}T$, so that $\chi = \frac{4acT^3}{3\sigma_R}$. The Rosseland opacity is assumed to vary with density and temperature as $\sigma_R = \sigma_0\rho^m T^{-n}$. Substituting the functional dependencies of conductivity and Rosseland opacity into the equation relating the two, we obtain $a_0 = -m$ and $b_0 = n + 3$. For the problem under consideration, $a_0 = -2$ and $b_0 = 6.5$. So, the Rosseland opacity used in our code is $\sigma_R = \sigma_0\rho^2T^{-3.5}$ with $\sigma_0 = \frac{4ac}{3\chi_0}$. As in the RMV problem, the initial gas density is assumed to be $\rho = g_0 r^k$ with $k = -(6b_0 - 1)/(2b_0 - 2a_0 + 1) = -2.111$ in this case. The thermodynamic variables are related by the ideal gas equation of state, $\frac{P}{\rho} = NkT = RT = (\gamma - 1)E = \Gamma T$. If energy is in unit of 10^{16} ergs, pressure in 10^{16} ergs/cc, temperature in keV and density in gm/cc, then we can set $\Gamma = g_0 = \chi_0 = 1$.

The normalized density, pressure, velocity and temperature obtained from our radiation hydrodynamic code for $\gamma = 5/4$ at 4.879 ns for a total energy of 16.9×10^{16} ergs deposited in the first mesh are shown in figure 6.7. The results agree with those published by RMV and those generated by Shestakov. The kink in ρ/ρ_1 and a sharp drop in T/T_1 at a distance of 0.57 cm are observed which shows that the heat front lags behind the shock front in this case. The smooth variation of temperature near the origin shows the effectiveness of radiative energy transfer from regions of high temperature. But for the unperturbed power law density profile ahead of the shock front, profiles of other variables are somewhat similar to point explosion problem without heat conduction.

For energy deposition of 235×10^{16} ergs, the heat front is found to move ahead of the shock front at 0.5145 ns in RMV problem. The perturbations in other variables (pressure and velocity) generated by the advancing heat front are observed by Shestakov also. However, the results of our radiation hydrodynamic code does not show these features. As shown in figure 6.8, the heat wave does not move beyond the shock wave and consequently all the variables are

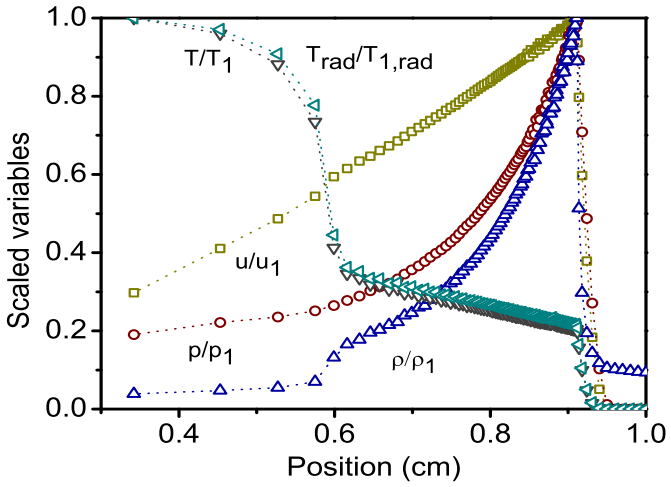

Figure 6.7: Profiles of the scaled thermodynamic variables at t = 4.879 ns for the point explosion problem including radiation interaction for $\gamma = 5/4$. Total energy 16.9×10^{16} ergs is deposited at t=0 in the innermost mesh.

unperturbed ahead of the shock front. The reason behind this difference is the use of heat conduction approximation by RMV and Shestakov. For the well known Marshak wave propagation problem [67],[109], it is found that diffusion approximations lead to a deeper penetration of radiation into the medium. However, this does not happen when full radiation transport is taken into account. Further, in the heat conduction approximation, radiation energy density does not evolve independently to reach a distribution in equilibrium with material temperature. The heat flux $\vec{H}_f = -\frac{4ac}{3\sigma_0}\rho^{-2}T^{6.5}\vec{\nabla}T$, because of its temperature dependence, peaks beyond the region where $|\vec{\nabla}T|$ begins to decrease. For very high energy deposition, the heat front apparently moves ahead of the shock front due to pre-heating by radiation conduction. We are attempting a quantitative characterization of this phenomenon.

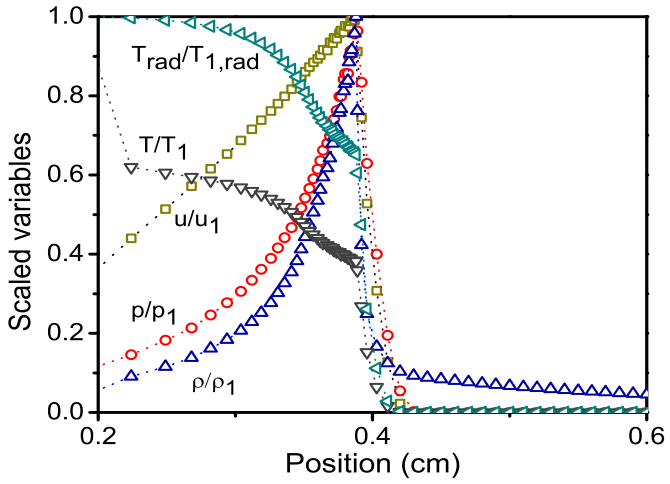

Figure 6.8: Profiles of the scaled thermodynamic variables at t = 0.5145 ns for the point explosion problem including radiation interaction for $\gamma = 5/4$. Total energy 235×10^{16} ergs is deposited at t=0 in the first mesh.

6.3.2 Asymptotic convergence analysis of the code

Asymptotic convergence analysis is performed for conducting verification analysis of the code. The asymptotic convergence rate quantifies the convergence properties of the software implementation (code) of a numerical algorithm for solving the discretized forms of continuum equations [78].

In the Lagrangian formalism as used in our code though the mesh sizes vary non uniformly with time, the mass of a mesh remains constant. For any variable ξ computed for a given mesh of mass Δm_i and uniform time step Δt_l, the fundamental *ansatz* of pointwise convergence analysis is that the difference between the exact and the computed solutions can be expanded as a function of the mass and temporal zone sizes:

$$\xi^* - \xi_i^l = \epsilon_0 + A(\Delta m_i)^p + B(\Delta t_l)^q + C(\Delta m_i)^r(\Delta t_l)^s + O((\Delta m_i)^p, \quad (6.11)$$
$$(\Delta t_l)^q, (\Delta m_i)^r(\Delta t_l)^s)$$

where ξ^* is the exact value, ξ_i^l is the value computed on the grid of zone mass Δm_i and time step Δt_l, ϵ_0 is the zeroth order error, A is the spatial/mass-wise convergence coefficient, p is the mass-wise convergence rate, B is the temporal convergence coefficient, q is the temporal convergence rate, C is the spatio- temporal convergence coefficient and r+s is the spatio-temporal convergence rate.

Our code verification for both planar and spherical cases consider the global mass-wise and temporal convergence separately.

6.3.2.0.1 Global mass-wise convergence analysis We employ the *ansatz* that the norm of the difference between the exact and computed solutions for the same time step Δt is

$$\| \xi^* - \xi_c \| = A(\Delta m)^p. \tag{6.12}$$

Since the exact solution ξ^* is unknown for the radiation hydrodynamics problem, we replace ξ^* by ξ_f where ξ_f is the value obtained for a very fine mesh ($\Delta m_f = \Delta m/\kappa^3$ and $\Delta m = \rho \Delta r$). The values ξ_m and ξ_i are also obtained for $\Delta m_m = \Delta m/\kappa$ and $\Delta m_i = \Delta m/\kappa^2$ respectively. Hence the mass-wise convergence rate p is obtained from the the following errors:

$$\| \xi_f - \xi_c \| = A(\Delta m)^p, \tag{6.13}$$

$$\| \xi_f - \xi_m \| = A(\Delta m/\kappa)^p, \tag{6.14}$$

$$\| \xi_f - \xi_i \| = A(\Delta m/\kappa^2)^p. \tag{6.15}$$

Applying logarithm to both sides and plotting the logarithm of the norm of the errors as a function of the logarithm of the mesh width, the slope of the line gives the mass-wise convergence

rate p.

$$\log \parallel \xi_f - \xi_c \parallel = \log A + p \ \log(\Delta m), \tag{6.16}$$

$$\log \parallel \xi_f - \xi_m \parallel = \log A + p \ \log(\Delta m/\kappa), \tag{6.17}$$

$$\log \parallel \xi_f - \xi_i \parallel = \log A + p \ \log(\Delta m/\kappa^2). \tag{6.18}$$

For N number of meshes, the L_1 norm is defined as

$\parallel \xi_2 - \xi_1 \parallel_1 = \Delta m \ \Sigma_{i=1}^{N} \mid \xi_2 - \xi_1 \mid$

and L_2 norm as

$\parallel \xi_2 - \xi_1 \parallel_2 = \sqrt{\Delta m \ \Sigma_{i=1}^{N} \mid \xi_2 - \xi_1 \mid^2}$.

6.3.2.0.2 Global temporal convergence analysis Similar to the mass-wise convergence analysis, the *ansatz* employed is that the norm of the difference between the exact and computed solutions for the same mass of the mesh Δm is

$\parallel \xi^* - \xi_c \parallel = \epsilon_m + B(\Delta t)^q$ where ϵ_m is the mass-wise error which dominates over the temporal error and hence needs to be accounted. However, the exact solution ξ^* being unknown, ξ^* is replaced by ξ_f where ξ_f is the value obtained for a very small time step ($\Delta t_f = \Delta t/\tau^3$). The values ξ_m and ξ_i are similarly obtained for $\Delta t_m = \Delta t/\tau$ and $\Delta t_i = \Delta t/\tau^2$ respectively. Replacing ξ^* by ξ_f, ϵ_m on the R.H.S. gets cancelled as all the variables $\xi_f, \xi_i, \xi_m, \xi_c$, etc., are obtained for the same value of mass of a mesh. Thus the temporal convergence rate q is obtained from the following equations:

$$\log \parallel \xi_f - \xi_c \parallel = \log B + q \ \log(\Delta t), \tag{6.19}$$

$$\log \parallel \xi_f - \xi_m \parallel = \log B + q \ \log(\Delta t/\tau), \tag{6.20}$$

$$\log \parallel \xi_f - \xi_i \parallel = \log B + q \ \log(\Delta t/\tau^2). \tag{6.21}$$

A plot of the logarithm of the L_1 and L_2 norms of the errors in total internal energy for

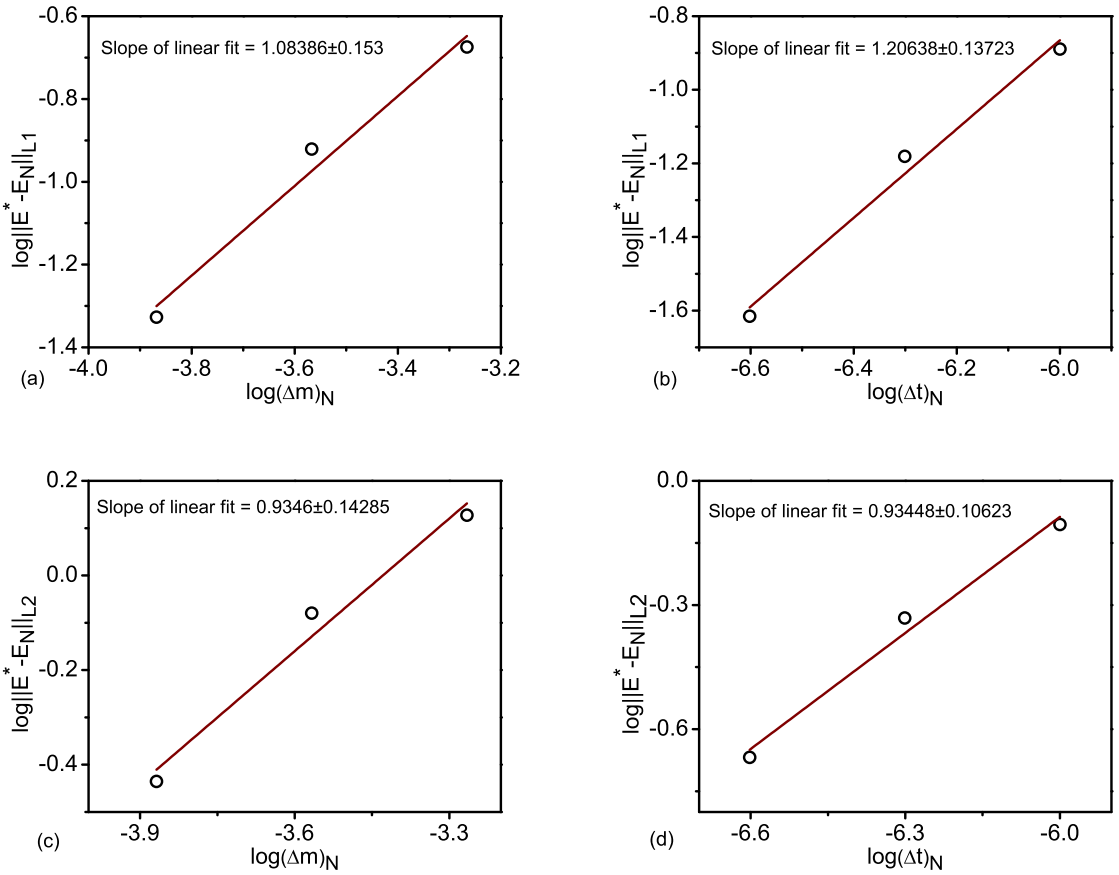

Figure 6.9: (a) Spatial convergence rate for the L_1 norm (b) Temporal convergence rate for the L_1 norm (c) Spatial convergence rate for the L_2 norm and (d) Temporal convergence rate for the L_2 norm obtained for the error in the thermodynamic variable internal energy (E) for the problem of shock propagation in Al foil.

both spatial/mass-wise and temporal convergence are shown in figure 6.9 for the problem of shock propagation in aluminium foil. In all the cases the convergence rates are $\simeq 1$ as expected from the discretization of the mass, momentum and energy conservation equations (as explained in the appendix). Similar convergence rates ($\simeq 1$) are observed for the other thermodynamic variables like velocity, pressure, density and temperature. Similarly, for the spherical case of point explosion problem with radiation transport, the spatial and temporal convergence rates are $\simeq 1$ for the L_1 norm as depicted for the total internal energy in figure 6.10.

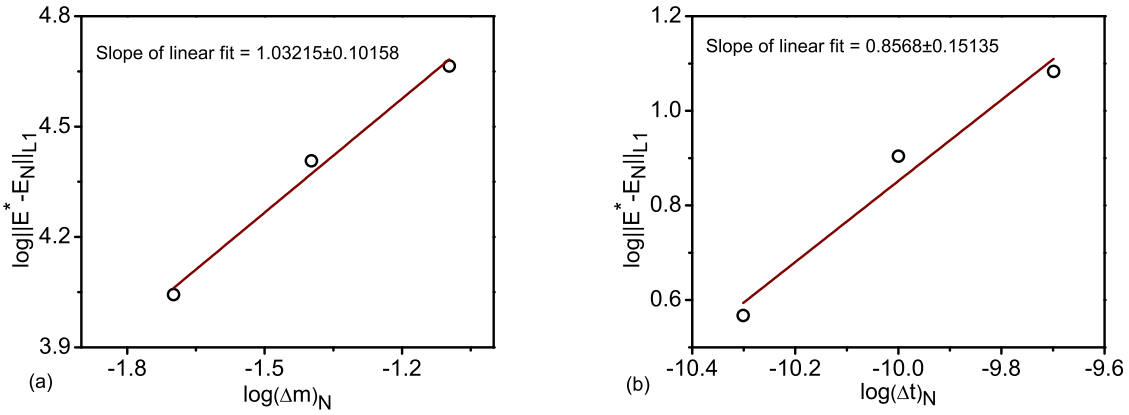

Figure 6.10: (a) Spatial and (b) Temporal convergence rate for the L_1 norm obtained for the error in the thermodynamic variable internal energy (E) for the problem of point explosion with radiation interaction (Total energy 235×10^{16} ergs is deposited).

6.3.3 Semi-implicit method

In the semi-implicit scheme, eqn. [5.5] is retained and $P_i^{1/2}$ is expressed as $P_i^{1/2} = (P_i + \tilde{P}_i)/2$ wherein $\tilde{P}_i$ is the pressure at the end of the time step. Starting with the previous time step values for $\tilde{P}_i$, the position and velocity of each mesh is obtained and $\tilde{P}_i$ is iteratively converged using the EOS. As the variables are obtained explicitly from the known values, there is no need to solve the tridiagonal system of equations for the velocities of all the meshes. Again, the energy flowing to the meshes as a result of radiation interaction is obtained by solving the transport equation once at the start of the time step, and hence the iterations leading to temperature convergence are absent.

The performance of the implicit and semi-implicit schemes are compared by studying the convergence properties and the CPU cost for the problem of shock wave propagation in aluminium. The convergence properties are examined by obtaining the absolute L_2-Error in the respective thermodynamic variable profile versus the fixed time step value. The absolute L_2-

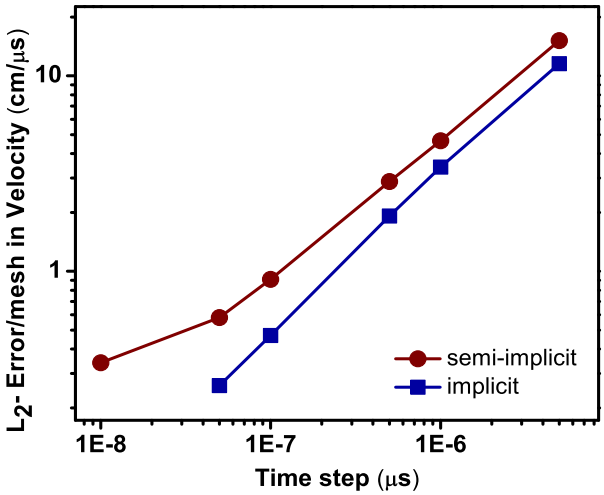

Figure 6.11: L_2-Error/mesh in velocity Vs. time step for the shock wave propagation problem in aluminium with $\Delta t/\Delta x = 5 \times 10^{-3}\ \mu\mathrm{s/cm}$. Convergence rate is higher for the implicit scheme.

Error in the variable f (velocity, pressure, density or temperature) is defined as

$$L_2\text{-Error} = [\sum_{j=1}^{N}(f_j - f_j^e)^2]^{1/2}, \tag{6.22}$$

where the data f_j^e constitute the exact solution for $\Delta t \longrightarrow 0$. The summation is taken over the values in all the meshes.

In figure 6.11. the L_2-Error per mesh for velocity i.e. $[\sum_{j=1}^{N}(f_j - f_j^e)^2/\text{number of meshes}]^{1/2}$, is plotted as a function of the time step by keeping the ratio of time step to mesh size i.e. $\Delta t/\Delta x$ constant at $5 \times 10^{-3} \mu s/cm$. As the solution of the implicit scheme is found to converge linearly, the results obtained from the implicit method using a small time step of $\Delta t = 10^{-8} \mu s$ and mesh width of 2×10^{-6} cm is chosen as the exact solution. Both the implicit and semi-implicit schemes show linear convergence, though the convergence rate is faster for the implicit scheme showing its superiority in obtaining higher accuracies.

Figure 6.12. shows that the faster convergence in the implicit method is attained at the cost

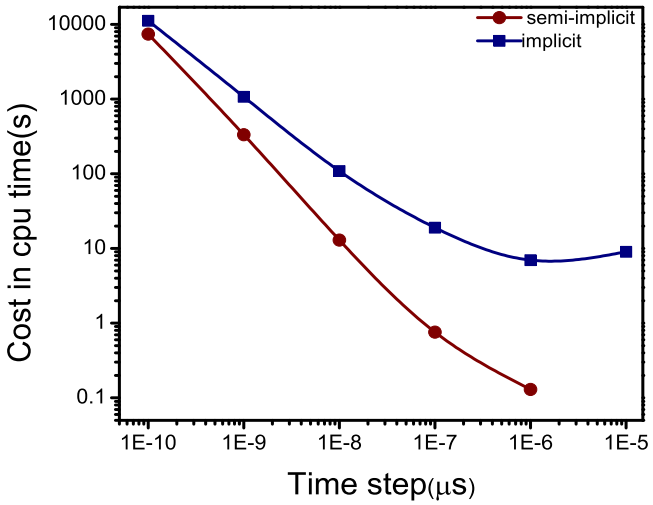

Figure 6.12: CPU cost Vs. time step for the shock wave propagation problem in aluminium with mesh width $\Delta x = 2 \times 10^{-4}$ cm.

of slightly higher CPU time. However the cost in CPU seconds become comparable in the two schemes for smaller time steps.

6.4 Summary

In this chapter, we have developed and studied the performance of fully implicit radiation hydrodynamics scheme. The time dependent radiation transport equation is solved and energy transfer to the medium is accounted exactly without invoking approximation methods. To validate the code, the results have been verified using the problem of shock propagation in aluminium foil in the planar geometry and the point explosion problem with heat conduction in the spherical geometry. The simulation results show good agreement with the theoretical solutions. For the purpose of verification, asymptotic convergence analysis is applied to both the problems of shock propagation in aluminium and the point explosion problem including full radiation transport. The temporal and mass-wise convergence rates are found to be $\simeq 1$ in agreement with

the fact that the thermodynamic variables velocity, pressure, density, temperature and internal energy have an error $O(\Delta m)$ for constant time steps and $O(\Delta t)$ for a fixed mesh width on discretizing the respective conservation equations. Convergence rate is higher for the implicit compared to the semi-implicit scheme. For larger time steps, more accurate results are obtained from the implicit method at the cost of higher CPU time.

7 Concluding remarks on this thesis

7.1 Summary and conclusions

In this thesis we have focussed on improving the present models for analyzing energy transport in partially and fully ionized plasmas. Considerable improvement has been made to the currently available energy deposition model of charged particles in ICF plasma. Inclusion of large angle Coulomb scattering, nuclear scattering and collective plasma effects are observed to affect the results. For both alpha particles and deuterons depositing energy in a fully ionized deuterium plasma, more energy is deposited to the ions thereby decreasing the thermalization distance, reducing the leakage probability and thus making ignition and burn more promising. This energy deposition model has been clubbed with the zero dimensional model for analyzing time development of a highly compressed and heated DT fusion pellet. Three separate cases have been considered.

Firstly, we reanalyze the problem of internal tritium breeding. As the fusion cross-section of D-T reaction is orders of magnitude higher than D-D at about 5 keV, presence of T in the fusion pellet helps in lowering the ignition temperature. It was found in the literature that a small fraction of T (x=0.0112) in the deuterium pellet acts as a catalyst and helps in reducing the ignition temperature. However the proper inclusion of all the loss mechanisms like Bremsstrahlung and inverse Compton scattering increased the density and temperature requirements and internal T

breeding was no more possible for the pellet considered. On using the detailed energy deposition model, multigroup treatment for neutron energy deposition and improved reactivity fits, we showed that for the same pellet parameters, internal T breeding is possible even on including all the loss mechanisms.

Secondly, we obtained optimum values of initial pellet density, temperature and fraction of tritium in the pellet for which internal tritium breeding occurs.

Thirdly, the fusion yields have been obtained for DT pellets having equal amounts of D and T for a wide range of densities and temperatures. Two separate schemes have been considered viz., volume and central ignition. For volume ignition, the zero-dimensional model produces results in agreement with those obtained in the literature using 1D Lagrangian code. We modified the zero dimensional model to study central ignition with only central 10% of the pellet at a high temperature. The central region expands at the thermal or detonation wave velocity against a pressure exerted by the outer cold fuel. Although the yields are found to be lower for the same initial temperature for central ignition, gains are higher above a certain density in comparison with volume ignition as expected.

Bremsstrahlung emission and absorption of radiation occurs due to free-free transitions of electrons in the vicinity of an atom or ion. In addition, bound-free and bound-bound transitions are also responsible for absorption and emission of photons in the medium. To properly account all these mechanisms in a partially ionized plasma, accurate fits for Rosseland opacities as a function of plasma densities and temperatures are supplied as input to the radiation transport equation coupled to the mass, momentum and energy conservation equations for the material. In order to obtain analytical solutions to the radiation transport equation, a few simplifying assumptions are made. The material is assumed to be static, opacity is temperature independent and the specific heat is proportional to the cube of the material temperature. The equations are linearized because of these assumptions. Analytical expression for radiation and material energy densities as a function of space and time are obtained for the finite planar slab, sphere

and spherical shell using both the Laplace transform and eigen function expansion method. These results, obtainable to the required degree of accuracy by adding more terms in the series solution, serve as new benchmark problems for time dependent radiation diffusion codes.

One dimensional codes are developed for hydrodynamics, radiation diffusion and transport simulation. Hydrodynamic simulation in performed in an implicit manner by obtaining the velocities of all the vertices at each time step. It is validated in all the three geometries using shock tube, point explosion and Noh problem. Radiation diffusion equation is next solved using the finite difference method and results generated for planar slab and spherical shell for which analytical results have been generated. Finally, radiation transport equation is solved using the discrete ordinates method and results generated for Marshak wave propagation in planar and spherical geometries.

Finally, implicit hydrodynamics program is coupled with radiation transport to obtain a fully-implicit 1D Lagrangian radiation hydrodynamic code. Results obtained for shock propagation in Al foil is found to agree well with the scaling law obtained from strong shock relations. For lower input energies, the position of the shock front and the heat front are found to coincide with those obtained both analytically and numerically for point explosion with heat conduction.

7.2 Limitations of this work

All the models, analytical solutions and codes have been developed in 1D which simplifies the problems considerably. In all cases, symmetry of the variables is assumed in the other two dimensions. This assumption may not be valid for practical systems so that 2D and 3D models need to be considered.

In the temperature and density regime that we consider, the plasma is non degenerate. We have not studied the effect of electron degeneracy which may arise in some cases relevant to ICF at very high densities and low temperatures.

Though we have qualitatively explained the reason for the heat front not moving ahead of the shock front in the transport formalism, a qualitative analysis of the same has not been performed.

The problem of shock propagation in Al foil performed with the radiation hydrodynamic code has been considered for incident temperatures below 300 eV. If more intense radiation ($>$ 1keV) is incident on the foil, more interesting phenomena like radiative shock propagation can be observed.

7.3 Future scope

The analytical derivations for finite systems can be extended to two or three dimensions using separation of variables along with the eigenfunction expansion method. Also, instead of a constant flux of radiation being incident on the surface, benchmarks can be generated for a time varying radiation pulse incident on finite systems. Writing implicit radiation hydrodynamic code in two and three dimension will be an useful extension of this work. Radiative shocks having separate ion and electron temperatures can be studied using the radiation hydrodynamics code by considering radiation pressure and momentum terms also. Mechanism of Rayleigh Taylor Instabilities can be studied using molecular dynamics simulation.

A Runge-Kutta method for solving the ODEs

Runge-Kutta methods are used for obtaining the solution of a single or a set of ordinary differential equations which achieve the accuracy of a Taylor series approach without requiring the calculation of higher derivatives [110]. In this method, the solution of an ordinary differential equation of the form

$$\frac{\mathrm{dy}}{\mathrm{dx}} = \mathrm{f}(\mathrm{x}, \mathrm{y}) \tag{A.1}$$

can be cast in the generalized form

$$\mathrm{y_{i+1}} = \mathrm{y_i} + \phi(\mathrm{x_i}, \mathrm{y_i}, \mathrm{h})\mathrm{h}, \tag{A.2}$$

where $\phi(\mathrm{x_i}, \mathrm{y_i}, \mathrm{h})$ is called an increment function, which can be interpreted as a representative slope over the interval. $\mathrm{y_{i+1}}$ and $\mathrm{y_i}$ are the new and old values of the unknown respectively. The increment function can be written in general form as

$$\phi = \mathrm{a_1 k_1} + \mathrm{a_2 k_2} + \ldots\ldots\ldots + \mathrm{a_n k_n}, \tag{A.3}$$

where the a's are constants and the k's are recurrence relationships

$$k_1 = f(x_i, y_i), \tag{A.4}$$

$$k_2 = f(x_i + p_1 h, y_i + q_{11} k_1 h), \tag{A.5}$$

$$k_3 = f(x_i + p_2 h, y_i + q_{21} k_1 h + q_{22} k_2 h), \tag{A.6}$$

$$k_n = f(x_i + p_{n-1} h, y_i + q_{n-1,1} k_1 h + q_{n-1,2} k_2 h + ... + q_{n-1,n-1} k_{n-1} h), \tag{A.7}$$

where the p's and q's are constants. By employing different number of terms n in the increment function, various types of Runge-Kutta methods can be devised. For n^{th}-order Runge-Kutta method, the values of a's, p's and q's are evaluated by setting eqn. [A.2] equal to terms in a Taylor series expansion. Fourth order Runge-Kutta methods are the most popular and as the result of the derivation contains less number of equations than the number of unknowns, an infinite number of versions are possible. The classical fourth-order RK method is the following:

$$y_{i+1} = y_i + \frac{1}{6}(k_1 + 2k_2 + 2k_3 + k_4)h \tag{A.8}$$

where

$$k_1 = f(x_i, y_i), \tag{A.9}$$

$$k_2 = f(x_i + \frac{1}{2}h, y_i + \frac{1}{2}k_1 h), \tag{A.10}$$

$$k_3 = f(x_i + \frac{1}{2}h, y_i + \frac{1}{2}k_2 h), \tag{A.11}$$

$$k_4 = f(x_i + h, y_i + k_3 h). \tag{A.12}$$

The graphical depiction of the slope estimates for the fourth order Runge-Kutta method are shown in figure A.1. For a system of n equations, n initial conditions are to be known at the starting value of x. The method presented above employs a constant step size h, however in the region of abrupt change the result would be inaccurate. The region of abrupt change requires small step size whereas the region of gradual change requires larger ones. This problem is

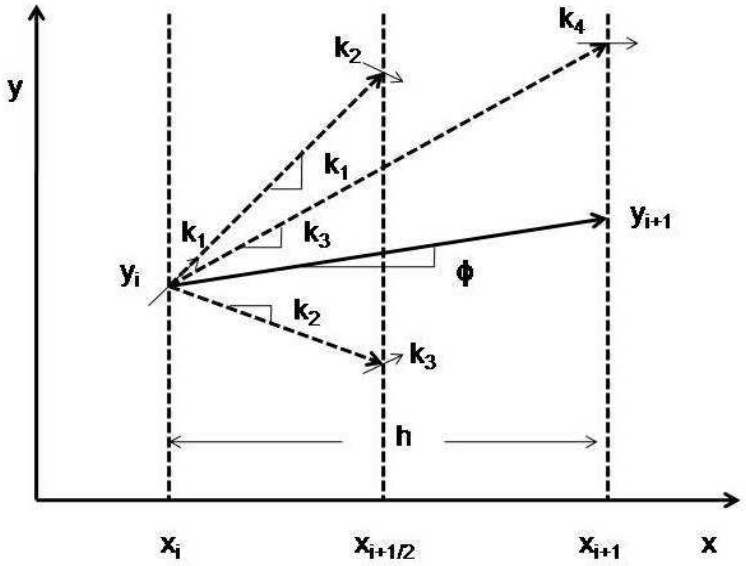

Figure A.1: Schematic of slopes for fourth order Runge Kutta Method.

overcome by obtaining an error estimate by computing two RK predictions of different orders. The Runge-Kutta Fehlberg or embedded RK method uses a fifth order RK method that employs the function evaluations from the accompanying fourth-order RK method.

B

Error arising from the discretization of mass, momentum and energy conservation equations

The position of a mesh at time t i.e., $\tilde{\mathrm{r}}_{\mathrm{i}}$ can be written in terms of the position at the previous time r_{i} by Taylor series expansion as

$$\tilde{\mathrm{r}}_{\mathrm{i}} = \mathrm{r}_{\mathrm{i}} + \mathrm{u}_{\mathrm{i}}\Delta\mathrm{t} + \frac{\mathrm{a}_{\mathrm{i}}(\Delta\mathrm{t})^2}{2} + \mathrm{O}(\Delta\mathrm{t})^3. \tag{B.1}$$

In the radiation hydrodynamics code, terms $\mathrm{O}(\Delta\mathrm{t})^2$ has been neglected in writing eqn. [5.2]. So, the error in position is $\mathrm{O}(\Delta\mathrm{t})^2$. Also, $\mathrm{u} = \frac{\mathrm{dr}}{\mathrm{dt}}$ and hence the error in velocity is $\mathrm{O}(\Delta\mathrm{t})$.

Similarly, in writing Eqs. 5.9 and 5.10, i.e the equation for conservation of mass in discrete form, since the gradient of velocity is written as a forward difference formula, the error in pressure is $\mathrm{O}(\Delta\mathrm{t})$ for a constant mesh width i.e., the temporal convergence rate $\simeq 1$ and $\mathrm{O}(\Delta\mathrm{m})$ for a constant time step, i.e., the spatial/mass-wise convergence rate $\simeq 1$. From the discrete form of the energy equations, i.e., eqn. [6.2], etc., it is observed that the temporal error in internal energy is $\mathrm{O}(\Delta\mathrm{t})$ and mass-wise error is $\mathrm{O}(\Delta\mathrm{m})$.

C

Melting curve of metals using classical molecular dynamics simulations

The melting curves of Cu and Al have been generated using one-phase classical molecular dynamics simulation employing the parallel molecular dynamics simulation package $\mathrm{DL\_POLY}$ [111] together with the crystalline and molecular structure visualisation program XCrySDen [112]. The embedded atom method potential of Cai and Ye has been used to account for the interactions between atoms [47]. We consider cubic super cells consisting of $11 \times 11 \times 11$ conventional FCC unit cells, which corresponds to 5324 atoms. Three dimensional parallelopiped periodic boundary conditions are applied on the super cells to eliminate the surface effects and reproduce the bulk properties. The Berendsen isothermal-isobaric (NPT) ensemble is used to achieve constant temperature and pressure conditions [113]. The relaxation times for the thermostat and barostat are 1.0 and 3.0 ps, respectively, and the pressure is fixed at 0 atm. We use the Verlet leapfrog scheme for integrating the Newton's equations of motion [114] with a time step of 0.001 ps for all cases. Simulations are done for a total of 10,000 time steps, where the first 4000 steps are used for equilibration and the remaining 6000 for statistical averaging. In order to ascertain that only one image of a particle interacts with another particle, the cut off distances for force calculations is chosen to be smaller than half the size of the supercell. A cutoff distance of 10Å is used for all the simulations. The melting curves obtained for Cu and Al using MD simulations are plotted in figure C.1 and figure C.2 respectively.

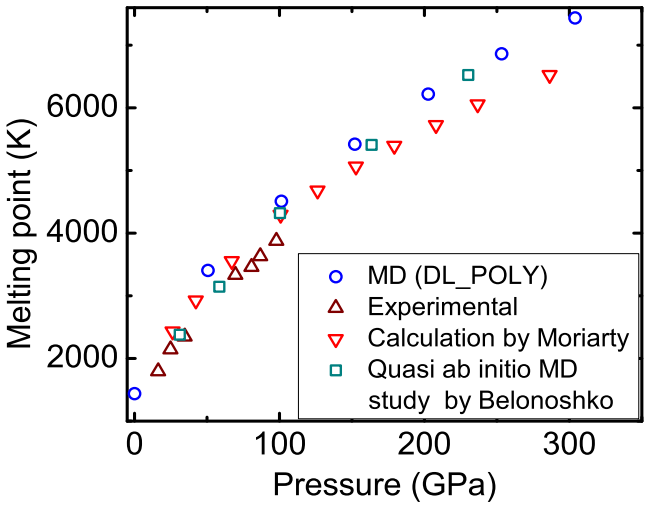

Figure C.1: Melting curve for Cu.

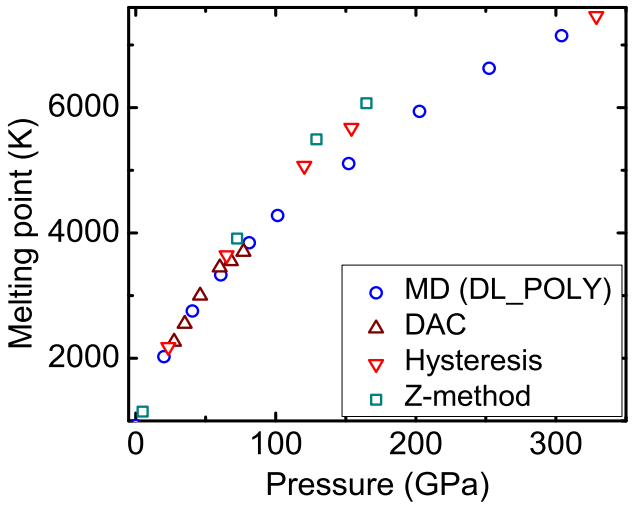

Figure C.2: Melting curve for Al.

The melting curve obtained from our MD simulation for Cu is found to agree well with the quasi ab initio MD study by Belonoshko [49]. Belonoshko *et al* have investigated the melting point of Cu using MD simulation employing the Sutton-Chen model for the interatomic interaction. This interaction has been fitted to reproduce results from first-principles self-consistent total-energy calculations within the local-density approximation using the full potential linear-muffin-tin-orbital method. The melting points obtained by Moriarty [115] using ab initio calculations agree well upto 100 GPa pressures and there is good agreement with the experimentally obtained laser-heated diamond cell results [116]. The steep slope of Cu confirms the key role of d-shell electrons in determining the temperature dependence of high pressure melting curve. The melting curve for Al agrees well with the experimental DAC [117] results. The results obtained from ab initio MD using the hysteresis and the Z-method [118] are found to be slightly higher at higher pressures. The results obtained for both the metals agree well with Diamond Anvil Cell and with ab initio MD simulation results like the hysteresis or Z-method.

D Role of site-selective doping on melting point of CuTi alloys: A classical molecular dynamics simulation study

D.0.1 Introduction

Effect of site-selective substitution of Ti in Cu on the thermal stability of CuTi alloy is investigated using classical molecular dynamics simulations with Embedded Atom Method potentials. It has been observed experimentally that melting point of all the naturally occurring stable phases of CuTi alloys do not show a definite trend with gradual increase in Ti concentration. To understand the phenomenon, super cells of CuTi alloy are constructed where Cu atom is substituted by Ti randomly and at selective sites. For random substitution, the melting point decreases linearly with increase in Ti concentration. A non-monotonous dependence is seen when Cu atoms at selective sites are replaced by Ti. For a particular doping concentration, the melting point shows a wide range of variation depending on the order of atomic arrangement, and can be fine tuned by selecting the sites for substitution. The variations in melting points in different cases are explained in terms of the peak height, width and position of the corresponding radial distribution functions. Finally, it is verified that initial structures of the naturally occurring CuTi alloys are responsible for the non-definite trend in their melting points.

Melting point of simple metal alloys (AB-type intermetallic compounds) is roughly equal to

the average of the melting points of the constituent elements [119]. But a number of transition metal alloys tend to have melting points below the averaged elemental melting points and no strong correlation with elemental variables such as heats of formation of the alloy or volume changes upon alloying is found [119]. In this work, thermal stability of CuTi alloys has been linked with local environment of the host and dopant atoms and the characteristics of the radial distribution function (RDF) are employed to address certain irregularities in the existing phase diagram. The cell volume of some alloys increases compared to that in its pure phase due to the larger radius of the dopant atoms. Melting point of these alloys decrease if the melt occupies larger volume than its solid phase. CuTi alloy belongs to this category and the melting point of CuTi alloy should decrease as Ti concentration increases. But the phase diagram of CuTi alloy shows decrease in melting point, from 1356 K to 1158 K, on alloying by Ti only below a certain concentration (20 % in $\mathrm{Cu_4Ti}$) [120]. Beyond this limit, stable phases are found at much elevated temperatures. Melting point gradually increases from 1158 K to 1273 K as the Ti concentration increases for stable phases like $\mathrm{Cu_2Ti}$, $\mathrm{Cu_3Ti_2}$, $\mathrm{Cu_4Ti_3}$ and CuTi (50 %). Therefore linear dependence of melting point on Ti concentration is not observed. This anomaly in the melting curve can be explained by performing simulations on thermal stability of CuTi alloy having various arrangements of dopant atoms.

Structures of CuTi alloys having different Ti concentrations have been generated by random or selective substitution of Ti in perfect fcc Cu supercells. The origin of the cartesian coordinate system is taken to be the centre of the supercell. The perfect fcc Cu supercell is generated using the program genlat.f in utility of $\mathrm{DL\_POLY}$. The Cu atoms are placed one after the other starting from the (-,-,-) octant towards the (+,+,+) octant.

For random doping of Cu atoms with Ti, random numbers (depending on the concentration) lying within the supercells are generated for x, y and z coordinates. The Cu atom whose coordinates are nearest to the random numbers are replaced by Ti atoms. The initial configurations generated for 5 % and 25 % Ti (number percentages) are shown in figure D.1 (a) and (b)

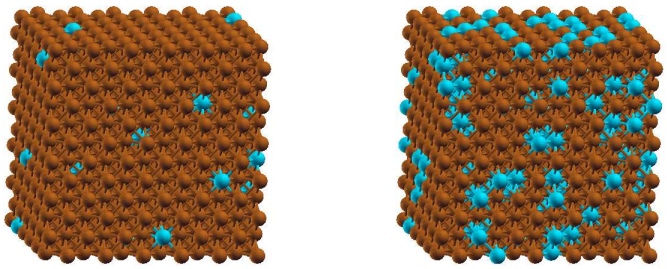

Figure D.1: Random doping of Cu with (a) 5% and (b) 25% Ti.

respectively.

Microstructures of Ti having various sizes are also generated within the Cu supercells. Single microstructures of different concentrations are generated by replacing all the Cu atoms with Ti atoms inside spheres of varying radii at the centre of the microstructures i.e., (0,0,0). figure D.2 (a) shows the negative octant of the supercell with single microstructure doping of 5.5973% Ti in Cu. For substituting 8 microstructures, all Cu atoms lying within spheres of different radii centered at (-L,-L,-L), (-L,-L,+L), (-L,+L,-L), (+L,-L,-L), (-L,+L,+L), (+L,-L,+L), (+L,+L,-L) and (+L,+L,+L) with L=10.845Å are replaced by Ti atoms. Similarly, 9 microstructures are obtained by replacing the Cu atoms within the sphere at the origin in addition to the spheres used for 8 microstructures (figure D.2 (b)).

Selective doping is done in a variety of ways: For a concentration of 5 % Ti, first Cu atom among every 20 atoms is replaced by Ti till all the 5324 atoms are covered. The selectively doped CuTi alloy generated in this way is called selective 5 % atom1. Similarly for a concentration of 10 % Ti, first Cu atom among every 10 atoms is replaced by Ti. This alloy is named as selective 10 % atom1. A type named atom2 is generated by replacing 2 atoms at a time. So, for a concentration of 5 % Ti, first two Cu atoms among every 40 atoms are replaced by Ti. Thus, selective 33.33 % atom1 is generated by replacing first among every 3 Cu atoms with Ti and selective 33.33 % atom6 by replacing first six among every 18 Cu atoms with Ti. Selective

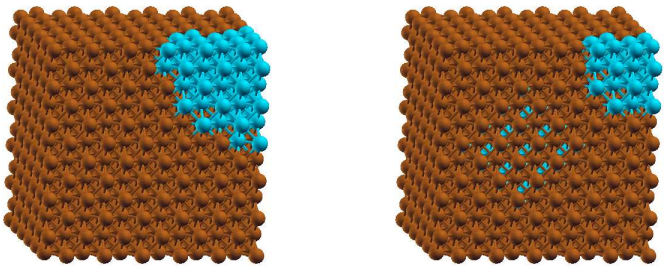

Figure D.2: Negative octant of supercell with (a) single microstructure of 5.5973% Ti and (b) 9 microstructures of Ti, each of radius 7 Å with 19.6% Ti.

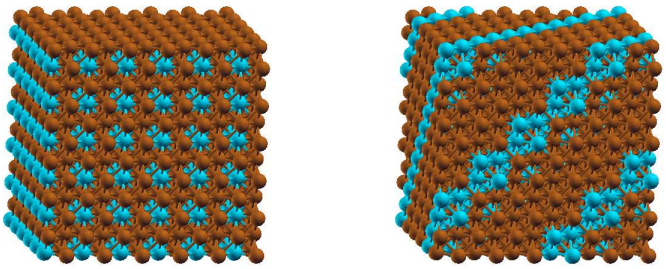

Figure D.3: Selective doping of Cu with 25% Ti for two Ti-arrangements, namely, (a) atom1 and (b) atom4.

25% atom1 and atom4 are shown in figure D.3 (a) and (b) respectively.

The natural CuTi alloy structures, viz. CuTi [121] and $CuTi_2$ [122] are also generated using the program genlat.f. The number of atoms of Cu and Ti and their positions within the unit cells are obtained from ICSD database [123](file no. 103128 for CuTi and 15807 for $CuTi_2$). The EAM potential by Hong has been used for simulating the CuTi alloy [124].

D.0.2 Results and Discussions

D.0.2.1 Random doping

The melting temperature for Cu is reported as 1200K in an earlier study employing $\mathrm{DL\_POLY}$ with Sutton Chen potential [48]. However, we get 1340 K which agrees better with the experimental result of 1356K. For random doping, melting point decreases linearly as Ti concentration increases. Since the atomic radius of Ti (2 $\mathrm{\AA}$) is higher than that of Cu (1.57 $\mathrm{\AA}$), cell volume increases when a Ti atom replaces a Cu atom. The increase in lattice parameter of the CuTi alloy is found to obey the empirical Vegard's law, which, for a given temperature, is a linear relation between lattice constant and concentration of the constituent elements [125] (see figure D.4). As a result, the average distance between Cu atoms increases and the Cu-Cu bond strength decreases. This is clearly reflected in figure D.5 which shows the 0K RDF for the Cu-Cu bond. It is observed that the heights of the RDF peaks decrease, full widths at half maxima (FWHM) increase and the peak positions shift to the right. As mentioned earlier, decrease in RDF peak height is directly linked to the reduction in number of nearest neighbours. Also, increase in cell volume leads to shifting of RDF peak to the right. Thus for random doping, the average Cu-Cu bond strength and hence melting point decreases linearly as dopant concentration increases (inset of figure D.5).

D.0.2.2 Microstructural doping

For most of the practical cases, doping of clusters of several atoms is more probable compared to atom by atom substitution. Therefore, micro-structures of several Ti atoms are created within the Cu lattice. For a single microstructure, the Cu-Cu bond strength decreases linearly with increase in Ti concentration as shown in figureD.6. This is also reflected in the linear decrease of melting point (inset of figure D.6). Similarly, for 8 microstructure doping, the RDF peak height decreases linearly (figure D.7) and a gradual decrease in melting point is observed (see

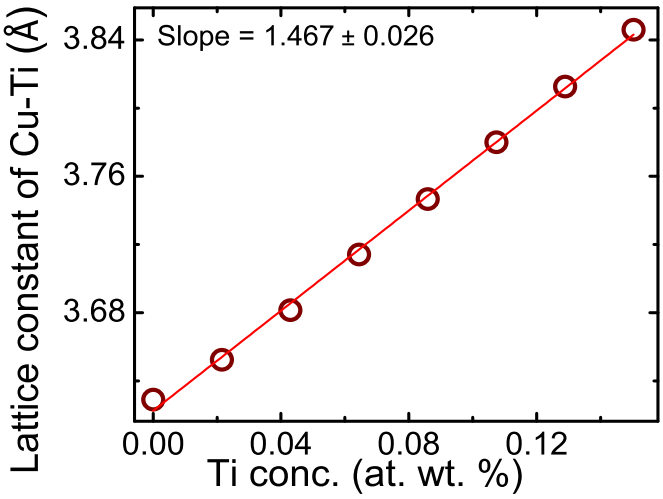

Figure D.4: Linear variation of the lattice parameter as a function of the atomic weight percent of the dopant Ti in Cu.

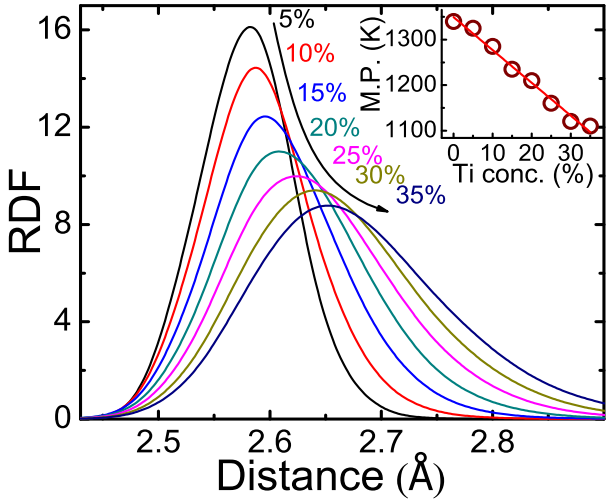

Figure D.5: RDFs for Cu-Cu bond in the case of random doping of Cu with Ti. Inset shows linear variation in melting point (M.P.) as a function of the number percent of the dopant Ti in Cu.

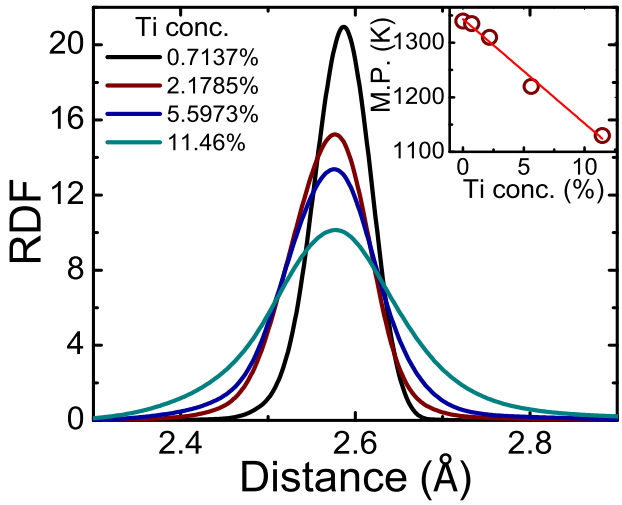

Figure D.6: RDFs for Cu-Cu bond in case of single microstructure doping of Cu with Ti. Inset shows linear variation in melting point as a function of the number percent of the dopant Ti in Cu.

inset of figure D.7). Exactly similar trends are observed for 9 microstructure doping.

D.0.2.3 Selective doping

The systematic variation in melting point on changing the Ti concentration as observed for random and microstructural doping is no longer seen in case of selective dopant substitution. Both dopant concentration and the site of substitution are responsible for determining the melting point of the alloy. As already pointed out, Ti atoms can be introduced into Cu lattice in various ways to generate different atomic arrangements having the same dopant concentration. When a Ti atom replaces a single Cu atom in a unit (atom1), melting point decreases with Ti concentration up to 20 % as in the case of random substitution (inset of figure D.8). Then the melting point increases for 25% Ti. As shown in figure D.8, upto 20 % Ti concentration, the height of the first RDF peak decreases, become broader and position shifts to the right showing a loss in symmetry of the structure. But for 25% of Ti concentration, the first RDF peak becomes narrower and attains its maximum value. Its position does not shift further indicating stronger Cu-Cu bonding

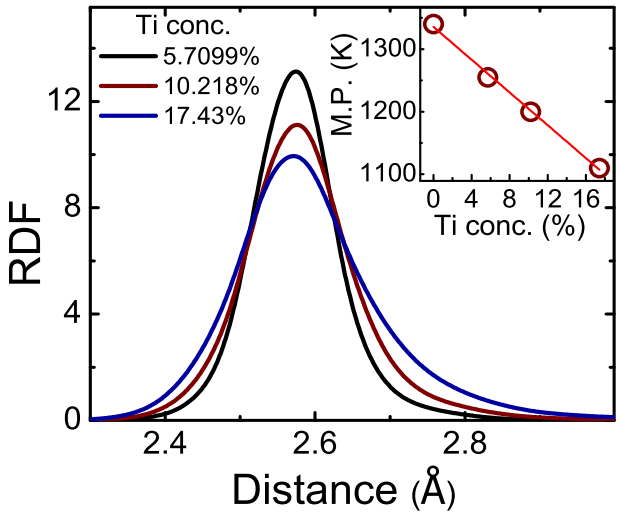

Figure D.7: RDFs for Cu-Cu bond in case of 8 microstructure doping of Cu with Ti. Inset shows linear variation in melting point as a function of the number percent of the dopant Ti in Cu.

for the structure as compared to 20 % Ti. Therefore, high melting point observed in case of 25 % atom1 case can be understood in terms of the height, width and position of the RDF peak. In a similar manner, the low melting point found in case of 33.33 % atom1 case can be understood by the loss in Cu-Cu bond strength which is clearly evident from the corresponding short and broad RDF peak. Finally, peak height increases and becomes narrower for 50 % Ti which results in increase in melting point. Similar kind of non-monotonous behaviour of melting point with dopant concentration can be seen for selective atom2 to atom6 cases. Only the late rise in melting point can be seen for different dopant concentration depending on the initial atomic arrangement.

The correlation between the melting point and characteristics of the RDF peak established here is important for the following reason. For an alloy it is necessary to quantify the interaction between the host atoms as well as between the host and dopant atoms. Especially, at higher temperatures when atoms may be displaced from their equilibrium positions, characteristics of the RDF peaks can predict the symmetry of the atomic configuration and the thermal behaviour

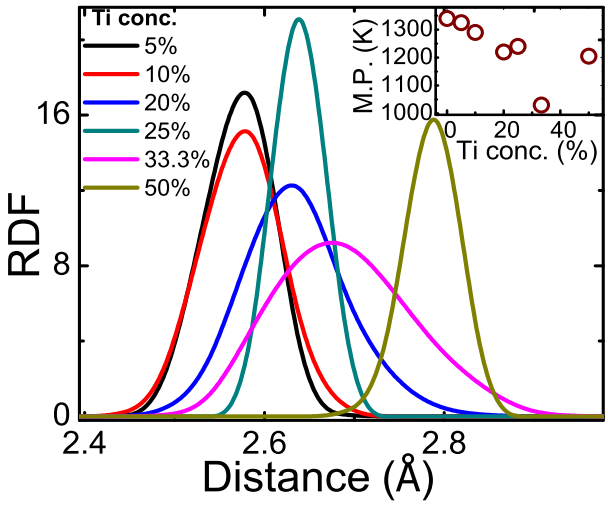

Figure D.8: RDFs for Cu-Cu bond in case of selective doping of Cu with Ti (atom1). Inset shows variation in melting points as a function of the number percent of the dopant Ti in Cu.

of the alloy.

The role of site selective doping on thermal stability can be unequivocally established if melting point is shown to change for different arrangement of dopant atoms but having same concentration. For that purpose, six different configurations of 25% doped CuTi alloy having different arrangements of Ti atoms in Cu lattice are constructed. Variation of the melting point for different Ti arrangements is depicted in the inset of figure D.9. The first, second and third Cu-Cu RDF peaks for four arrangements, namely, atom1, atom2, atom4 and atom6 are shown in figure D.9. The melting point is seen to decrease upto atom4 and then increases for atom5 and atom6. The height of the first RDF peak also decreases upto atom4 showing a loss in symmetry of the structure. However, for atom6, the RDF peak height increases and shifts to the left showing a more compact structure thus explaining the increase in melting point.

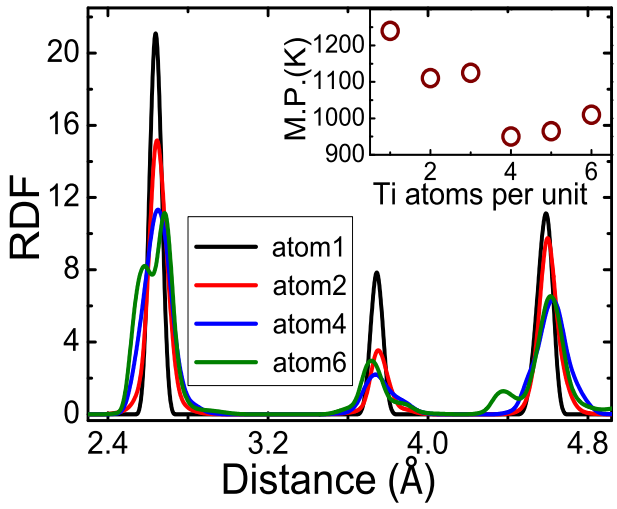

Figure D.9: First three peaks of the Cu-Cu RDF for selective substitutional doping of Cu with 25% Ti doping. Inset shows variation in melting points for different Ti arrangements having 25% Ti concentration.

Finally, we plot the melting points against dopant concentration for different ways of doping, namely, random, microstructural and selective doping (figure D.10). For random, single, 8 and 9 microstructures, linear variation of melting point on Ti concentration is observed. However, in case of microstructural doping, the melting points decrease faster compared to random doping. Selective doping (atom1), on the other hand, does not show the linear variation and the melting point depends on the initial structure irrespective of the concentration.

D.0.2.4 Natural CuTi alloys

The link established so far, between melting points and characteristics of the RDF peaks of an alloy, can be employed to understand the observed anomaly in the melting curve of naturally existing phases of CuTi alloys. Melting point as extracted from the phase diagram of CuTi alloy show non-monotonous dependence on Ti concentration. In the inset of figure D.11, the calculated melting points of Cu and two of its naturally occurring alloys viz. CuTi and $CuTi_2$

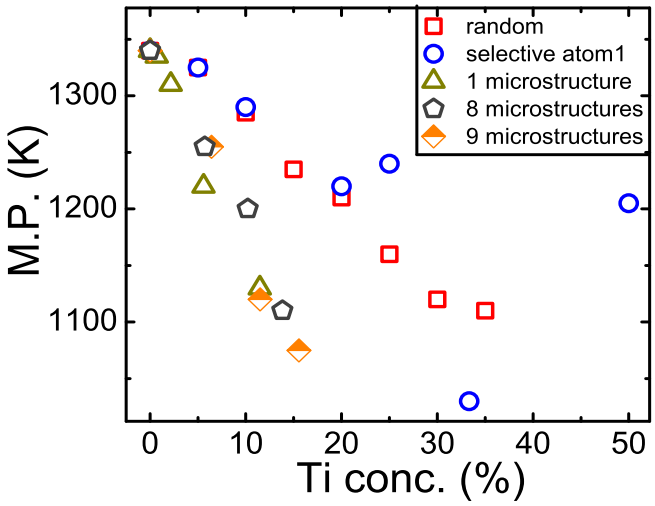

Figure D.10: Melting points obtained for different types of substitutional doping of Cu with Ti.

are plotted and the corresponding RDF peaks are shown in figure D.11. In line with the experimental phase diagram, melting point Vs. Ti concentration first decreases and then again increases. For example, substantial reduction in the melting point of naturally occuring CuTi alloy (1210 K) is seen compared to pure Cu (1340 K). Melting point of $CuTi_2$ increases to 1360K for 66.6 % doping (see inset of figure D.11). The late rise in melting point with the increase of Ti concentration arises due to higher ordering between the atoms in $CuTi_2$ (I4/mmm) than CuTi (P4/nmmS) . This is reflected on the Cu-Cu bond strength which can be visualized by the reduced RDF peak height of CuTi compared to pure Cu. As expected, RDF peak height of $CuTi_2$ increases which explains its observed higher melting point.

D.0.3 Conclusions

In summary, the role of site-selective substitution of Ti in Cu on the melting point of CuTi alloy has been investigated. Super cells of CuTi alloy having different arrangement of Ti atoms are constructed. Results obtained by replacing Cu atoms by Ti randomly, selectively and in the

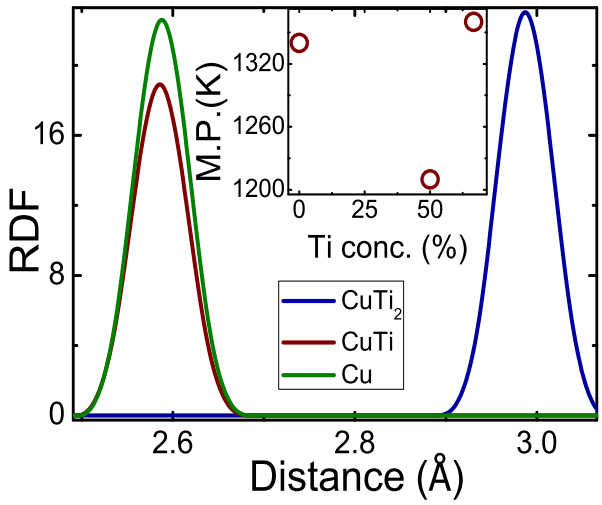

Figure D.11: First Cu-Cu RDF peaks for natural phases of CuTi alloy. Inset shows variation in melting point.

form of clusters are analyzed. We have established that, in addition to the concentration, the arrangement of dopant atoms in the host lattice plays a pivotal role in determining the melting point. A direct link between the melting point and characteristics of the RDF peaks of the alloy has been established. This facilitates to explain the variation in thermal stability in terms of the bond strength between host as well as host and dopant atoms in the alloy. The proposition has been validated by explaining the anomaly in the melting curve seen in naturally occurring phases of CuTi alloys having different crystal structures. The present study can be extended to other alloys of its kind and is useful for predicting doping strategies for fabrication of the alloy.

Bibliography

[1] R. Paul Drake 2006 *High-Energy-Density Physics, Fundamentals, Inertial Fusion and Experimental Astrophysics* Chapter 7 (Springer-Verlag, Berlin Heidelberg) ISBN-10 3-540-29314-0

[2] R. G. McClarren and J. G. Wohlbier 2011 *J. Quant. Spectrosc. Radiat. Transf.* **112** 119

[3] J. J. Duderstadt and G. A. Moses 1982 *Inertial Confinement Fusion* (John Wiley and Sons)

[4] Y. B. Zeldovich and Y. P. Raizer 1966 *Physics of Shock Waves and High-Temperature Hydrodynamic Phenomena*, Vols I and II (Academic Press, New York)

[5] A. B. Wollaber 2008 *Advanced Monte Carlo Methods for Thermal Radiation Transport* (A PhD Thesis in the University of Michigan)

[6] G. C. Pomraning 1973 *The Equations of Radiation Hydrodynamics. 1st ed. Oxford: Pergamon Press* Ch.III, 50-105

[7] D. Mihalas and B. W. Mihalas 1984 *Foundations of Radiation Hydrodynamics, Oxford University Press, New York* Ch.VI, 309-385

[8] S. Pfalzner 2006 *An Introduction to Inertial Confinement Fusion* (Taylor and Francis)

[9] S. Atzeni and J. Meyer-ter-vehn 2004 *The Physics of Inertial Fusion* (Oxford: Clarendon Press)

[10] J. Badziak, G. Mishra, N. K. Gupta and A. R. Holkundkar 2011 *Phys. Plasmas* **18** 053108

[11] N. K. Gupta and S. V. Lawande 1989 *Laser and Particle Beams* **7** 27

[12] N. K. Gupta and S. V. Lawande 1986 *Phys. Rev. A* **33** 2813

[13] N. K. Gupta and S. V. Lawande 1986 *Plasma Phys. Controlled Fusion* **28** 925

[14] L. Ensman 1994 *Astrophys. J.* **424** 275

[15] G. A. Sod 1978 *J. Comput. Phys.* **27** 1

[16] L.I.Sedov 1959 *Similarity and Dimensional Methods in Mechanics* (Gostekhizdat, Moscow, 4 th edition 1957. English transl. (M.Holt, ed.), Academic Press, New York)

[17] W. F. Noh 1978 *J. Comput. Phys.* **72** 78

[18] G. D. Smith 1969 *Numerical Solution of Partial Differential Equations* Oxford University Press, London

[19] E. A. Dorfi, H. Pikall, A. Stokl and A. Gautschy 2006 *Comp. Phys. Commun.* **174** 771

[20] R. Kippenhahn, A. Wiegert and E. Hofmeister 1967 *Methods. Comput. Phys.* **7** 129

[21] R. D. Richtmyer and K. W. Morton 1967 *Difference Methods for Initial Value Problems* Interscience, New York

[22] J. Von Neumann and R. D. Richtmyer 1950 *J. Appl. Phys.* **21** 232

[23] S. K. Godunov 1959 *Mat. Sbornik* **47** 271

[24] B. Einfeldt 1988 *SIAM J. Numer. Anal.* **25** 294

[25] N. K. Gupta, C. D. Munz and B. Goel 1990 *Laser and Particle Beams* **8** 807

[26] E. E. Lewis and W. F. Miller, Jr. 1984 *Computational Methods of Neutron Transport*, (John Wiley and Sons, New York)

[27] M. Y. Kim, S. Menon and S. W. Baek 2010 *Int. J. Heat Mass Transfer* **53** 5682

[28] J. A. Fleck Jr. and J. D. Cummings 1971 *J. Comput. Phys.* **8** 313

[29] J. D. Densmore 2006 *Ann. Nucl. Energy* **33** 343

[30] K. J. Connolly, F. Rahnema and D. Zhang 2012 *Ann. Nucl. Energy* **42** 1

[31] E. P. Shettle and J. A. Weinman 1970 *J. Atmos. Sci.* **27** 1048

[32] R. J. Goldstein *et al* 2010 *Int. J. Heat Mass Transfer* **53** 4397

[33] W. Dai and P. R. Woodward 1998 *J. Comput. Phys.* **142** 182

[34] D. A. Knoll, W. J. Rider and G. L. Olson 2001 *J. Quant. Spectrosc. Radiat. Transf.* **70** 25

[35] C. C. Ober and J. N. Shadid 2005 *J. Comput. Phys.* **195** 743

[36] A. Liemert and A. Kienle 2012 *J. Quant. Spectrosc. Radiat. Transf.* **113** 559

[37] H. Salt 1983 *Int. J. Heat Mass Transfer* **26** 1611

[38] A. Haji-Sheikh and J. V. Beck 2002 *Int. J. Heat Mass Transfer* **45** 1865

[39] X. Lu, P. Tervola and M. Viljanen 2005 *J. Phys. A: Math. Gen.* **38** 2873

[40] S. Eliezer, A. Ghatak and H. Hora 2002 *Fundamentals of Equations of State* (World Scientific: Singapore)

[41] R. M. More ,K. H. Warren, D. A. Young and G. B. Zimmerman 1988 *Phys. Fluids* **31** 3059

[42] D. K. Bradley *et al* 2009 *Physics of Plasmas* **16** 042703

[43] M. P. Allen and D. J. Tildesley 1989 *Computer Simulation of Liquids* (Oxford: Calendon Press)

[44] M. Griebel, S. Knapek and G. Zumbusch 2007 *Numerical Simulation in Molecular Dynamics*, Springer-Verlag Berlin Heidelberg

[45] J. M. Holender 1990 *J. Phys.:Condensed Matter* **2** 1291

[46] M .S. Daw and M. I. Baskes 1984 *Phys. Rev.* B **29** 6443

[47] J. Cai and Y. Y. Ye 1996 *Phys. Rev.* B **54** 8398

[48] Y. Mitrokhin 2006 *Comp.Mater.Sci.* **36** 189

[49] A. B. Belonoshko, A. Rosengren, L. Burakovsky, D. L. Preston and B. Johansson 2009 *Phys.Rev.* B **79** 220102(R)

[50] E. Nardi and Z. Zinamon 1978 *Phys. Rev.* A **18** 1246

[51] D. H. H. Hoffmann, K. Weyrich, H. Wahl, D. Gardes, R. Bimbot and C. Fleurier 1990 *Phys. Rev.* A **42** 2313

[52] S. Eliezer, Z. Henis and J. M. Martinez-val 1997 *Nucl.Fusion* **37** 985

[53] O. N. Krokhin and V. B. Rozanov 1973 *Soviet Journal of Quantum Electronics* **2** 393

[54] R. S. Cooper and F. Evans 1975 *Phys. Fluids* **18** 332

[55] S. Eliezer, Z. Henis, J. M. Martinez-val and I. Vorbeichik 2000 *Nucl.Fusion* **40** 195

[56] N. A. Tahir and D. H. H. Hoffmann 1998 *Fusion Technology* **33** 164

[57] A. Gsponer and J. P. Hurni 1999 *Phys. Lett.* A **253** 119

[58] S. Eliezer, Z. Henis, J. M. Martinez-val and M. Piera 1998 *Phys. Lett.* A **243** 311

[59] L. Spitzer Jr. 1956 *Physics of Fully Ionized Gases* (Interscience Publishers, Inc., New York)

[60] G. S. Fraley *et al* 1974 *Phys. Fluids* **17** 474

[61] R. E. Marshak 1958 *Phys. Fluids* **1** 24

[62] W. Kass and M. O'Keeffe 1966 *J. Appl. Phys.* **37** 2377

[63] G. C. Pomraning 1979 *J. Quant. Spectrosc. Radiat. Transf.* **21** 249

[64] B. Su and G. L. Olson 1996 *J. Quant. Spectrosc. Radiat. Transf.* **56** 337

[65] B. D. Ganapol and G. C. Pomraning 1983 *J. Quant. Spectrosc. Radiat. Transf.* **29** 311

[66] B. Su and G. L. Olson 1997 *Ann. Nucl. Energy* **24** 1035

[67] B. Su and G. L. Olson 1999 *J. Quant. Spectrosc. Radiat. Transf.* **62** 279

[68] M. M. R. Williams 2005 *Ann. Nucl. Energy* **32** 1047

[69] K. R. Olson and D. L. Henderson 2004 *Ann. Nucl. Energy* **31** 1495

[70] D.Mihalas and B.W.Mihalas 1984 *Foundations of Radiation Hydrodynamics* (Oxford Univ.Press, New York)

[71] W.Dai and P.R.Woodward 1998 *J.Comput.Phys.* **142** 182

[72] J.W.Bates, *et al* 2001 *J.Comput.Phys.* **167** 99

[73] W.Dai and P.R.Woodward 2000 *J.Comput.Phys.* **157** 199

[74] D. de Niem, E. Kuhrt and U. Motschmann 2007 *Comput. Phys. Commun.* **176** 170(2007)

[75] E. F. Toro 1997 *Riemann Solvers and Numerical Methods for Fluid Dynamics* (Springer-Verlag, Berlin/New York)

[76] P. Reinicke and J. Meyer-ter-Vehn 1991 *Phys. Fluids A* **3** 1807

[77] A. I. Shestakov 1999 *Phys. Fluids* **11** 1091

[78] J. R. Kamm, W. J. Rider and J. S. Brock 2004 *Consistent Metrics for Code Verification, Los Alamos National Laboratory*, **LA-UR-02-3794**

[79] D. A. Knoll, *et al* 2003 *J. Comput. Phys.* **185** 583

[80] D. J. Sigmar and G. Joyce 1971 *Nucl. Fusion* **11** 447

[81] C. K. Li and R. D. Petrasso 1993 *Phys. Rev. Lett.* **70** 3063

[82] C. K. Li and R. D. Petrasso 1993 *Phys. Rev. Lett.* **70** 3059

[83] F. Evans 1973 *Phys. Fluids* **16** 1011

[84] J. D. Jackson 1975 *Classical Electrodynamics* (Wiley, New York), Chap.13

[85] J. J. Devaney and m. L. Stein 1971 *Nuclear Science And Engineering* **46** 323

[86] S. Glasstone and A. Sesonske 1994 *Nuclear Reactor Engineering* Vol-1, Chapman and Hall, Inc., New York

[87] K. M. Case, F. D. Hoffmann and G. Placzek 1953 *Introduction to the Theory of Neutron Diffusion-I* (Los Alamos Scientific Laboratory)

[88] R. J. Barrett and R. E. MacFarlane 1979 *Coupled neutron-photon cross-section for transport calculations* LA-7808-MS

[89] R. Feldbacher 1987 *Alternate Physics Program Datalib*,Rep. NDC(ANS)-12/G,Tech. Univ. of Grad

[90] J. D. Huba 2006 *NRL Plasma Formulary* (Washington: Naval Research Lab.) 35

[91] S. Eliezer, P. T. Leon, J. M. Martinez-Val and D. V. Fisher 2003 *Laser and Particle Beams* **21** 599

[92] P. T. Leon, S. Eliezer, M. Piera and J. M. Martinez-Val 2005 *Laser and Particle Beams* **23** 193

[93] J. J. Honrubia 1993 *Nucl. Fusion by Inertial Confinement* (Velarde G.,Roney Y., Martinez-Val J., Eds)(Boca Raton: CRC Press) Ch.5

[94] H. S. Bosch and G. M. Hale 1992 *Nucl. Fusion* **32** 611

[95] A. M. Frolov 1994 *Can. J. Phys.* **72** 33

[96] A. M. Frolov, V. M. Smith Jr. and G. T. Smith 2002 *Can. J. Phys.* **80** 43

[97] Mathematica, Wolfram Research Inc., Version 7.0, Champaign, IL; 2008

[98] D. Sarkar and A. Haji-Sheikh 2012 *Int. Commun. Heat. Mass* **39** 1009

[99] Y. Sun and Y. S. Wichman 2004 *Int. J. Heat Mass Transfer* **47** 1555

[100] R. A. Axford 2000 *Laser and Particle Beams* **18** 93

[101] E. Larsen 1988 *J.Comput.Phys.* **78** 459

[102] P. Barbucci and F. Di Pasquantonio 1977 *Nucl. Sci. Eng.* **63** 179

[103] J. C. Stewart 1965 *J. of Quantitative Spectroscopy and Radiative Transfer* **5** 637

[104] H. L. Wilson 1973 *A new numerical technique for solving the time dependent radiation transport equation, edited by C. A. Rouse,* Progress in High Temperature Physics and Chemistry 1973, Pergamon Press.

[105] M.D.Sekora and J.M.Stone 2010 *J. Comput Phys.* **229** 6819

[106] M. L. Wilkins 1999 *Computer Simulation of Dynamic Phenomena* (Springer-Verlag, Berlin, Heidelberg, New York) ISBN 3-540-63070-8

[107] R. L. Kauffman, *et al* 1994 *Phys. Rev. Lett.* **73** 2320

[108] M. Basko 1996 *Phys. Plasmas* **3** 4148

[109] G. L. Olson, L. H. Auer and M. L. Hall 2000 *J. of Quantitative Spectroscopy and Radiative Transfer* **64** 619

[110] W. H. Press *et al* 1992 *Numerical Recipes in Fortran* Cambridge University Press ISBN 81-85618-17-8

[111] W. Smith, T. R. Forester, I. T. Todorov and M. Lesley, DL_POLY 2 User manual, CCLRC, Daresbury Lab.

[112] A. Kokalj 2003 *Comp.Mater.Sci.* **28** 155. Code available from http://www.xcrysden.org

[113] H. J. C. Berendsen, J. P. M. Postma, W. F. van Gunsteren, A. DiNola and J. R. Haak 1984 *J.Chem.Phys.* **81** 3684

[114] L. Verlet 1967 *Phys. Rev.* **159** 98

[115] J. A. Moriarty 1986 *Shock Waves in Condensed Matter ed Y M Gupta* (New York: Plenum Press) p101

[116] S. Japel, B. Schwager, R. Boehler and M. Ross 2005 *Phys. Rev. Lett.* **95** 167801

[117] R. Boehler and M. Ross 1997 *Earth and Planetary Sci. Lett.* **153** 223

[118] J. Bouchat, F. Bottin, G. Jomard and G. Zerah 2009 *Phys. Rev.* B **80** 094102

[119] J. R. Chelikowski and K. E. Anderson 1987 *J.Phys.Chem.Solids* **48** 197

[120] W. A. Soffa and D. E. Laughin 2004 *Prog.Mater.Sci.* **49** 347

[121] N. Karlsson 1951 *J.Inst.Metals* **79** 391

[122] M. H. Mueller and H. W. Knott 1963 *Transactions of the Metallurgical Society of AIME* **227** 674

[123] A. Belsky, M. Hellenbrandt, V. L. Karen and P. Luksch 2002 *Acta Cryst.* B **58** 364

[124] R.T. Hong, M.J. Huang and J. Y. Yang 2005 *Mater. Sci. Semiconductor Processing* **8** 587

[125] A. R. Denton and N. W. Ashcroft 1991 *Phys.Rev.* A **43** 3161